THESIS FOR THE DEGREE OF DOCTOR OF PHILOSOPHY IN THERMO AND FLUID DYNAMICS

Spark Ignition Combustion of Direct Injected Alternative Fuels

Stratified Combustion and Application to Hybrid Powertrains

LARS CHRISTIAN RIIS JOHANSEN

Department of Applied Mechanics
Division of Combustion
CHALMERS UNIVERSITY OF TECHNOLOGY

Göteborg, Sweden 2016

Spark Ignition Combustion of Direct Injected Alternative Fuels
Stratified Combustion and Application to Hybrid Powertrains
LARS CHRISTIAN RIIS JOHANSEN
ISBN 978-91-7597-510-8

Doktorsavhandlingar vid Chalmers tekniska högskola
Ny serie nr. 4191
ISSN 0346-718X
Department of Applied Mechanics
Division of Combustion
Chalmers University of Technology
SE-412 96 Göteborg
Sweden
Telephone: +46 (0)31-772 1000

Cover:
Contours of OH* chemiluminescence from spark ignited, globally lean, stratified combustion of E85 in an optical engine with advancing time.

Chalmers Reproservice
Göteborg, Sweden 2016

Spark Ignition Combustion of Direct Injected Alternative Fuels
Stratified Combustion and Application to Hybrid Powertrains
Thesis for the degree of Doctor of Philosophy in Thermo and Fluid Dynamics
LARS CHRISTIAN RIIS JOHANSEN
Department of Applied Mechanics
Division of Combustion
Chalmers University of Technology

Abstract

Several technologies and modifications exist to increase the fuel efficiency of passenger vehicles in general and spark ignition engines in particular. Combining a spark ignition engine with an electric drive system in hybrid powertrain and thermodynamic cycle improvements are two such approaches with the potential to greatly reduce fuel consumption. Thermodynamic efficiency can be improved by lean engine operation. Extension of the lean limit leading to unthrottled operation is possible with lean stratified combustion. Stratified combustion leads to increased soot formation in addition to NOx with standard catalyst aftertreatment. Ethanol is an alternative fuel for spark ignition engines which is renewable and potentially leads to a reduction in soot formation in lean stratified combustion. In addition to liquid fuels, spark ignition engines are able to operate with gaseous fuels.

The potential for reduction of spark ignition engine emissions during engine load transients using assistance from the electric powertrain was investigated. NOx emissions during engine load transients were reduced with simulated electric powertrain assistance. CO, hydrocarbon and soot emissions occurred at the beginning and end of engine load transients due to transient fuel rich conditions in the engine as a result of incorrect fuel metering. Electric assistance did not reduce soot emissions as they were unconnected to the engine load value during the transient.

Combustion, sources of soot formation and soot oxidation in lean, spark ignited, stratified combustion of E10 (10 % vol. ethanol, 90 % vol. gasoline) and E85 were investigated in an engine with optical access using pressure analysis, high speed imaging, OH* chemiluminescence and soot incandescence. Diffusion combustion of liquid fuel films on the surface of the piston, referred to as a pool fire, was a major source of soot formation for both E10 and E85 with a single injection due to the fuel spray impingement on the piston. The effect was magnified when the engine load was increased. For E10 soot formation also occurred in the gas phase. Pool fires were the sole source of soot formation with E85 as the fuel. Splitting the single injection into multiple injections reduced the magnitude of soot formation from pool fires for both E10 and E85. Soot formation in the gas phase with E10, appeared to increase slightly with multiple injection for both engine loads. Multiple injections led to an increase in the rate and stability of combustion in all cases.

Gaseous fuels such as hydrogen and methane amongst others are another class of alternative fuels for spark ignited engines. The self similarity and the Turner model for the structure of transient jets during injection with a range of injection and ambient pressures was investigated with high speed schlieren imaging of helium jets. The Turner model was found to be an accurate approximation for the structure of the jet in all cases. The ratio of the jet width to the length was found to vary with the injection pressure to ambient pressure ratio indicating that the jet width to length ratio varied with different pressure ratio.

Keywords: internal combustion engine, spark ignition, stratified combustion, optical dianostics

Preface

The work described in this thesis was conducted by the author during employment as a doctoral student between 2011-02-01 and 2016-07-15 at the Divsion of Combustion in the Department of Applied Mechanics at Chalmers University of Technology. The main supervisor and examiner was Head of the Division of Combustion, Professor Ingemar Denbratt. Associate Professor Petter Dahlander and Assistant Professor Stina Hemdal also provided supervision for the work described in this thesis. Funding for the work was provided by the Swedish Energy Agency and in-kind support was provided by Volvo Car Corporation.

NOMENCLATURE

Dimensions

Dimension symbol	Description	SI base unit	Symbol
M	Mass	kilogram	kg
T	Time	second	s
L	Length	metre	m
Θ	Temperature	kelvin	K
N	Amount of substance	mole	mol

Latin

Symbol	Dimensions	Description
A	L^2	Area
C_D		Drag coefficient
C_f	$\mathrm{M\,L\,T^{-2}}$	Constant road friction coefficient
C_v	$\mathrm{M\,T^{-1}}$	Road friction speed coefficient
C_{vn}	$\mathrm{M\,L^{1-n}\,T^{n-2}}$	Road friction speed power coefficient
D	L	Maximum jet width
H	$\mathrm{M\,L^2\,T^{-2}}$	Enthalpy
K		Soot absorption coefficient
L	L	Optical depth of soot
M	$\mathrm{M\,N^{-1}}$	Molar mass
Q	$\mathrm{M\,L^2\,T^{-2}}$	Heat transfer
Q_{ch}	$\mathrm{M\,L^2\,T^{-2}}$	Change in internal energy of formation (heat release from combustion)
R	$\mathrm{L^2\,T^{-2}\,\Theta^{-1}}$	$= R_{\mathrm{u}}\,/M$ Specific gas constant
R_{u}	$\mathrm{M\,L^2\,T^{-2}\,\Theta^{-1}\,N^{-1}}$	$=8.314\,459\,8(48)\,\mathrm{J\,K^{-1}\,mol^{-1}}$. Gas constant
$\mathcal{R}$		Image pixel set
T	Θ	Temperature
U	$\mathrm{M\,L^2\,T^{-2}}$	Internal energy
V	L^3	Volume
W	$\mathrm{M\,L^2\,T^{-2}}$	Work
c_p	$\mathrm{L^2\,T^{-2}\,\Theta^{-1}}$	Constant pressure specific heat capacity
c_V	$\mathrm{L^2\,T^{-2}\,\Theta^{-1}}$	Constant volume specific heat capacity
d	L	Diameter
f	$\mathrm{T^{-1}}$	Frequency
h	$\mathrm{L^2\,T^{-2}}$	Specific enthalpy
i		Intensity
k	$\mathrm{L^3\,M^{-1}}$	Gladstone-Dale coefficient
m	M	Mass
$\dot{m}$	$\mathrm{M\,T^{-1}}$	Mass flow rate
n	N	Amount of substance
n		Refractive index
$\dot{n}$	$\mathrm{N\,T^{-1}}$	Amount of substance flow rate
p	$\mathrm{M\,L^{-1}\,T^{-1}}$	Pressure
s		Spread
t	T	Time
u	$\mathrm{L^2\,T^{-2}}$	Specific internal energy
u		Horizontal image pixel index
v		Vertical image pixel index
v	$\mathrm{L\,T^{-1}}$	Velocity
z_t	L	Jet penetration length

Greek

Symbol	Dimensions	Description
Γ		Self-similarity variable dependent constant
η		Efficiency
κ		Polytropic coefficient
λ		Ratio of the air to fuel ratio relative to stoichiometric ratio
γ		Ratio of specific heat capacities
ν	$\mathrm{M\,L^{-1}\,T}$	Dynamic viscosity
ω	$\mathrm{T^{-1}}$	Engine crankshaft rotational frequency
ϕ		Ratio of the fuel to air ratio relative to stoichiometric ratio
ρ	$\mathrm{M\,L^{-3}}$	Density
σ	$\mathrm{M\,T^{-2}}$	Surface tension
θ		Crank angle

Subscripts

Symbol	Dimensions	Description
CO2,eq		CO_2 equivalent
V		Isochoric (constant volume)
a		Air
ad		Adiabatic
amb		Ambient
c		Critical
d		Displacement
exh		Exhaust
f		Fuel
i		Index
inj		Injection
int		Intake
l		Liquid
lv		Vapourization
m		Molar quantity
noz		Nozzle
p		Isobaric (constant pressure)
p		Particulate
r		Road
s		Stoichiometric
sat		Liquid-vapour saturation
amb		Ambient
t		Triple point
v		Vapour
vh		Vehicle
vol		Volumetric

Abbreviations

Symbol	Dimensions	Description
AR5		IPCC fifth assessment report [Int14a; Int14b]
BIW		Body in white. Car body without movable parts such as door and before painting
CA50		50 % fuel mass burned crank angle degree
CAD		Crank angle degree
CI		Compression ignition
CoV		Coefficient of variation
E10		10 % vol. ethanol, 90 % vol. gasoline
E85		85 % vol. ethanol, 15 % vol. gasoline
EM		Electric motor
EVC		Exhaust valve close
EVO		Exhaust valve open
GHG		Greenhouse gas
ICE		Internal combustion engine
IEA		International Energy Agency
IMEP	$\mathrm{M\,L^{-1}\,T^{-2}}$	Indicated mean effective pressure
IPCC		Intergovernmental Panel on Climate Change
IVC		Intake valve close
IVO		Intake valve open
LHV	$\mathrm{L^{2}\,T^{-2}}$	Lower heating value
MON		Motor octane number
Mtoe	$\mathrm{M\,L^{2}\,T^{-2}}$	= 41.868 PJ, million tonne of oil equivalent [Intb]
NMHC		Non-methane hydrocarbon
OECD		Organisation for Economic Co-operation and Development
PAH		Poly aromatic hydrocarbon
PM	M	Particulate mass
PN		Particulate number
PRF		Primary reference fuel
RON		Research octane number
RPM		Revolutions per minute
SCR		Selective catalytic reduction
SI		Spark ignition
SOI		Start of injection
SOS		Start of spark
THC		Total hydrocarbon
TWC		Three way catalyst
exh		Exhaust
int		Intake
toe	$\mathrm{M\,L^{2}\,T^{-2}}$	= 41.868 GJ, tonne of oil equivalent [Intb]

THESIS

This thesis consists of an extended summary and the following appended papers:

Paper A	L. C. R. Johansen and S. Hemdal. In cylinder visualization of stratified combustion of E85 and main sources of soot formation. *Fuel* **159** (2015), 392–411. DOI: `10.1016/j.fuel.2015.07.013`
Paper B	L. C. R. Johansen, S. Hemdal, and I. Denbratt. Comparison of E10 and E85 Spark Ignited Stratified Combustion and Soot Formation. *Submitted to Fuel* (2016)
Paper C	L. C. Johansen, I. Denbratt, and S. Hemdal. Drive Cycle Particulate and Gaseous Emissions from a Parallel Hybrid Combustion Engine and Electric Powertrain. *SAE Technical Paper 2015-24-2538* (2015). DOI: `10.4271/2015-24-2538`
Paper D	L. C. Johansen, E. de Benito Sienes, and P. Dahlander. Analysis of Transient Compressible Gas Jets Using High Speed Schlieren Imaging. *SAE Technical Paper 2013-01-0871* (2013). DOI: `10.4271/2013-01-0871`

Contents

Extended Summary

Chapter 1

Motivation

Greenhouse gas emissions levels will come to determine future global mean surface temperatures. Greenhouse gas emissions will need to be reduced 41 % to 72 % by 2050 if the temperature rise is remain less than 2 °C by 2100 [Int14a, Table 6.3]. Road transport is responsible for a significant fraction of global greenhouse gas emissions due to the overwhelming use of oil and derived products within the sector [Int14a, Figure 1.3a] [Inta]. Emissions from road transport can amongst other ways be reduced by increasing fuel efficiency of vehicles and switching from non-renewable fuels with a large carbon content per unit of energy to renewable fuels with smaller carbon content [Int14a, Ch. 8]. Light duty vehicles, comprised of passenger vehicles and light commercial vehicles, in particular are responsible for 47 % of energy use in the road transport sector and are a prime candidate for efforts to increase fuel efficiency and reduce GHG emissions [Int12, Figure 7].

Light duty vehicles predominantly use either compression ignition or spark ignition engines. Compression ignition engines in general achieve a larger thermodynamic efficiency due to the larger compression ratio compared to spark ignition engines and less throttling but cannot operate on the same fuels as spark ignition engines [Hey89, Ch. 3,Ch. 10]. Spark ignition engines can provide a larger power output for a given engine displacement and lower emissions in comparison to compression ignition engines in part due to exhaust gas aftertreatment systems [Hey89, Ch. 11].

The EU has adopted legislation limiting CO_2 average new car emissions which is to be fully enforced in 2016 [The09] with further reductions by 2020 [The14]. Additionally, emissions of NOx, CO, hydrocarbons and particulate matter from passenger cars are regulated [The12] with limits which have similarly reduced over the course of several iterations of emissions standards.

Several technologies and modifications exist to increase the fuel efficiency of passenger vehicles in general and spark ignition engines in particular. Combining a spark ignition engine with an electric drive system in hybrid powertrain and thermodynamic cycle improvements are two such approaches with the potential to greatly reduce fuel consumption [Int12]. Hybrid powertrains offer the possibility for a reduction in fossil fuel use by using electric potential energy sourced from renewable sources in the electric drive system of the hybrid powertrain. Several approaches to thermodynamic cycle improvement exist. Lean homogeneous combustion operation reduces pumping work due to a reduction in throttling and the excess air leads to an increase in expansion work [Hey89, Ch. 5]. Due to excess oxygen in the exhaust, NOx in the exhaust gas cannot be converted using traditional three way catalysts. Extension of the lean limit leading to unthrottled operation is possible with lean stratified combustion. Stratified combustion leads to increased soot formation in addition to the issue of NOx aftertreatment. Ethanol is an alternative fuel for spark ignition engines which is renewable and potentially leads to a reduction in soot formation in lean stratified combustion. In addition to liquid fuels, spark ignition engines are able to operate with gaseous fuels.

1.1 Scope

The electric drive in a hybrid powertrain provides the means to assist and reduce the load on the internal combustion engine in the powertrain during load transients by providing part of the required torque. This was hypothesized to reduce emissions of NOx, CO, hydrocarbons and soot and was investigated using a three cylinder, spark ignited, direct injected, turbocharged engine and simulated electric motor assistance during load transients in a modified new European driving cycle on a dynamometer stand. This study is described in Paper C.

Lean, spark ignited, spray guided, stratified combustion increases the cycle thermal thermodynamic efficiency of spark ignited engines by reducing throttling leading to a reduction in pumping work and an increase in expansion work due to the excess air and increase in specific heat ratio [Hey89; ZLH99; Alk07]. In order to provide an ignitable fuel and air mixture capable of sustaining a flame, fuel is injected late in the compression stroke. This produces an inhomogeneous and stratified mixture ranging from fuel lean to fuel rich [PRS14]. The latter provides conditions suitable for soot formation. Spray impingement on the piston due to the proximity of the piston resulting in pool fires has been observed in wall guided engines and may be an issue in spray guided stratified combustion. Ethanol is a renewable fuel which has been shown in laboratory flames [Mar12] and in stratified combustion [Fra11] to lead to a reduction in soot. The sources of soot formation and soot oxidation in lean, spark ignited, spray guided, stratified combustion was studied and compared for E10 (10 % vol. ethanol, 90 % vol. gasoline) and E85 in an optical engine using an piezo actuated, outward opening pintle injector. Two engine loads were studied. The effect of injection strategy on combustion, soot formation and soot oxidation was investigated given previous indications that split injections improve combustion stability and work output [Oh+11]. This study is described in Paper A and Paper B.

Lean stratified combustion with gaseous fuels is likely to require the ignition of the fuel during injection requiring an understanding of the structure of the gas jet [Moh+08]. Transient gas jets reach self similarity after a short transition immediately after the start of the jet and a model for the gas jet structure has been proposed previously [HO99]. The structure of helium gas jets and the self similarity variable for a range of injection and ambient pressures was studied using schlieren imaging. This study is described in

Paper D.

Chapter 2

Background

The Fifth Assessment Report (AR5) of the Intergovernmental Panel on Climate Change (IPCC) [Int14b] concluded that anthropogenic greenhouse gas emissions are extremely likely to be the dominant cause [Int14b, SPM 1.2] of warming of the global climate system, at levels unprecedented over decades to millennia [Int14b, SPM 1.1]. Global annual anthropogenic greenhouse gas emissions between 1970 and 2010 are shown in Figure 2.1. Global greenhouse gas emissions increased 81 % in that time period. CO_2 originating from fossil fuels usage and industrial processes was the largest constituent of total greenhouse gas emissions annually, similarly increasing from 15 $\mathrm{Gt}_{\mathrm{CO2,eq}}$ and 55 % of global anthropogenic greenhouse gas emissions in 1970 to 32 $\mathrm{Gt}_{\mathrm{CO2,eq}}$ and 65 % in 2010. The IPCC concluded that the consequences of additional greenhouse gas emissions are a further increase global warming and persistent changes in the climate system which in turn will lead to a greater chance of severe consequences for both ecosystems and people [Int14b, SPM 2]. Given the predominance of CO_2 in global greenhouse gas emissions and the previous findings, it is not surprising that the cumulative emissions of CO_2 will come to determine global warming by the end of the 21st century [Int14b, SPM 2.1] and are directly linked to the future risk levels of climate change. "Risks from climate change depend on cumulative CO_2 emissions which in turn depend on annual GHG emissions over the next decades." ([Int14b, Figure 3.1]).

> Without additional efforts to reduce GHG emissions beyond those in place today, emissions growth is expected to persist, driven by growth in global population and economic activities despite improvements in energy supply and end-use technologies (high confidence). ([Int14a, TS.2.2])

This highlights the need for mitigation of GHG emissions along with adaptation as outlined by the IPCC to avoid the projected increase of global mean surface temperatures of 3.7 °C to 4.8 °C in 2100 in the above above stated scenario [Int14a]. If it is to remain likely that the global mean surface temperature increase will be below 2 °C[1], CO_2 emissions must be reduced by 41 % to 72 % by 2050 [Int14a, Table 6.3].

---

[1] Relative to 1850-1900

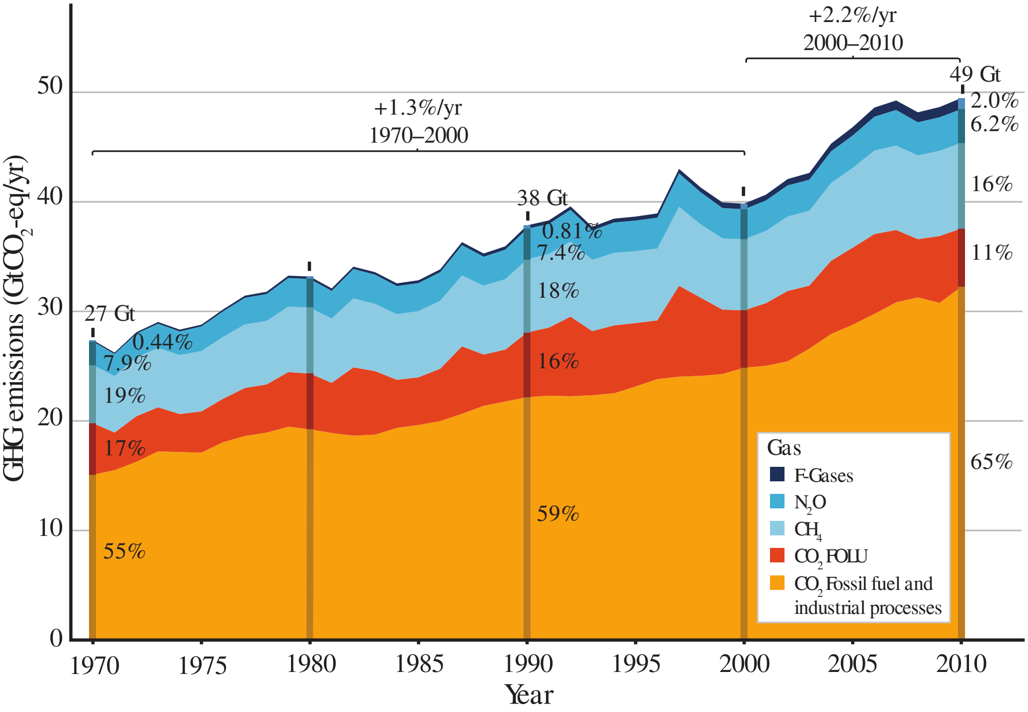

Figure 2.1: *Global greenhouse gas emissions 1970-2010. Forest or land use (FOLU). From [Int14a, Figure 1.3c]*

Transport was responsible for 14.1 % of global greenhouse gas emissions in 2010 as shown in Figure 2.2. Road transport in particular was responsible for 10.2 % of global GHG emissions and the greater part of total transport emissions with 72 %. A reduction of road transport emissions would contribute significantly to reducing global total GHG emissions by virtue of the share of emissions originating from the sector.

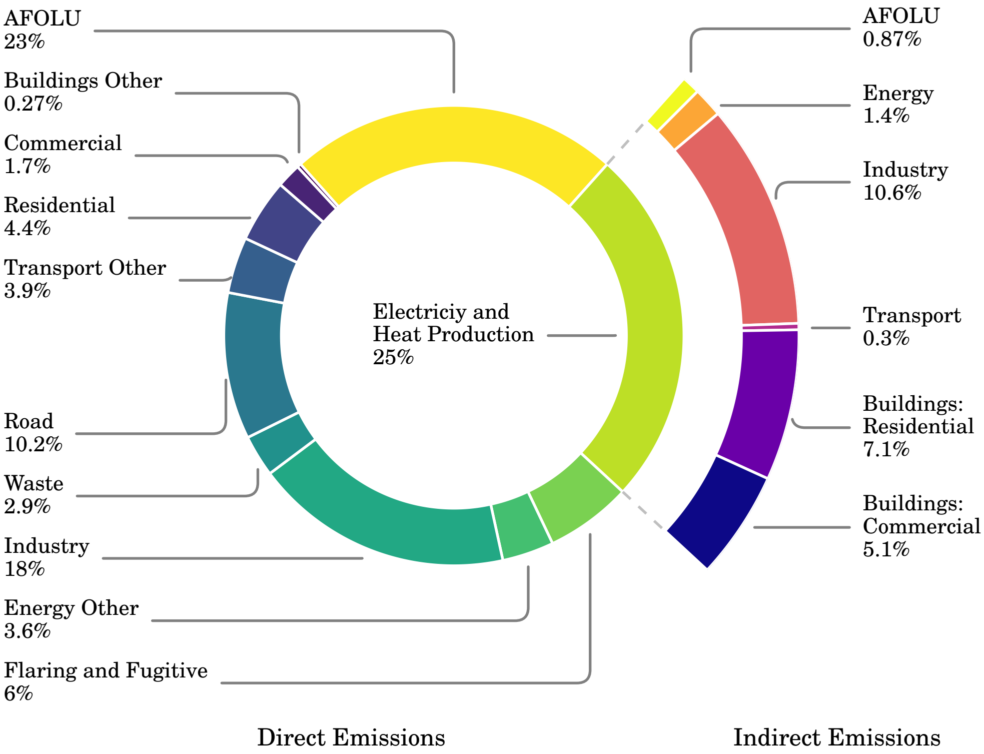

Figure 2.2: *Global greenhouse gas emissions by sector in 2010. Agriculture, forest or land use (AFOLU) [Int14a]. Adapted from [Int14a, Figure 1.3a]*

Global road transport energy is sourced almost exclusively from oil products and accounts for a large fraction of total global oil consumption through oil products. In 2013 oil products provided 94.9 % of road transport energy as shown in Figure 2.3 and road transport accounted for 49.5 % oil products used [Inta].

Oil is a non-renewable fuel source and a net contributor of CO_2 to the atmosphere when used as a fuel in combustion. In addition to the dominance of oil as an energy source in road transport, aviation and maritime fuels are sourced exclusively from oil [Inta]. Oil is one of the primary sources of global CO_2 emissions with 33 % of emissions in 2013 created from the combustion of oil and products derived from oil [Int15].

Light duty vehicles, comprised of passenger vehicles and light commercial vehicles, are responsible for the largest use of energy within the road transport sector with 47 %

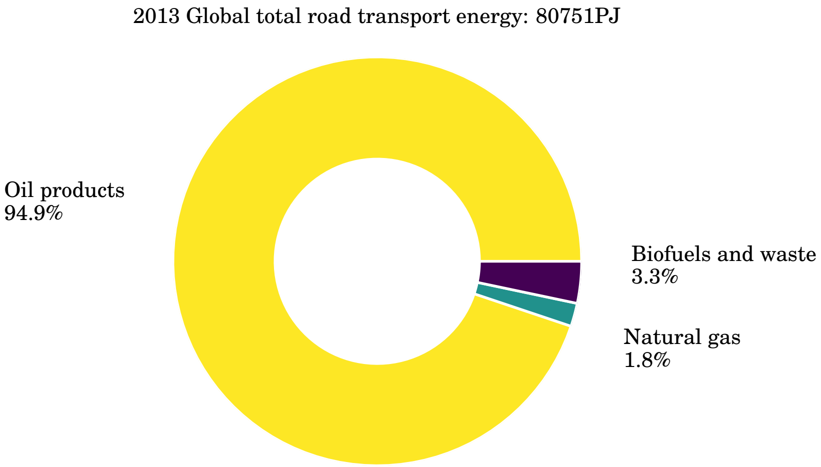

Figure 2.3: *Global road transport energy use and sources in 2013. Source [Inta]*

of energy as shown in Figure 2.4. Since oil is the almost exclusive source of energy for road vehicles, this illustrates the importance of light duty vehicles and passenger cars with respect to reducing CO_2 emissions.

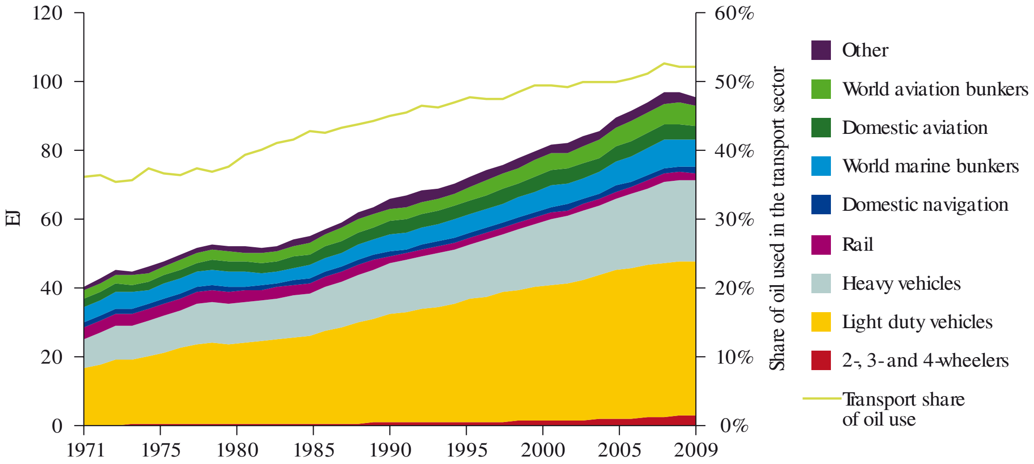

Figure 2.4: *Global transport energy use by mode 1971-2009. From [Int12, Figure 7]*

2.1 Reducing Vehicle Emissions

"Direct regulatory approaches and information measures are widely used, and are often environmentally effective... (medium confidence)." ([Int14a, TS.4.2]).

> Policies that promote fuel economy technologies and improve tested and in-use fuel economy, including fuel economy standards, fiscal measures and information/ education programmes, will play a critical role in maximizing fuel economy improvements in all countries over the coming decades.. ([Int12]).

Legislation limiting CO_2 emissions from the transport sector has been introduced in several countries for various transport sectors. Most countries in the OECD and China have introduced fuel economy standards [Int12]. The EU introduced legislation in 2009 limiting CO_2 emissions from new passenger cars to $130\,\mathrm{g\,km^{-1}}$[The09] by 2015 with the limit lowered further in 2014 to $95\,\mathrm{g\,km^{-1}}$ for new passenger cars by 2021 [The14].

The IPCC Working Group III [Int14a, Ch. 8] outlined four GHG emission mitigation pathways for transport:

- Avoiding journeys where possible
- Modal shift to lower-carbon transport systems
- Lowering energy intensity (MJ/(passenger km) or MJ/(t km))
- Reducing carbon intensity of fuels ($CO_{2,\mathrm{eq}}$/MJ)

Of the four, the last two involve modifications to vehicles. Lowering energy intensity is equivalent to lowering vehicle fuel consumption by adoption of new technologies and modifications. Reducing carbon intensity of fuels can be achieved by replacing oil derived fuels with fuels produced from renewable sources. National goals toward the replacement of fossil fuels in transport have been adopted in Sweden [Gov16].

Light duty vehicles with internal combustion engines use either spark ignition (SI) or compression ignition (CI). While alternative fuels for exist for both engine types and are increasingly used, the predominant fuel for each remains respectively gasoline and diesel. As a result, the engine types are often referred to as gasoline engines and diesel engines respectively. Both gasoline and diesel are produced by fractional distillation of oil. The thermal efficiency of internal combustion engines is amongst other factors determined by and proportional to the compression ratio and the excess air [Hey89, Ch. 3]. Spark ignition engines in general use a smaller compression ratio than typically used by compression ignition engines due to the onset of knock, which can damage the engine, as the compression ratio increases in spark ignition engines. Spark ignition engines are not able to operate with same amount of excess air as diesel engines further limiting thermal efficiency. Spark ignition engines are nevertheless still used in part because they can use fuels which cannot be used in compression ignition engines in addition to larger power output at a fixed engine cylinder volume.

Numerous possibilities exist for reducing the fuel consumption of light duty vehicles. Approaches to reduce fuel consumption and estimates of the reduction for vehicles with spark ignition engines are given in Table 2.1. While four stroke, spark ignition engines first appeared in 1876 with the first prototype created by Nicolaus A. Otto [Hey89, Ch. 1] and have been developed and improved upon since, many possibilities for improving the thermal efficiency of spark ignition engines still remain. Direct injection Thermodynamic cycle improvements include such technologies as lean homogeneous combustion, lean stratified combustion, Miller cycle and homogeneous charge compression ignition (HCCI) to name but a few. Strong downsizing involves reducing the engine displacement volume so that the engine on average operates at a larger engine load where spark ignition engines typically operate more efficiently due in part to less throttling and a reduction in the associated losses [Hey89, Ch. 15][MST12, Ch. 2]. From the fuel reduction estimates in Table 2.1 it is apparent that thermodynamic cycle improvements and downsizing are promising approaches to improving engine efficiency.

	Technology	Reduction in fuel use/%
Spark Ignition	Low friction design and materials	2
	Tyres: low rolling resistance	3
	Aerodynamics improvement	2
	Reduced driveline friction	1
	Lightweight components other than BIW	2
	Thermal management	3
	Variable valve actuation and lift	2
	Auxiliary systems improvement	5
	Thermodynamic cycle improvements	14
	Strong downsizing	17
	Dual clutch transmission	6
	Strong weight reduction	12
	Cumulative before full hybridisation	51
	Full hybrid: electric drive	25
	Cumulative after full hybridisation	63

Table 2.1: Modifications and technology with the potential to reduce fuel consumption for light duty vehicles with spark ignition engines. From [Int12, Table 4]. Estimates of the reduction are relative to a 2005 vehicle. BIW: Body in white. Car body without movable parts such as door and before painting

Combustion of oil and oil derived fuels also results to a lesser degree in the emission of CO, NO, the greenhouse gases NO_2 and hydrocarbons and carbon particulate matter also referred to as soot. Soot and NO_2 are environmental pollutants and health hazards as well as greenhouse gases. CO is toxic and NO participates in ozone depletion.

Various emissions from road transport have been subject to legislative limits before CO_2 due to the hazards they pose. While CO_2 emission limits in the EU first entered into force in 2012 [The09, Article 4], limits on the emissions of CO and hydrocarbons began in 1970 [The70]. The EU has introduced increasingly stringent pollutant emission legislation since the first emission standard with limits lowered and additional types of emissions added. Euro 1 and subsequent emission standards provide emission limits based on the vehicle and engine type, with different limits for spark ignition and compression ignition engines amongst other criteria. The limits specified by the EU emission standards for passenger cars[2] with spark ignition engines[3] since the Euro 1 standard are provided in Table 2.2.

Having begun with CO and hydrocarbon limits, Euro 1 and subsequent emissions standards either added emission types or split combined emissions into separate limits for each type in addition to any overall reduction:

- Euro 1: NOx added with a limit on the combined hydrocarbon and NOx emissions
- Euro 3: Separate limits for hydrocarbons and NOx
- Euro 5: Non-methane hydrocarbons added and particulate mass for direct injection engines added
- Euro 6: Particulate number for direct injection engines added

While improving spark ignition engine fuel efficiency can lead to a reduction in CO and THC, it can lead to an increase in NOx and soot emissions depending on the method used to improve thermal efficiency. Lean homogeneous combustion leads to an excess of air and thus an increase in thermal efficiency but the NOx conversion efficiency of three-way catalysts decreases significantly with increasing excess oxygen leading to an increase in NOx emissions. Stratified lean combustion adds to this issue with an increase in soot formation and emissions due to locally fuel rich conditions and combustion in the cylinder. These examples illustrate the complexity of reducing CO_2 emissions through increased thermal efficiency and all other emissions from a spark ignition engines simultaneously.

---

[2] Category M: Motor vehicles with at least four wheels designed and constructed for the carriage of passengers [The01, Annex II].

[3] Spark ignition engines are classed as positive ignition in EU emissions standards.

	Source	Date of effect	CO $/\mathrm{g\,km^{-1}}$	THC $/\mathrm{g\,km^{-1}}$	NMHC $/\mathrm{g\,km^{-1}}$	NOx $/\mathrm{g\,km^{-1}}$	THC + NOx $/\mathrm{g\,km^{-1}}$	PM $/\mathrm{mg\,km^{-1}}$	PN $/\mathrm{km^{-1}}$
Euro 1	[The91]	1992-07	2.72				0.97		
Euro 2	[Eur96]	1996-01	2.2				0.5		
Euro 3	[The98]	2000-01	2.3	0.2		0.15			
Euro 4	[The98]	2005-01	1.0	0.1		0.08			
Euro 5	[The07]	2009-09	1.0	0.1	0.068	0.06		5.0	
Euro 6	[The09; The12]	2014-09	1.0	0.1	0.068	0.06		4.5	$6{\times}10^{11}$

Table 2.2: European emission limits for passenger vehicles (Category M) with spark ignition engines (positive ignition) since 1991. THC: total hydrocarbons, NMHC: non-methane hydrocarbons, PM: particulate mass, PN: particulate number. The particulate mass and number limits only apply to vehicles with direct injection engines [The12].

Chapter 3

Spark Ignition Engines

The vast majority of contemporary, four stroke, spark ignition engines employ one of two systems to introduce fuel into the engine cylinder; port fuel injection (PFI) or direct injection (DI). The difference between the two systems is illustrated in Figure 3.1. In port injected engines, fuel is injected immediately upstream of the intake valves while for direct injected engines the fuel is injected directly into the cylinder.

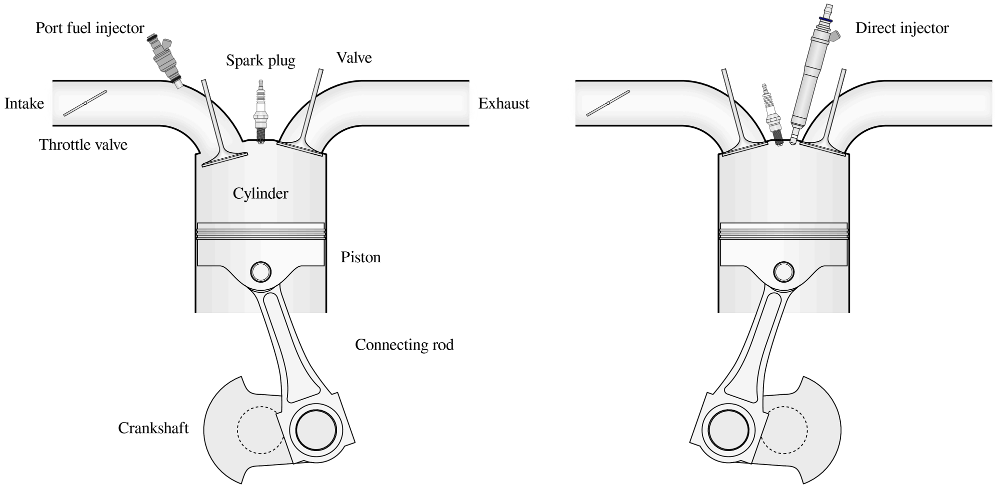

Figure 3.1: *Diagram of port injected and direct injected spark ignition engine cylinders*

The engine cycle for a four stroke, port injected engine is illustrated in Figure 3.2. Fuel vapour and air upstream of the intake valve are inducted into the cylinder during the intake stroke. This leads, ideally and in practice, to a homogeneous mixture of fuel and air. The amount of fuel is determined by the required engine power output. In order for a flame to propagate through the homogeneous fuel and air mixture and for the complete combustion of the fuel, the air mass should ideally be the exact amount required for the given fuel mass. The ratio of the fuel mass to the air mass for this condition is defined as the stoichiometric ratio and is dependent on the fuel composition as outlined in section 3.3. The ratio of the fuel-air ratio to the stoichiometric ratio is defined as the equivalence ratio, ϕ, as stated in Eq. 3.1a. The inverse of ϕ is denoted by λ as defined in Eq. 3.1b.

$$\phi = \frac{1}{\lambda} = \frac{\left(\dfrac{m_{\text{fuel}}}{m_{\text{air}}}\right)}{\left(\dfrac{m_{\text{fuel}}}{m_{\text{air}}}\right)_{\text{s}}} = \frac{\left(\dfrac{n_{\text{fuel}}}{n_{\text{air}}}\right)}{\left(\dfrac{n_{\text{fuel}}}{n_{\text{air}}}\right)_{\text{s}}} \tag{3.1a}$$

$$\lambda = \frac{1}{\phi} = \frac{\left(\dfrac{m_{\text{air}}}{m_{\text{fuel}}}\right)}{\left(\dfrac{m_{\text{air}}}{m_{\text{fuel}}}\right)_{\text{s}}} = \frac{\left(\dfrac{n_{\text{air}}}{n_{\text{fuel}}}\right)}{\left(\dfrac{n_{\text{air}}}{n_{\text{fuel}}}\right)_{\text{s}}} \tag{3.1b}$$

where m is mass and n is the amount of substance. The masses and amounts in Eq. 3.1a and Eq. 3.1b can be substituted by mass flow rates, $\dot{m}$, and amount flow rates, $\dot{n}$.

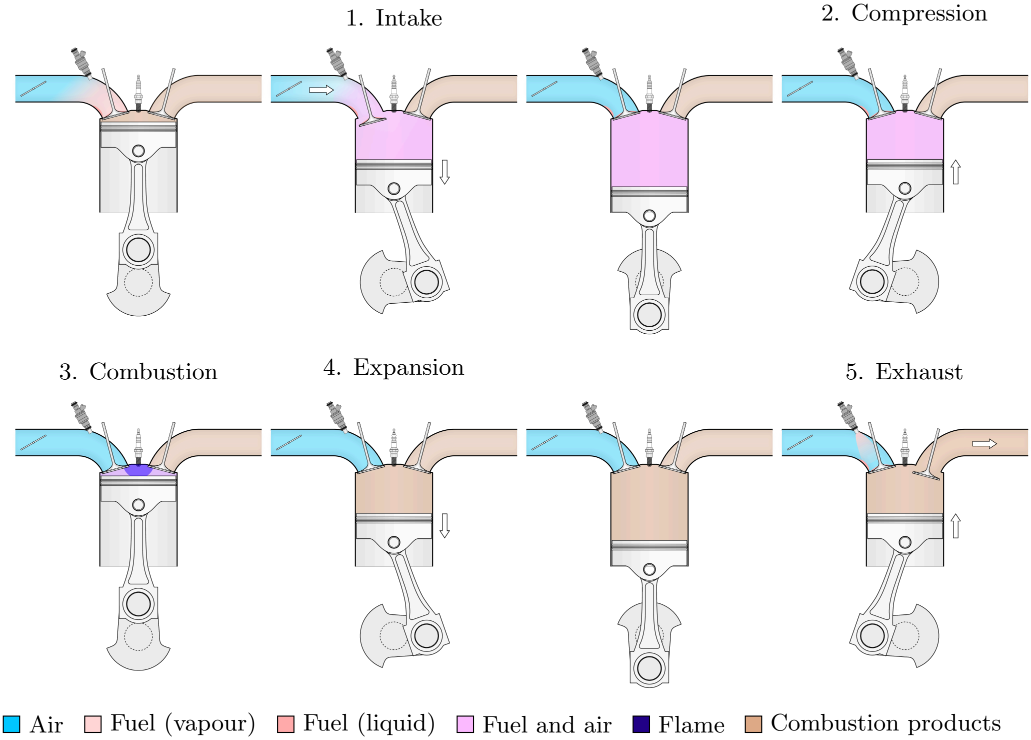

Figure 3.2: *Cycle for a port fuel injection, four stroke, internal combustion engine*

A certain fuel mass fraction in an air and fuel vapour mixture is required for ignition and a self sustaining flame [Kuo05]. Increasing the air mass fraction in a homogeneous cylinder mixture beyond the stoichiometric value or conversely decreasing the fuel mass fraction leads to slower flame propagation and eventually to incomplete combustion and ignition failure beyond a certain critical equivalence ratio [Hey89]. The latter phenomena is referred to as misfire. The throttle valve limits the mass of air which is inducted in order to provide a stoichiometric mixture in the cylinder for a given fuel quantity in both port injected and direct injected engines operating homogeneously.

In a port fuel injected engine the injection of fuel for a given engine cycle can in principle take place at any point after the intake valves close in the previous cycle and before the intake valve close (IVC) in the current engine cycle. In practice, in order to improve fuel vapourization, engine occurs during prior to the intake valves opening (IVO) in order to provide additional time for vapourization and in order to use the hot valve surface to provide additional energy for vapourization [Hey89, Ch. 7], [Rei15, p. 96]. This is illustrated in Figure 3.2 where injection occurs during the exhaust stroke and thus while the intake valve is closed and immediately prior to the intake valve opening prior at the start of the intake stroke. Fuel vapour and air is then inducted as illustrated at 1. in Figure 3.2. The large velocities in the vicinity of the intake valve during the intake stroke and the resulting bulk fluid motion in the cylinder help to create a homogeneous mixture of fuel vapour, air and residual combustion product gases [Hey89, Ch. 8].

Fuel injected in the intake port displaces air as it vapourizes as illustrated in Figure 3.3. This effect reduces the mass of air that could otherwise be inducted had fuel not been present in the intake. This is not an issue since while the engine operates at a fraction of the maximum work output and restriction of the inducted mass of air is necessary for a stoichiometric ratio of fuel and air. Indeed, the displacement of air by fuel vapour functions as different form of intake restriction analogous to the throttle valve. This effect does become an issue when the maximum work output of the engine is sought which in turn requires that the largest possible mass of air[1] is inducted into the cylinder allowing the largest mass of fuel to combust stoichiometrically. Fuel vapour in the intake port thus reduces the maximum engine work output by reducing the maximum air mass that can be inducted.

Injection of fuel in the intake port creates liquid fuel films on the intake port surfaces and on the intake valve on the port facing side. This is illustrated in Figure 3.3. The fuel films provide a source of fuel vapour. For a steady state engine load the fuel film

---

[1] Volumetric efficiency, η_{vol}, is a measure of the mass of air inducted into the cylinder relative to the mass of air with a volume equal to the cylinder at bottom dead center (BDC) at a standard temperature and pressure, typically 298.15 K and 0.1 MPa or at the conditions present at a location in the intake. It is in effect the air mass that could occupy the cylinder if the piston remained at bottom dead center and the intake valve remained open indefinitely.

$$\eta_{\text{vol}} = \frac{\dot{m}_{\text{air}}}{\rho_{\text{air,int}} V_d \dfrac{\omega}{2}} \tag{3.2}$$

where $\dot{m}_{\text{air}}$ is the engine or cylinder air mass flow rate, $\rho_{\text{air,int}}$ is the air density at a location in the intake, V_d is the engine or cylinder displacement volume, and ω is the engine crankshaft revolution frequency. The division of the engine revolution frequency by 2 accounts for the fact that a 4 stroke engine cycle inducts air every second revolution.

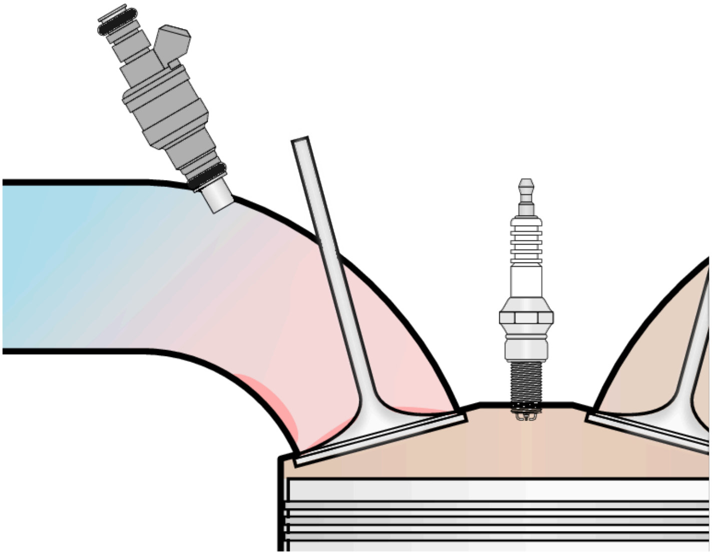

Figure 3.3: *Illustration of displacement of air by fuel vapour in the intake and liquid fuel films on the valve and intake surfaces as a result of port fuel injection*

mass similarly reaches a quasi-steady state. When the injected fuel desired change in engine work output, the fuel films and the fuel mass inducted enter a transient resulting in a transient equivalence ratio [Hey89, Ch. 7]. This is undesirable from the viewpoint of emissions as explained in section 3.4.

3.1 Direct Injection

The volumetric efficiency of a direct injected engine is increased relative to a port injected engine due to the lack of fuel vapour in the intake port due to the lack of fuel vapour in the intake port. Fuel injection for a direct injected engine operating with homogeneous combustion generally occur while the intake port is open and air is being inducted in order to take advantage of the large velocity and turbulent kinetic energy in the vicinity of the cylinder head which helps to mix the fuel and air to create a homogeneous mixture. The injection timing for a port injected and direct injected engine cylinder is compared in Figure 3.4. Volumetric efficiency can be increased further if fuel is injected after the intake valves have closed at the cost of reduced mixing both due to the reduction in mixing time prior to the spark and due to lower levels of turbulence after the induction of air has ceased.

The fuel mass quantity delivered to an engine cylinder can be controlled more accurately with direct injection of fuel into the cylinder in comparison to injection of fuel in the intake port prior to the opening of the intake valve where intake air dynamics and fuel film dynamics affect the fuel mass delivered to the cylinder. The lack of fuel film dynamics in direct injection also improves the transient load response of the engine [Hey89; ZLH99]. Vapourization of fuel in the cylinder lowers the cylinder gas temperature allowing the compression ratio to be increased [Bas09]. This increases the maximum indicated mean effective pressure and the increase in compression ratio increases thermal efficiency.

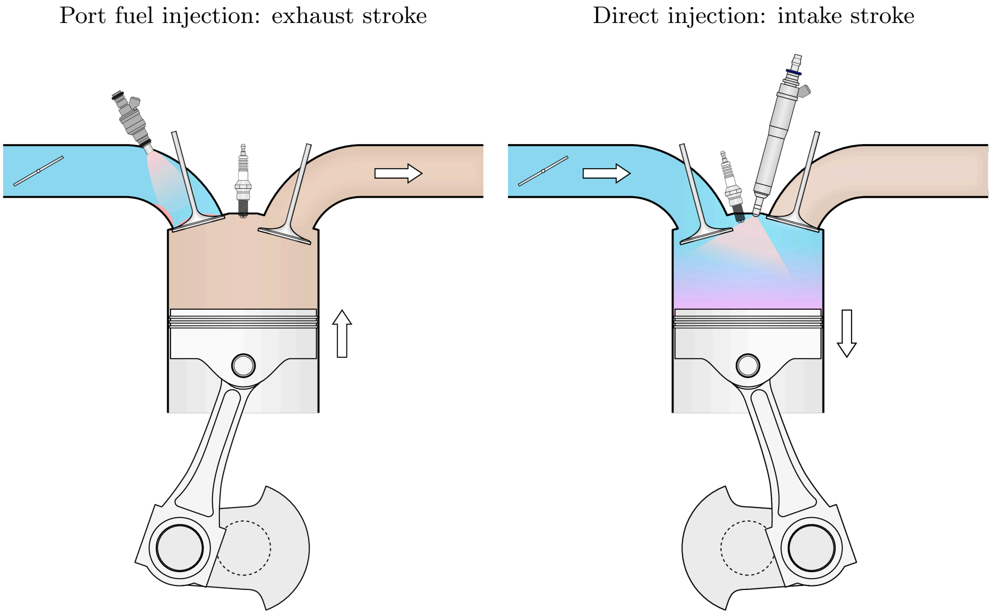
Port fuel injection: exhaust stroke

Direct injection: intake stroke

Figure 3.4: *Injection timing for port injected and direct injected engines operating with homogeneous combustion*

Figure 3.5 shows the pressure and volume relationship of a direct injected, single cylinder, optical engine. Apart from the injection timing, the cycle is the same as for the equivalent port injected configuration and the steps labeled in Figure 3.5 correspond to the steps in Figure 3.2.

3.1.1 Fuel Injectors

Two types of fuel injectors suitable for spart ignited direct injection engines are solenoid actuated injectors with multiple round nozzles (multi-hole injector) and piezo actuated injectors with an outward opening pintle opening (piezo injector) [ZLH99]. Spray penetration for a fixed fuel quantity is smaller for piezo injectors compared to multi-hole injectors [Mar+12].

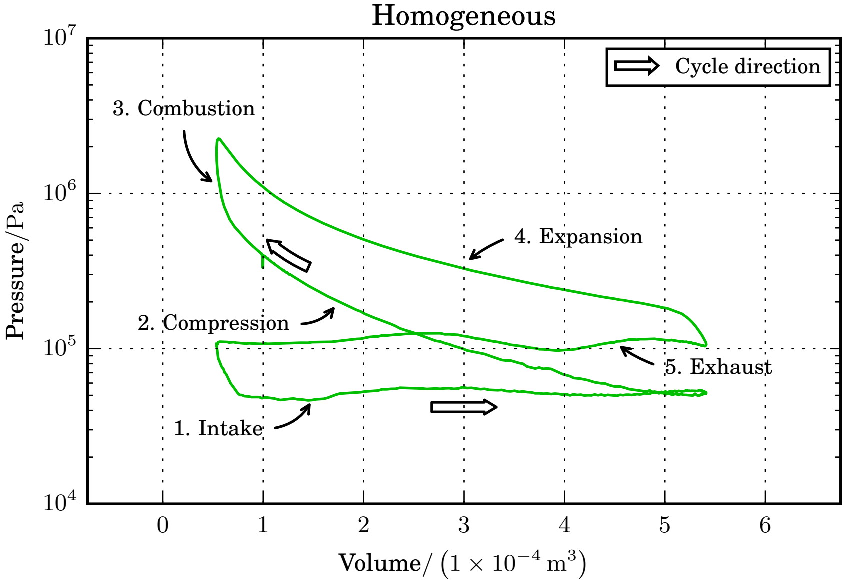

Figure 3.5: *Cylinder volume and pressure in a homogeneous combustion cycle. The pressure is the cycle ensemble average of 50 cycles. The engine is a direct injected, single cylinder, optical engine with a piezo actuated, outward opening pintle injector similar to the configuration shown in Figure 3.1.*

3.2 Stratified Combustion

In addition to the advantages of direct fuel injection in comparison to port fuel injection in stoichiometric homogeneous engine operation, direct injection also provides the means for stratified combustion which increases the maximum air to fuel ratio to the levels typical of unthrottled engine operation while maintaining stable and complete combustion. Unthrottled engine operation reduces the pumping losses in the cylinder gas exchange process as shown in Figure 3.7 and the peak temperature of the cylinder gas mixture, reducing heat losses [Alk07] and increasing expansion work [Hey89]. Globally lean stratified combustion in a spark ignition engine requires a localised fuel and air mixture with an air to fuel ratio which can sustain a flame front and which extends to the spark plug electrodes during the spark discharge. Several methods have been developed to achieve this [Bas09]. Most strategies rely on injecting fuel late in the compression stroke thereby limiting the extent of fuel and air mixing in order to prevent the local air to fuel equivalence ratio increasing beyond the limit required for stable and complete combustion. The wall guided concept involves injecting fuel towards a piston shaped so as to direct the fuel towards the spark plug. In the spray guided concept the injector and spark plug are located in close proximity so the fuel spray from the injector passes the spark plug gap directly after the injector. This is illustrated in Figure 3.6 where the approximate injection timing for homogeneous and stratified combustion operation in a direct injected engine is shown.

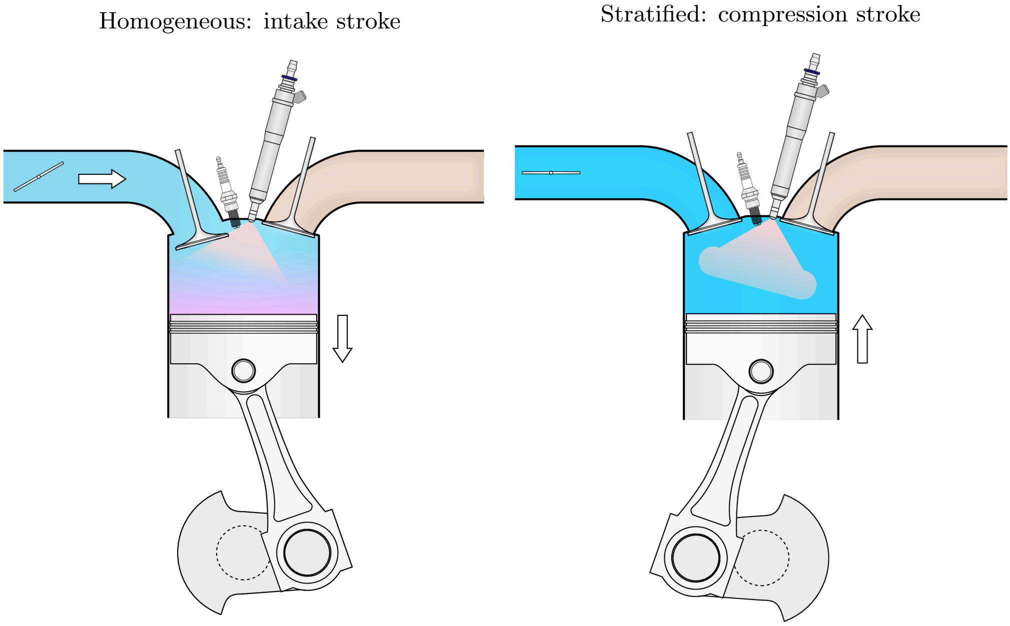
Homogeneous: intake stroke

Stratified: compression stroke

Figure 3.6: *Injection timing for homogeneous and stratified combustion in a direct injected engine*

Due to the limited mixing of fuel and air the local stoichiometry immediately prior to ignition varies spatially and temporally in the cylinder with the existence of regions devoid of fuel, fuel lean regions and regions rich in fuel relative to the stoichiometric fuel to air equivalence ratio. This is particularly true for spray guided concepts where fuel is confined to the center of the combustion chamber during fuel injection [Bas09]. Fuel rich conditions are known to be a prerequisite for the formation of soot in combustion [Sta01]. Inhomogeneously mixed fuel rich regions in diesel fuel sprays and diffusion combustion driven by injection of fuel into developed flames have been identified as a source of soot formation in diesel engines [Boc94, Ch. 24]. Spray guided stratified combustion consists of both local premixed combustion and local diffusion combustion due to the stratified fuel distribution. Premixed and diffusion combustion in fuel rich regions created by late injection during the compression stroke for spray guided stratified combustion have been observed for gasoline [Sto+05; OB13] and E85 [SR13] and both forms of combustion are expected to be a source of soot formation.

Liquid gasoline films on the surface of the piston created by the impingement of the fuel spray were observed in a wall guided engine with a multihole injector [Dra+03] and a spray guided engine with a swirl injector in near stoichiometric operation [SS01]. [SS01] observed an increased fuel film mass on the piston crown in an optical engine equipped with a centrally mounted swirl injector as the start of injection was delayed towards TDC. In this case, fuel films on the piston crown persisted for the duration of an engine cycle when fuel was injected in the second half of the compression stroke or in the first half of the intake stroke. In both studies combustion of the gasoline films on the piston crown resulted in diffusion flames referred to as pool fires.

Pool fires on the piston crown were confirmed as a source of soot formation in wall guided stratified combustion of gasoline using a multihole injector [Dra+03; Sto+05] and in spray guided stratified combustion both with globally near stoichiometric conditions using a swirl injector [SS01] and with globally lean conditions using a multihole injector [Vel+10]. In the latter study fuel impingement on the piston crown and the resulting fuel films and pool fires could not be eliminated by phasing the start of injection during the end of the compression stroke in lean spray guided stratified combustion using a multihole injector [Vel+10]. Phasing of the start of injection did not affect particulate emissions although the IMEP increased with an earlier phasing [Vel+10]. The measured particulate emissions for two injection phasings late in the compression stroke resulted in approximately equal particulate emissions and pool fires were concluded to be the main source of soot formation in the given study. In contrast, the soot incandescence and particulate emissions measured in an optical engine [Hem+11] and particulate emissions in a single cylinder metal engine [OB13] increased as the start of injection was delayed in spray guided stratified operation with outward opening piezo actuated injectors. NOx emissions decreased as the start of injection was delayed towards TDC [OB13]. Hollow cone fuel spray impingement on the spark plug electrodes has also been observed to cause pool fires late in the combustion process [Hem+11]. The spark plug was positioned in close proximity to the piezo injector in order to ignite the fuel spray directly. An increase in the piston crown fuel film mass and soot formation from the resulting pool fires is a possible explanation if the fuel film created by the spray from a outward opening piezo injector increases with delayed injection analogous to the observations for a swirl injector

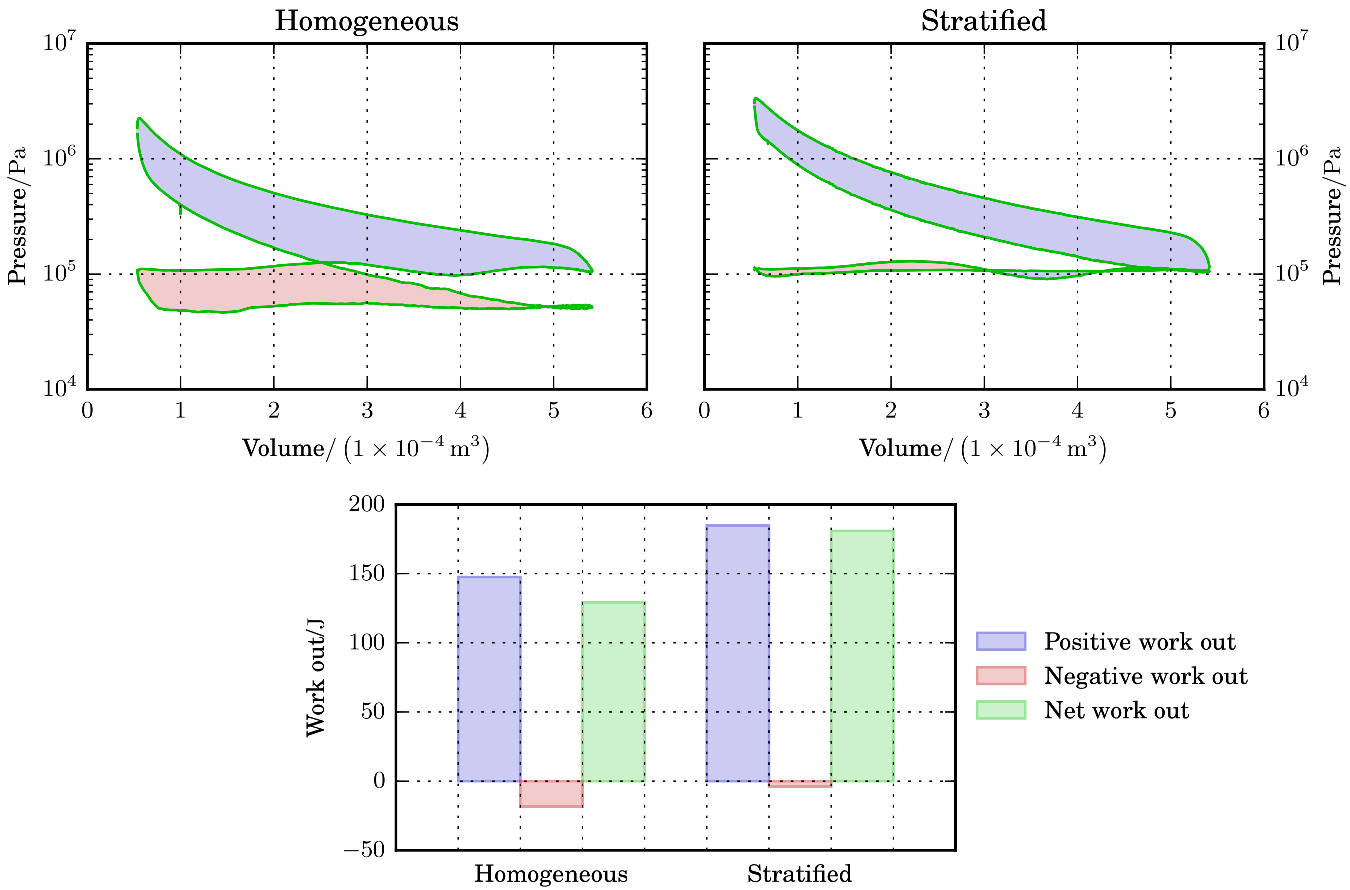

Figure 3.7: *Homogeneous and stratified cycle pressure and volume. The pressure is the cycle ensemble average of 50 cycles*

hollow cone spray [SS01].

3.3 Fuels

The stoichiometric ratio of the mass of air to the mass of fuel is dependent on the fuel composition. The most common fuels for reciprocating internal combustion engines consist of molecules composed of primarily or entirely of carbon, hydrogen and oxygen. For a molecule consisting of C, H and O, that is to say a fuel in the form of $\mathrm{C_aH_bO_c}$ where a, b, c are the number of the respective atoms in the molecule, the stoichiometric global chemical equation for the stoichiometric combustion of 1 mol of $\mathrm{C_aH_bO_c}$ is given in Eq. 3.3.[2]

$$\mathrm{C_aH_bO_c}+\left(\mathrm{a}+\frac{\mathrm{b}}{4}-\frac{\mathrm{c}}{2}\right)\left(\mathrm{O_2}+3.77\,\mathrm{N_{2,air}}\right)\longrightarrow \mathrm{aCO_2}+\frac{\mathrm{b}}{2}\mathrm{H_2O}+3.77\left(\mathrm{a}+\frac{\mathrm{b}}{4}-\frac{\mathrm{c}}{2}\right)\mathrm{N_{2,air}} \tag{3.3}$$

The stoichiometric ratio of the mass of air to the mass of fuel is derived from Eq. 3.3 and given in Eq. 3.4.

$$\frac{m_{\mathrm{air}}}{m_{\mathrm{fuel}}}=\frac{\left(\mathrm{a}+\frac{\mathrm{b}}{4}-\frac{\mathrm{c}}{2}\right)\left(1\,\mathrm{kmol}\cdot M_{\mathrm{O_2}}+3.77\,\mathrm{kmol}\cdot M_{\mathrm{N_{2,air}}}\right)}{1\,\mathrm{kmol}\cdot\left(\mathrm{a}\cdot M_{\mathrm{C}}+\mathrm{b}\cdot M_{\mathrm{H}}+\mathrm{c}\cdot M_{\mathrm{O}}\right)} \tag{3.4}$$

The stoichiometric air to fuel ratios of several hydrocarbons and alcohols are provided in Table 3.1

---

[2] In addition to $\mathrm{O_2}$ and $\mathrm{N_2}$, dry air consists of a number of other trace species with volume concentrations. less than $0.01\,\mathrm{m^3/m^3}$. The remaining moles of trace species in dry air are often incorporated into the number of $\mathrm{N_2}$ moles, and the molar mass is modified accordingly yielding a hypothetical 'air' $\mathrm{N_2}$, yielding 3.77 kmol of 'air' $\mathrm{N_2}$ per 1 kmol of $\mathrm{O_2}$, with a molar mass of $28.16\,\mathrm{kg\,kmol^{-1}}$. The molar mass of $\mathrm{N_2}$ is $28.01\,\mathrm{kg\,kmol^{-1}}$. The U.S. standard atmosphere (1976) sea-level composition is an idealized representation of the mean annual composition [Hay16]. The local concentration of $\mathrm{H_2O}$, $\mathrm{CO_2}$ and $\mathrm{H_2O}$ varies.

Species	Volume fraction/$\left(\mathrm{m^3\,m^{-3}}\right)$
$\mathrm{N_2}$	7.8084×10^{-1}
$\mathrm{O_2}$	$2.094\,76\times10^{-1}$
Ar	9.34×10^{-3}
$\mathrm{CO_2}$	3.14×10^{-4}
Ne	1.818×10^{-5}
He	5.24×10^{-6}
Kr	1.14×10^{-6}
Xe	8.7×10^{-8}
$\mathrm{CH_4}$	2×10^{-6}
$\mathrm{H_2}$	5×10^{-7}

3.3.1 Liquid Fuels

Gasoline

Gasoline as opposed to the potential fuel compounds in Table 3.1, is a mixture of alkanes[3], alkenes[4], alkynes and aromatics, with both normal and branched isomers of the above mentioned [Sch90]. One possible approach to provide a well defined fuel in studies involving gasoline is the use of a mixture of primary reference fuels (PRF) which match one or more properties of a commercial gasoline. Common primary reference fuels for internal combustion engines are n-hexane, n-heptane, isooctane and toluene [Zig+11] amongst many others [GHJ06]. A mixture of primary reference fuels as a substitute for another less well defined fuel mixtures is referred to as a surrogate fuel mixture. A common substitute for gasoline when only a single component is used is isooctane which is also used along with n-heptane to define the research octane number and motor octane number scales which quantify the knocking behaviour of fuels. A subset of engine relevant thermodynamic and transport properties of several primary reference fuels are provided in Table 3.1.

Ethanol

Ethanol is an alternative to gasoline in spark ignition engines with several advantages with respect to gasoline and gasoline surrogate fuel components. Ethanol can be produced from several renewable sources including waste products [NS11; Aga07]. Thermodynamic and combustion properties of ethanol and several surrogate gasoline fuel components used in fuel spray investigations [Zig+11; AR13] and laminar flame speed investigations [Dir+14] are given in Table 3.1. The lower enthalpy of combustion of ethanol is smaller in comparison with the alkanes listed in Table 3.1 and commercial gasoline. A greater mass of ethanol can combust with the same mass of air as a result of the lower stoichiometric air to fuel ratio of ethanol compared to normal alkanes due to the presence of a hydroxyl group. As a result, the lower enthalpy of combustion per unit mass of a stoichiometric fuel air mixture for ethanol is 1.5 % greater relative to isooctane. In addition, the cylinder gas temperature decrease due to vaporization of liquid fuel in the cylinder is greater for ethanol in comparison with the other fuels listed in Table 3.1 due to an enthalpy of vaporization more than twice as large which allows the compression ratio to be increased.

Ethanol has a greater research octane number and motor octane number than commercial gasoline blends. Blending of ethanol with primary reference fuels consisting of isooctane and n-heptane and commercial gasoline with comparatively lower octane ratings has been found to increase the octane rating which allows a greater compression ratio [Foo+14]. The larger enthalpy of vaporization, viscosity and surface tension of ethanol and a vapour pressure equal to that of the n-heptane and isooctane likely yields greater droplet sizes relative to the fuels in Table 3.1 and gasoline as indicated by the hollow cone spray measurements of [Zig+11] for several fuels. This behaviour has been confirmed for multihole sprays of E85 and gasoline at atmospheric conditions [Ale+10].

---

[3] Also referred to as parrafins.

[4] Also referred to as olefins or olefines.

One should also note that the slower initial rate of vaporization of ethanol in comparison with gasoline and resulting increase in liquid fraction at the same time during fuel injection is undesirable with respect to soot formation.

The vapour pressure of ethanol is lower than that of gasoline at ambient conditions [PBS00]. A blend of 85 % vol. ethanol and 15 % vol gasoline has a vapour pressure twice that of ethanol at 311 K [PBS00]. A greater vapour pressure aids in reducing cold start emissions particularly in PFI engines [SAW13].

The adiabatic constant pressure flame temperature of ethanol is approximately equal to that of the n-alkanes and isooctane. The laminar flame speed of ethanol is greater than isooctane [Bro+13], primary reference fuel 87 (PRF87: 87 % vol. isooctane, 13 % vol. n-heptane) and gasoline [Jer+09; Bro+13] at pressures ranging from 0.1 MPa to 1.0 MPa. For a small fraction of ethanol in isooctane and gasoline the laminar flame speed is approximately equal to that of the two major components at 0.1 MPa [Bro+13; Dir+14] and increases non-linearly towards that of ethanol as the fraction of ethanol in a ethanol/isooctane blend increases [Bro+13]. Based on the results of ethanol/isooctane blends, the laminar flame speed of E85 is expected to be close to that of ethanol and greater than isooctane and gasoline as a result. While the laminar flame speed of ethanol is expected to be larger than that of gasoline, under homogeneous conditions the rate of combustion is approximately equal [Ale+10]. In contrast to homogeneous operation, under lean stratified conditions the rate of combustion of E85 was observed to be larger compared to gasoline [OBM10; Fra11; SR12].

A reduction in NOx and soot with E85 relative to gasoline was observed by [SR13] in spray guided lean stratified combustion using a multihole injector. NOx was reduced further by delaying the start of injection towards TDC while soot was reduced slightly at a larger load and remained constant at a smaller load [SR12]. The reduction in emissions was achieved while maintaining combustion stability and operating at peak thermal efficiency. The lack of increased soot emissions as the start of injection was retarded nearer to TDC is in clear contrast to the increase in soot emissions observed for gasoline. The reduction of NOx and soot emissions relative to gasoline and decrease with delayed injection was also observed by [OBM10] with an outward opening piezo injector. Unburned hydrocarbon emissions were equal for E85 and gasoline in the study with the piezo injector. E85 was found by [Fra11] to increase the maximum load at which lean stratified combustion could be used relative to gasoline as determined by a particulate emission limit in a single cylinder engine with an outward opening piezo actuated injector. In the same study the specific fuel consumption corrected for lower heating values was larger for E85 below 2000 RPM and above this engine rotation frequency and an IMEP of 6 bar the fuel consumption was lower in comparison with gasoline. A reduction in NOx emissions was observed over the entire engine map while soot, CO and unburned hydrocarbon emission reductions were observed over a large fraction of the engine map. The studies mentioned demonstrate that in stratified combustion the use of E85 can reduce emissions compared to gasoline under the same operating conditions and further improvement is possible with later phasing of the start of injection with combustion. The reduction in emissions allow the lean stratified combustion to be used at larger engine loads given the equal emission limits for E85 and gasoline.

3.3.2 Gaseous Fuels

Hydrogen and methane are two possible gaseous fuels for internal combustion engines with advantages compared to conventional liquid fuels. Similarly to ethanol, both fuels can be produced with relative ease from renewable sources. The research octane number (RON) and motor octane number (MON) for methane are 120 which is significantly greater than the values of 92 to 98 and 80 to 90 respectively found for gasoline, as given by [Hey89]. This potentially allows increased compression ratios and thus an increase in efficiency for engines fueled with methane in comparison to gasoline, with an increase of the order of 5 % reported by [KNC11]. The advantages of hydrogen identified by [VW09] include wide flammability limits, low ignition energy, high auto ignition temperature and generally high flame speeds.

Hydrogen is distinct from the hydrocarbons and alchohols in Table 3.1 in that it contains no carbon. The oxidation of H_2 produces only H_2O rather than H_2O and CO_2 as is the case for hydrocarbon fuels. Hydrogen is a potentially carbon neutral fuel depending on the source and method of production. Hydrogen can be produced from electrolysis of water, where the electrical energy can potentially be sourced from renewable energy sources such as wind or solar power. This opens the possibility for a hydrogen based economy. One significant issue with hydrogen in transport is the issue of storage. While methane

3.4 Emissions

3.4.1 NOx

NOx is the collective term for NO and NO_2 which are classed as pollutants and are of concern due to their adverse health effects and their role in the formation secondary pollutants which include acid rain, tropospheric ozone (O_3) and secondary soot particulate matter precursors [Kuo05]. A number of formation mechanisms exist [Kuo05]:

1. Thermal NO mechanism (Zel'dovich NO mechanism)
2. Prompt NO mechanism
3. Fuel-bound nitrogen (FN)
4. NO_2 mechanism
5. N_2O mechanism

The first mechanism is significant in internal combustion engine NO formation. The mechanism involves N_2 oxidation and depends on temperatures on the order of 1000 K. The most widely used aftertreatment method for reducing NO and NO_2 emissions is catalytic reduction using three way catalysts (TWC). TWCs simultaneously oxidize CO and reduce NO when the engine is operated stoichiometrically. When the exhaust gas contains excess air, NO conversion efficiency decreases and TWCs are therefore unsuitable for globally lean combustion NOx aftertreatment. Other aftertreatment solution such as selective catalytic reduction (SCR) exist but require additional engine control strategies or reducing agents [FHG12].

3.4.2 Soot

Soot is the common term used for hydrocarbon particulate matter which is formed as a result of incomplete combustion of hydrocarbon fuels. It is amorphous and as such has no clearly defined structure. There is general agreement that the precursors to soot are poly aromatic hydrocarbons (PAH) which consist of interconnected aromatic rings formed by the addition of aromatic rings. The PAHs eventually coalesce to from amorphous particles which experience surface growth and coagulation with other particles. This process is illustrated in Figure 3.8.

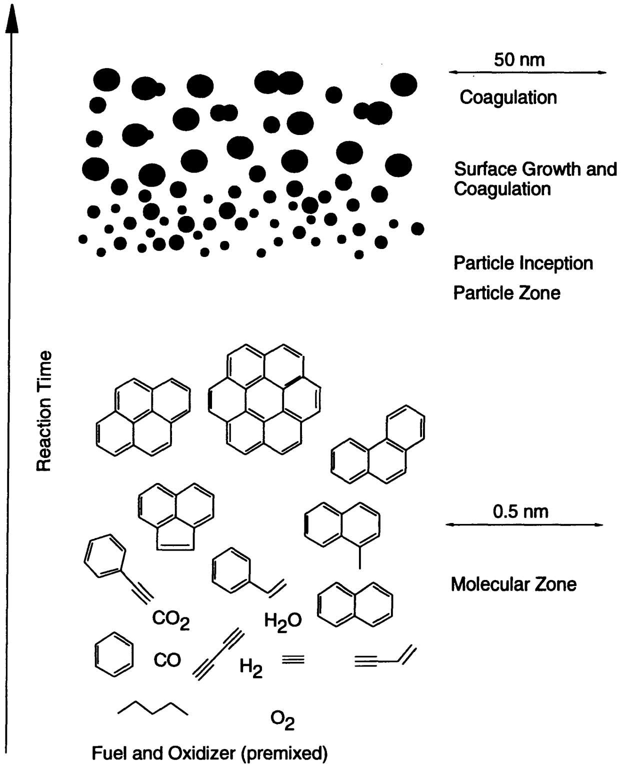

Figure 3.8: *Soot formation pathways. From [Boc94, Fig. 1].*

The mechanism of soot oxidation is the subject of ongoing research and has been shown to involve O_2 and the oxygen containing O and OH radicals amongst other species [Sta01; Boc94]. [FJ67] found that soot from premixed ethylene and acetylene flames was reduced by an order of magnitude when the oxidizer was changed from N_2O to O_2 while maintaining the same stoichiometry and flame temperature. Equal concentrations of the presumed aggregate precursor species were measured in both cases and the reduction in soot was attributed to the greater abundance of OH radicals from the O_2 and oxidation of the soot aggregates by OH. The formation, structure and oxidation of soot in a propane concentric co-flow diffusion flame at atmospheric pressure was investigated by [HNI14]. The soot size measured by Raman scattering of sampled soot and the soot volume fraction determined with laser induced incandescence decreased as the intensity of the laser induced fluorescence of OH increased suggesting soot oxidation by OH. Under diesel engine conditions the oxidation of soot in two diesel surrogate fuels was found in both cases to coincide with a decrease in CO from peak concentrations through oxidation by OH radicals by [Cav+94]. It was argued that the reduction in CO left more OH radicals available for the oxidation of soot through a parallel reaction with a lower kinetic rate to that involving OH and CO.

	Hydrogen	Methane	Methanol	Ethanol	n-Hexane	n-Heptane	Isooctane	Toluene
$(m_{\mathrm{air}}/m_{\mathrm{fuel}})_{\mathrm{s}}$	34.3	17.2	6.47	8.98	15.21	15.14	15.09	13.47
RON			106	108	24.8	0	100	118
MON			92	92.9	26	0	100	103.5
$p = 0.1\,\mathrm{MPa}$, $T = 298.15\,\mathrm{K}$								
Phase	Vapour	Vapour	Liquid	Liquid	Liquid	Liquid	Liquid	Liquid
$\rho/\mathrm{kg\,m^{-1}}$	$8.13{\cdot}10^{-2}$	$6.48{\cdot}10^{-1}$	786	785	659	680	704	862
T_{sat} $(0.1\,\mathrm{MPa})/\mathrm{K}$			337	351	342	371	372	383
p_{sat} $(298.15\,\mathrm{K})/\mathrm{kPa}$			17.0	7.87	20.3	6.09	6.54	3.79
$h_{\mathrm{sat},lv}$ $(0.1\,\mathrm{MPa})/\mathrm{kJ\,kg^{-1}}$			1101.8	849.4	330.2	317.2	311.3	361.6
$\nu/\mathrm{Pa\,s}$	$8.9{\cdot}10^{-6}$	$11.08{\cdot}10^{-6}$	$5.43{\cdot}10^{-4}$	$1.07{\cdot}10^{-3}$	$2.98{\cdot}10^{-4}$	$4.11{\cdot}10^{-4}$	$4.67{\cdot}10^{-4}$	$5.48{\cdot}10^{-4}$
$\sigma/\mathrm{N\,m^{-1}}$			$2.21{\cdot}10^{-2}$	$2.23{\cdot}10^{-2}$	$1.80{\cdot}10^{-2}$	$2.00{\cdot}10^{-2}$	$1.83{\cdot}10^{-2}$	$2.79{\cdot}10^{-2}$
$\mathrm{LHV}/\mathrm{MJ\,kg^{-1}}$	120	50.0	21.1	26.9	44.8	44.6	44.4	40.6
Flame $T_{\mathrm{ad},p}/\mathrm{K}$	2516	2322	2326	2348	2388	2390	2388	2481

Table 3.1: Thermodynamic and combustion properties of ethanol and of surrogate gasoline fuel component examples. Constant pressure adiabatic flame temperatures were calculated without including dissociation of the combustion products. Data sources [GHJ06; Foo+14; DP04; SW03a; SW03b; LS06; MW90; Yaw12; LM14; Som88]. Determination of thermodynamic and transport properties is discussed in greater detail in Appendix A

Chapter 4

Studies

In light of the significant contribution of passenger vehicles engines to the total anthropogenic GHG emissions and and CO_2 emissions in particular, reductions in this sector will help to minimize the effects of global warming. The two primary approaches to this end are:

1. Increase fuel efficiency
2. Reduce carbon intensity of fuels

The improvement of thermodynamic cycle efficiency of spark ignition engines belongs to the first approach and several possibilities exist in this regard. Globally lean, stratified combustion in direct injection spark ignition engines is one such possibility which can increase fuel efficiency through an increase in thermodynamic efficiency. Replacing gasoline with fuels available from renewable sources such as ethanol in conjunction with globally lean stratified combustion combines both approaches to reducing GHG emissions and offers the added benefit of potentially reducing soot emissions.

Combining the internal combustion engine with an electric motor to form a hybrid powertrain is an approach which which can potentially achieve both goals by allowing the internal combustion engine to operate at greater thermodynamic efficiency (the first approach) and by using electrical energy from renewable sources (the second approach).

The studies outlined in the following sections studied aspects of the above mentioned approaches to GHG emissions reductions from passenger vehicles with spark ignition engines. In particular, the common themes are the improvement of thermodynamic efficiency and emissions of direct injection spark ignition engines using stratified combustion and hybrid powertrains and the use of renewable alternative fuels.

4.1 Electric Assistance During Engine Load Transients

SIDI engines have larger particulate matter mass and number emissions in comparison to PFI engines over the NEDC cycle [BWS14]. Particulate numbers are largest during engine start [BWS14], are dependent on engine load [BWS14; BCL14; JHD13; Whi+11] and can increase by a factor of 2 during cold engine starts [BWS14].

Particulate matter emissions are known to occur during engine transients [Kar+14; Whi+11; BWS14; Mam+13] coinciding with air to fuel ratio transients [Whi+11; Sto+14]. Three way catalysts can effectively eliminate NOx, CO and unburned hydrocarbons (HC) emissions during stoichiometric engine operation [Hey89]. Gasoline particulate filters (GPF) have been demonstrated to be an effective aftertreatment solution for particulate matter [Joh13] with trapping efficiencies for direct injection engines ranging from 90% during hot engine starts to 99% during cold engine starts where particulate numbers are greater [Mam+13].

Hybrid combustion engine and electric powertrains is one technology with the potential to reduce emissions. Reductions in combustion engine fuel consumption can be achieved with parallel plug-in hybrids where part of the required energy is delivered by the electric grid and has no associated vehicle emissions. In addition to the use of electric grid energy, hybrid powertrains offer the possibility of energy recuperation through braking, providing a further reduction in fuel consumption.

Parallel hybrid powertrains provide a means of reducing the transient engine load by using the electric component of the powertrain to deliver part of the power required during a transient thereby reducing the combustion engine load and the need for a fast engine load response. As a result, the combustion engine load can be increased at a slower rate thereby ideally reducing emissions during transients due to sudden power demands and the desire for provided the electric powertrain component can deliver sufficient power.

4.1.1 Study

This study investigated the effect of simulated electric assistance during powertrain load transients on combustion engine emissions. The time resolved emissions during a modified New European Drive Cycle (NEDC) were measured for a drive cycle with power delivered exclusively by the combustion engine and a drive cycle with simulated electric motor assistance during the transients. The NEDC was chosen since the constant accelerations in the drive cycle provided a variety of clearly defined drive cycle transients in contrast to drive cycles which aim to simulate real world driving patterns more closely such as the Worldwide Harmonized Light Vehicles Test Procedure (WLTP) [Uni15]. Battery management and hybrid control strategy were not the focus of the investigation and the NEDC results should not be viewed as representing a viable real world hybrid drive cycle. The NEDC in this context should be viewed as a series of engine transient test segments.

Further details of this study can found in L. C. Johansen, I. Denbratt, and S. Hemdal. Drive Cycle Particulate and Gaseous Emissions from a Parallel Hybrid Combustion Engine and Electric Powertrain. *SAE Technical Paper 2015-24-2538* (2015). DOI: `10.4271/2015-24-2538`.

4.2 Soot Formation in E10 and E85 Stratified Combustion

The benefits of globally lean stratified combustion discussed in section 3.2 come at the cost of increased soot emissions [Fra11] and greater combustion instability [PRS14]. Ideally the stratified mixture would be confined to the vicinity of the spark plug and within the mixture the stoichiometry would be one. In practice this cannot be achieved and the local fuel to air ratio in the stratified fuel and air mixture varies from lean to rich. The injection and spark timing is a balance between allowing enough mixing to minimize locally fuel rich conditions and avoiding too much mixing which leads to locally fuel lean conditions at ignition and during the subsequent combustion process. Fuel rich regions provide conditions favorable to soot formation [Sta01] due to the insufficient fraction of oxidizers. Excessively fuel lean regions leads to poor flame propagation and quenching [PRS14].

In addition to these issues, injection of fuel close to top dead center (TDC) firing increases the chance of the fuel spray impinging on the piston due to the short distance between the piston at TDC and the injector. Fuel spray impingement on the piston can lead to liquid fuel films on the surface and which increase in volume as injection is delayed towards TDC [Dra+03]. Fuel films produce diffusion flames, referred to as pool fires, once combustion starts and this has been confirmed as a source of soot formation [Dra+03; Vel+10]. Soot particulate emissions increase in proportion with the fuel film mass [Dra+03]. Increases in soot incandescence [Hem+11] and soot emissions [Hem+11; OB13] as injection is delayed in spray guided engines with outward opening pintle injectors using gasoline suggest that part of the increase is similarly due to the increase in fuel film mass and diffusion combustion in pool fires. This has not been conclusively determined with gasoline or for E85 (85 % vol. ethanol, 15 % vol. gasoline).

Injecting earlier in the intake stroke would reduce the fuel impingement on the piston for a given design but this leads to increased fuel and air mixing and a lower average air to fuel ratio if the spark timing remains at the initial optimal timing. This leads to poorer flame propagation [PRS14] resulting in increased combustion instability and a reduction in work output [Oh+11; OB13]. Shifting both injection and spark to earlier in the compression stroke causes a greater fraction of combustion to occur during the compression stroke which also leads to a reduction in work output [OB13]. Injecting early enough to avoid fuel impingement entirely has not been possible without reducing work output and increasing combustion instability significantly for multihole injectors with gasoline [Vel+10].

4.2.1 Study

This study sought to determine the source of soot formation in E10 and E85 spray guided, globally lean, stratified combustion using a piezo actuated, outward opening, pintle injector and compare the results for the two fuels. The effect of split/multiple injection strategies on soot formation was also investigated. Two engine loads at 1500 RPM with a fully open throttle were investigated: 3.6 bar and 5 bar indicated mean effective pressure (IMEP). These loads led to globally lean engine conditions with the approximate fuel to air ratios of 0.37 and 0.66 with respect to stoichiometric ratios. The engine load points correspond to areas of the RPM-IMEP map at which a 2 litre spark ignition engine operates for a significant fraction of the NEDC cycle as evident from the study described in [JDH15]. Thermodynamic efficiency at these engine loads and emissions are therefore significant with respect to the drive cycles with similar load-speed profiles compared to the NEDC.

Further details of this study can found in:

- L. C. R. Johansen and S. Hemdal. In cylinder visualization of stratified combustion of E85 and main sources of soot formation. *Fuel* **159** (2015), 392–411. DOI: `10.1016/j.fuel.2015.07.013`
- L. C. R. Johansen, S. Hemdal, and I. Denbratt. Comparison of E10 and E85 Spark Ignited Stratified Combustion and Soot Formation. *Submitted to Fuel* (2016).

4.3 Gas Jet Structure

Direct injection of gaseous fuel into the engine cylinder improves volumetric efficiency and provides the possibility of more accurate fuel metering, as discussed in section 3.1. The injection of gas with a large upstream stagnation pressure from a circular nozzle in to a medium with a stagnation pressure on the order of a magnitude smaller, results in the creation of turbulent jets.

The flow and mixing process of transient gas jets affects combustion under homogeneous and stratified conditions. Natural gas jets have been found difficult to ignite during injection while ignition and combustion after the end of injection was stable, including under lean conditions [Moh+08]. For hydrogen jets stable ignition during injection was achievable [Moh+08]. Locating the spark near the boundary of the jet close to the nozzle and setting ignition to just after the start of injection was found to give stable ignition and control the combustion rate. Spark positioning at the jet tip or boundary

Transient turbulent jets issued from a round nozzle have been proposed by [HO99] as consisting of a spherical head vortex ahead of a quasi steady jet as illustrated in Figure 4.1, an extension from the original proposal of the model for buoyant plumes by [Tur62] according to [HO99]. After exiting the nozzle the velocity profile in the developing region of the jet transitions from the initial profile to a constant self similar profile in the fully developed region beginning at a distance variously given as between 10 to 20 nozzle diameters [SA03; HO99]. If the jet is underexpanded, a structure of expansion and shock waves also exist at the nozzle exit in order for the jet to reach the ambient pressure. This is illustrated in Figure 4.1 where the gas exiting the nozzle is underexpanded and therefore encounters expansion waves at nozzle exit and a barrel shock at the boundaries of the jet redirecting the flow away from the jet boundary. The gas finally encounters a Mach disk, which causes the pressure of the gas to reach that of the surroundings. The jet terminates in a rotating head vortex. The structure of the jet can in part be characterized by the penetration length of the jet and the angle between the boundaries of the jet as shown in Figure 4.1.

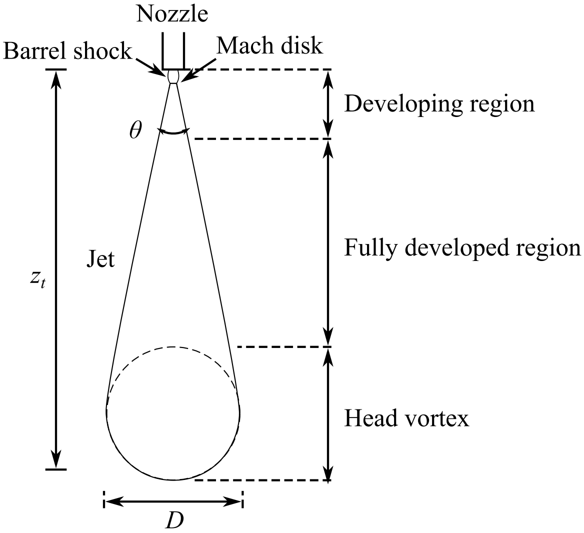

Figure 4.1: *Diagram of the model of a transient under expanded jet proposed by [HO99]. Modified from [SA03]*

Transient turbulent jets have been observed to exhibit self-similarity at a distance of 15 to 20 nozzle diameters from the nozzle exit with respect to ratio of the maximum jet width D and the penetration length z_t [HO99]. D/z_t therefore approaches a constant value. Eq. 4.1 has been derived from dimensional analysis for the penetration length of a compressible transient jet by [HO99].

$$z_t = \Gamma \left(\frac{\dot{m}_n v_n}{\rho_{\text{amb}}} \right)^{\frac{1}{4}} t^{\frac{1}{2}} \tag{4.1}$$

where $\dot{m}_n$ is the nozzle mass flow rate, v_n is the gas velocity at the nozzle, ρ_{amb} is the ambient density and t is the time that has elapsed from the start of injection. Γ is a function of the above stated ratio D/z_t. The Turner jet model, which describes a jet as a circular traveling vortex of diameter D ahead of a quasi-steady conic jet region, along with conservation of momentum and earlier mass entrainment results presented by [RS61] was used by [HO99] to derive an equation for Γ.

A value of 3.0(1) for Γ based on values for D/z_t of 0.25(5) determined from the images presented by [Riz58] for transient water jets. It is apparent that a factor 1.2 change in D/z_t leads to a factor change of 0.97 in Γ and that Γ is therefore relatively insensitive to the structure of the jet as quantified by D/z_t within the range stated of these parameters.

4.3.1 Study

The applicability of the Turner model and variability of the self similarity variable D/z_t under a range of pressure ratios was investigated given the importance of the ignition location in a gas jet as demonstrated by [Moh+08], and that direct ignition is likely to be required for an ignitable mixture in stratified combustion operation. Helium gas jets in air were chosen for the study due to the large difference in the index of refraction which applied itself to schlieren imaging and due to the inert nature of helium. A range of injection and ambient pressures were investigated.

Further details of this study can found in L. C. Johansen, E. de Benito Sienes, and P. Dahlander. Analysis of Transient Compressible Gas Jets Using High Speed Schlieren Imaging. *SAE Technical Paper 2013-01-0871* (2013). DOI: `10.4271/2013-01-0871`.

Chapter 5

Method

5.1 Electric Assistance During Engine Load Transients

Dynamometers provide the means to operate a powertrain on a drive cycle by imposing a predefined torque and rotational speed simulating the conditions imposed by a complete vehicle. The dynamometer imposed rotational frequency is determined from the final gear ratio and a defined vehicle speed profile for a drive cycle. The torque imposed by the dynamometers is determined from the road friction force, F_r and can be defined in terms of the vehicle speed. In this study the force was defined by Eq. Eq. 5.1.

$$F_r = C_f + C_v v + C_{vn} v^n + \frac{1}{2}\rho_{\text{air}} C_d A v^2 \tag{5.1}$$

where v is the vehicle speed, C_f is a constant friction force, C_v, C_{vn} are vehicle speed proportional friction constants, n is a vehicle speed exponent, C_d is the drag friction constant, A is the vehicle frontal area and ρ_{air} is the air density.The engine power requirement due to the road friction, P_r, was determined from Eq. 5.2.

$$P_r = F_r v \tag{5.2}$$

where v is the vehicle speed. The road friction power is not dependent on the vehicle mass and by extension the required engine work, as measured by the IMEP, due to road friction is also independent of vehicle mass. The power required to accelerate the vehicle, P_a, is dependent on mass and by extension the engine load due to acceleration is dependent on the vehicle mass as shown in Eq. 5.3.

$$P_a = m_{\text{vh}} a v \tag{5.3}$$

where m_{vh} is the vehicle mass and a is the vehicle acceleration. The engine load at constant vehicle speed will therefore be equal for two different vehicle mass while the engine load during acceleration consists of both the vehicle mass independent road load and the vehicle mass dependent acceleration load. As a result the engine load during acceleration will differ for different vehicle masses. The total power requirement is the sum of Eq. 5.2 and Eq. 5.3 as shown in Eq. 5.4.

$$P_\mathrm{t} = P_a + P_r = \left(m_\mathrm{vh} a + C_f + C_v v + C_{vn} v^n + \frac{1}{2} \rho_\mathrm{air} C_d A v^2 \right) v \tag{5.4}$$

By varying the vehicle mass the engine load during acceleration could be adjusted while maintaining the same engine load during constant vehicle speeds. This was utilized to simulate constant electric motor assist to reduce engine load during accelerations by reducing the vehicle mass. This allowed a more controlled study of the effect of engine load reduction during acceleration on emissions due to the well defined engine load reduction and avoiding the effects of gear changes on the electric motor. The electric motor was not used for this reason.

5.2 Soot Formation in E10 and E85 Stratified Combustion

An optical engine, an engine which can emulate conditions in a metal engine cylinder, provides the possibility to use both optical and pressure diagnostics in order to investigate engine cylinder combustion phenomena.

5.2.1 Cylinder Pressure

As discussed in greater detail in Appendix B, the rate of heat release $\mathrm{d}Q_\mathrm{ch}$ provides a time resolved view of combustion in the cylinder. The rate of heat release is the time rate of conversion of chemical energy to sensible energy. The cumulative heat release at a given point is proportional to $x_b\,[-]$, the mass fraction of the fuel which has combusted. From the total heat release it is possible to determine the crank angle duration of combustion, the crank angle at which 50% of the fuel has combusted (CA50), stability, variation, abnormal combustion and combustion efficiency, as discussed by [Hey89], which can be used to characterize and analyze the combustion process.

The rate of heat release is not directly measurable. The most readily measurable quantity providing a measure of the combustion process in a cylinder is the cylinder pressure p. The cylinder pressure increases as combustion progresses due to the resulting increase in cylinder gas temperature T. The pressure is therefore a function of the rate of heat release and this relationship provides a way of determining the rate of heat release from the cylinder pressure. However, the cylinder pressure also changes due to additional thermodynamic variables.

The goal of heat release analysis is to separate the effect of combustion on the cylinder pressure from the effects of any other phenomena. The accuracy of any method relating cylinder pressure to heat release will therefore depend on which of the phenomena other than combustion are accounted for, the accuracy of the models for the phenomena, and the magnitude of the effect of each neglected term on the cylinder pressure, relative to combustion.

5.2.2 Imaging

Light in the visible spectrum can be used to investigate a number of phenomena in internal combustion engines [Sic13]. Mie scattering of diffuse light by liquid fuel can be used to image fuel while chemiluminescence from species involved in combustion and soot incandescence in the visible spectrum can be used to image combustion and flame propagation. Imaging of these phenomena collects all light emitted along a line of sight and thus provides a 2-dimensional projected view of 3-dimensional phenomena. This is generally referred to as line of sight imaging. The methods described in subsection 5.2.3, subsection 5.2.5 and subsection 5.2.4.

5.2.3 Emission Spectrum

The spectrum of the emitted electromagnetic radiation from the spark and combustion was measured to identify chemical species present during the ignition and subsequent combustion of the fuel and air mixture, and to select appropriate filters for the OH^* chemiluminescence and soot incandescence measurements.

5.2.4 Soot Incandescence

Soot particles formed during combustion have a temperature equal to that of the surrounding gases and emit broadband thermal radiation in the visible and infrared spectrum [ZL98; Mod13]. A soot particle can be modelled as a blackbody with a wavelength dependent emissivity. Based on this model the spectral intensity of the luminescence emitted by a volume containing soot particles is a function of the temperature and wavelength according to Planck's law, the number of particles and the size distribution of the particles. The radiation emitted from a soot particle can be scattered and absorbed by other soot particles. Due to this the soot incandescence detected along an optical path through a region containing soot is also a function of the soot density and path length. The effect of the soot density and optical path length can be roughly quantified in terms of a KL factor, where K is an absorption coefficient proportional to the number density of soot particles and L is the path length of the radiation [ZL98].

This characteristic of soot particles can be used to optically detect soot particulates by long pass filtering to image the red end of the visible spectrum in which soot incandescence dominates as has been observed previously in stratified engine operation [Sto+05; Hem+11]. The method is line of sight and the signal intensity depends on the temperature, wavelength dependent emissivity and number of the soot particles along a line of sight. As a result of the dependency on other factors than particle number alone, soot incandescence does not provide a direct measure of soot emissions although in two studies [Hem+11; OB13] a correlation has been observed between the two measurements.

5.2.5 OH Chemiluminescence

The radical OH is created during oxidation of hydrocarbons as a product of chain branching and propagating reactions and is a reactant in exothermic chain propagating reactions

[GY08, Ch. 3]. In reaction mechanism models of ethanol [Lep+11] and E85 [DT08] oxidation, OH is involved in the initial decomposition of ethanol. Based on these results the presence of OH is an indication of oxidation of E85 and conditions conducive to the oxidation of soot. OH in the first higher electronic state, denoted OH*, emits radiation centered in a narrow band around 306 nm when relaxing to the ground electronic state at the temperatures present in flames [Gay74; DC62]. OH* can occur as the product of chemical reactions [Gay74] and the emitted luminescence is referred to as chemiluminescence. In hydrocarbon flames the reaction in Eq. 5.5 is a source of OH* [Por+67; CVP03].

$$\mathrm{CH} + \mathrm{O_2} \longrightarrow \mathrm{OH^*} + \mathrm{CO} \tag{5.5}$$

The OH* chemiluminescence intensity is dependent on the local temperature and chemical composition [DV92]. Soot particles attenuate OH* chemiluminescence in the same manner as with soot incandescence [Hem+11] and due to this the OH* chemiluminescence intensity decreases as the line of sight soot density increases. Spatially and temporally resolved OH* chemiluminescence and soot incandescence was measured by [Sto+05] using two bandpass filtered cameras and used to study soot formation, soot density and soot temperature using two colour pyrometry in wall guided stratified combustion of gasoline using a multihole injector in a single cylinder optical engine. Crank angle averaged and spatially resolved OH* and soot incandescence was used by [Hem+11] to study soot formation and oxidation in spray guided combustion of gasoline using a piezo outward opening injector.

5.3 Gas Jet Structure

Many gases are not visible in the visible spectrum and helium is an example of such a gas. Helium was used in the study due to the ease with which it can be visualized using the schlieren technique. Schlieren imaging allows the visualization of spatial gradients in the refractive index. Schlieren imaging can in general not provide quantitative data, although techniques do exist for special conditions such as laminar and radially symmetric flows which are discussed by [Set01]. The refractive index varies by species and wavelength and density. The refractive index of an ideal gas is also related to density by Eq. 5.6 as given by [Set01]. As a result, schlieren imaging can be used to provide images of density gradient and species gradients.

$$n - 1 = k\rho \tag{5.6}$$

where k is the Gladstone-Dale coefficient. As light parallel to the optical axis x passes through a refractive index gradient along an axis z perpendicular to x, it will be refracted by an angle ε_z. The refraction angle for a light ray passing through such a constant gradient of length L with a surrounding medium refractive index n, can be determined from Eq. 5.7 as given by [Set01].

$$\varepsilon_z = \frac{L}{n}\frac{\partial n}{\partial z} \tag{5.7}$$

Only non-uniform refractive index spatial gradients perpendicular to the light ray can be made visible with schlieren imaging, i.e. $\partial n/\partial z$ must vary along z. If the entirety of the source light passes through a uniform refractive index gradient, an equal refraction will occur according to Eq. 5.7. Placing a mask at a focal point following refraction due to non-uniform refractive index gradients provides a means of visualizing regions where these gradients occur. A fraction of the light is cut-off by the mask at the focal point. Light refracted perpendicular to the mask edge will be affected by a different cut-off than unrefracted light and light refracted parallel to the mask edge. A schlieren image is captured from light that has passed the mask at the focal point. Depending on the sign of the refraction angle and the mask placed at the focal point, an increase or decrease in illuminance relative to an image of wholly unrefracted light will occur.

At a vacuum wavelength of 500 nm and a pressure of 0.1 MPa and a temperature of 273 K, air and helium have refractive indices of 1.000 294 and 1.000 035 respectively [Cid96; MP69]. In the present experiment refraction occurred in the presence of species gradients, due to the difference in refractive index between the chamber air and injected helium.

Chapter 6

Experiment Apparatus and Setup

6.1 Electric Assistance During Engine Load Transients

The investigation was conducted using a three cylinder, turbocharged, direct injected gasoline engine mounted to a 7 speed dual clutch automatic transmission with an integrated electric motor. The engine and transmission together constituted a hybrid gasoline and electric power unit. Cylinder pressure sensors were used to determine the indicated mean effective pressure (IMEP) and combustion phasing. The engine specifications are given in Table 6.1. The transmission was limited to vehicle speeds of $100\,\mathrm{km\,h^{-1}}$ during the investigation. The integrated electric motor was connected via an electric motor clutch to the even gear shaft. During gear shifts on the even gear shaft the electric motor clutch disengaged and the electric motor could not deliver power. The layout of the transmission is shown schematically in Figure 6.1.

Induction	Turbocharged
Number of cylinders	3
Bore	82 mm
Stroke	82 mm
Displaced volume	1.3 L
Compression ratio	10.8
Fuel injection	Direct injection
Injector type	Solenoid, multihole
Fuel	Gasoline, RON 95

Table 6.1: Engine specifications

The engine and transmission were connected to two transient dynamometers which imposed the load specified by Eq. 5.4. The values used for the constants in Eq. 5.4 are

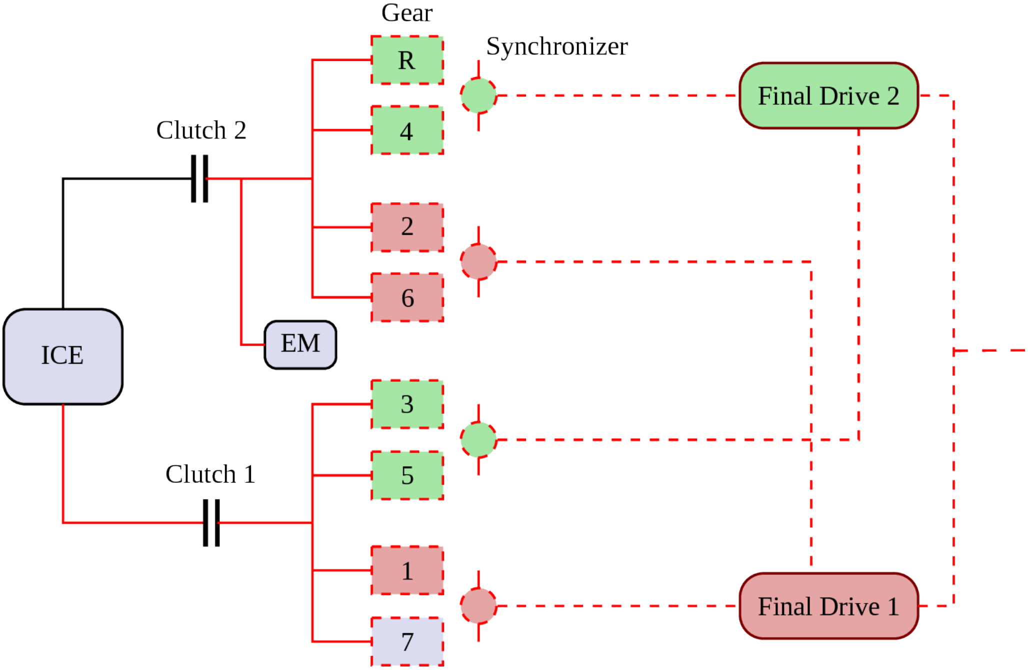

Figure 6.1: *The layout of the transmission with integrated electric motor. ICE: internal combustion engine, EM: electric motor. Numbers represent gear numbers. Reproduced from a figure provided by Rickard Arvidsson, Volvo Cars*

given in Table 6.2.

C_f	72.640 N
C_v	5.183 N/ (m/s)
C_{vn}	0.325 N/ $(\mathrm{m/s})^n$
n	2
ρ_{air}	1.164 $\mathrm{kg/m^3}$
C_d	0.320
A	2.315 $\mathrm{m^2}$

Table 6.2: Values used for the road load constants in Eq. 5.4

6.1.1 Emission Measurements

The exhaust gas composition was measured with an FTIR emission analyzer with a sample rate of 10 Hz. The exhaust mole concentration of infrared active species were measured using the FTIR emission analyzer, yielding the concentrations of H_2O, CO_2, CO, NO, NO_2 and hydrocarbons. The exhaust soot particulate mass (PM) concentration was measured with an AVL Micro Soot Sensor utilizing a photoacoustic measurement method [Arn+99; Gie+14]. The soot particulate number (PN) and size distribution was measured using a Cambustion DMS500 MKII utilizing a differential mobility analyzer (DMA) measurement method where the inertia and path deflection of charged soot particles are used to determine the size of the particles [KBW11; Gie+14]. A broadband lambda sensor measured the engine air to fuel ratio relative to the stoichiometric ratio from the exhaust gas. All emission measurement equipment sampled directly from the exhaust pipe between the turbocharger turbine exit and the three way catalyst without using a constant volume sampling (CVS) tunnel providing dilution. As a result, the emission measurements do not conform to Euro 6 measurement standards [The07] or the UN/ECE Particulate Measurement Programme (PMP) [Gie+12]. The measurement serve to compare the engine out emissions for pure gasoline engine operation and simulated electric motor assist during acceleration rather than emission levels in relation to legislative limits.

6.2 Soot Formation in E10 and E85 Stratified Combustion

An AVL 5411.018 single cylinder optical engine with a pent roof cylinder head was used in this study. A piezo actuated, outward opening, pintle needle fuel injector and a triple electrode spark plug were mounted in the center of the combustion chamber roof between the intake valves and the exhaust valves. A diagram of the engine is shown in Figure 6.2. Fixed engine parameters are given in Table 6.3.

Bore	83.06 mm
Stroke	90 mm
Connecting rod length	139.5 mm
Compression ratio	10.1
Displacement volume	$0.488 \cdot 10^{-3}$ m^3
Clearance volume	$0.535 \cdot 10^{-4}$ m^3
Number of intake valves	2
Intake valve diameter	33 mm
IVO/IVC (aTDC firing)	340/-120 CAD
Number of exhaust valves	2
Exhaust valve diameter	28 mm
EVO/EVC (aTDC firing)	105/-355 CAD
Swirl and tumble	No swirl and low tumble
Injector	piezo actuated outward opening pintle
Stratified operation	spray guided
Fuel pressure	205 bar

Table 6.3: Single cylinder optical engine specifications

The engine was operated at a fixed rotational speed. An AVL 4210 instrument con-

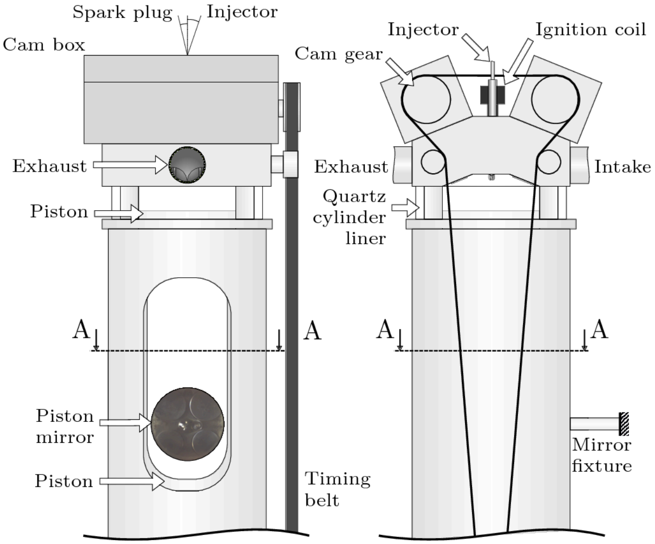

Figure 6.2: *Diagram of the optical single cylinder engine. The piston mirror camera and cylinder liner camera faced the engine sides shown to the left and right respectively. The section corresponding to the A–A cut plane is shown in Figure 6.6*

troller was used to generate trigger pulses beginning or ending at a specified crank angle with a specified crank angle or time duration. All experiments were conducted with a constant ignition coil charging duration with the aim being a constant spark energy. The trailing edge of the ignition coil trigger initiated the spark and the spark timing was controlled by shifting this edge. The start of spark (SOS) timings given in this paper are the ignition coil trigger trailing edge timings. The start of injection and injection durations and delay between injections were controlled in a similar manner with trigger pulses to the injector driver unit. The AVL 4210 was used to trigger a digital delay generator which in turn generated trigger pulses to the injector driver. The start of injection was initiated by the leading rising edge of the first trigger pulse to the injector driver. The start of injection (SOI) timings given in this paper correspond to the timing of the leading edge of the injector driver trigger pulse. The injection duration t_{inj} was defined as the duration between the rising leading edge and falling trailing edge of the injection trigger signal. The delay duration d_{inj} between injections was defined as the duration between the falling trailing edge of one injection and the rising leading edge of the next injection.

Commercial, certified test fuels were used. Fuel properties and compositions are given in Table 6.4. The fuel was supplied to the injector at a pressure of 205 bar. A wide band fuel to air ratio sensor was mounted in the exhaust pipe.

The engine could not be operated continuously as this would cause the quartz components of the engine to fracture and fail. As a result the engine component temperatures

Property	E10	E85
Density (288.15 K)	749.4 kg/m^3	787.3 kg/m^3
Vapour pressure	59.4 kPa	36.6 kPa
Water	308 mg/kg	200 mg/kg
Ethanol	10.1 % vol.	86.4 % vol.
MTBE	< 0.5 %vol.	2.9 %vol.
Initial boiling point	309.0 K	
Final boiling point	457.5 K	354.0 K
Lower heating value	43.9 MJ/kg	29.2 MJ/kg

Table 6.4: Properties and composition of the E10 and E85 fuels used in the experiments

increased while the engine was fired. Skip firing of the engine in order to achieve quasi steady state temperatures was not feasible due to the accumulation of soot on the quartz piston crown prior to achieving a quasi steady state.

6.2.1 Cylinder Pressure

A differential piezo pressure sensor was used to measure the change in cylinder pressure. The sensor was mounted horizontally on the side of the intake valves. The opening to the pressure sensor is indicated in Figure 6.4. The cylinder pressure was measured for a duration of 100 cycles for each experiment. The same measurement duration was used for measuring the motored engine cylinder pressure. In the crank angle range −45 CAD to 45 CAD the pressure was recorded at intervals of 0.1 CAD and otherwise at intervals of 1 CAD. The indicated mean effective pressure (IMEP) and heat release were calculated from the pressure measurements. The intake manifold pressure was 95.9 kPa.

The crank angle at which 50 % of the fuel had oxidized (CA50) and the rate of heat release ($\mathrm{d}Q_{\mathrm{ch}}/\mathrm{d}t$) was determined from the cylinder pressure from energy conservation for a single control volume with the specific heat ratio replaced by a polytropic coefficient. This is stated in Eq. 6.1 where Q_{ch} is the rate of heat release, t is time, κ is the polytropic coefficient, p is the measured cylinder pressure, V is the cylinder volume and θ is the crank angle. The polytropic coefficient was determined from linear interpolation between the compression and expansion values obtained from least square fits in a manner inspired by an earlier more elaborate method [Tun09]. Heat losses are incorporated by κ.

$$\frac{\mathrm{d}Q_{\mathrm{ch}}}{\mathrm{d}t} = \left(\frac{\kappa}{\kappa-1} p \frac{\mathrm{d}V}{\mathrm{d}\theta} + \frac{1}{\kappa-1} V \frac{\mathrm{d}p}{\mathrm{d}\theta} \right) \frac{\mathrm{d}\theta}{\mathrm{d}t} \tag{6.1}$$

6.2.2 Imaging

A quartz window was mounted in each of the two pent roof gables in the cylinder head. The head was mounted on top of a quartz cylinder liner with a height of 25 mm with a metal ring join between the two. The vertical distance from the injector tip to the piston surface at top dead center was 12 mm. The distance from the injector tip to the spark gap was 8 mm. The piston was visible through the quartz cylinder liner between −60 CAD and 60 CAD after top dead center (aTDC) firing.

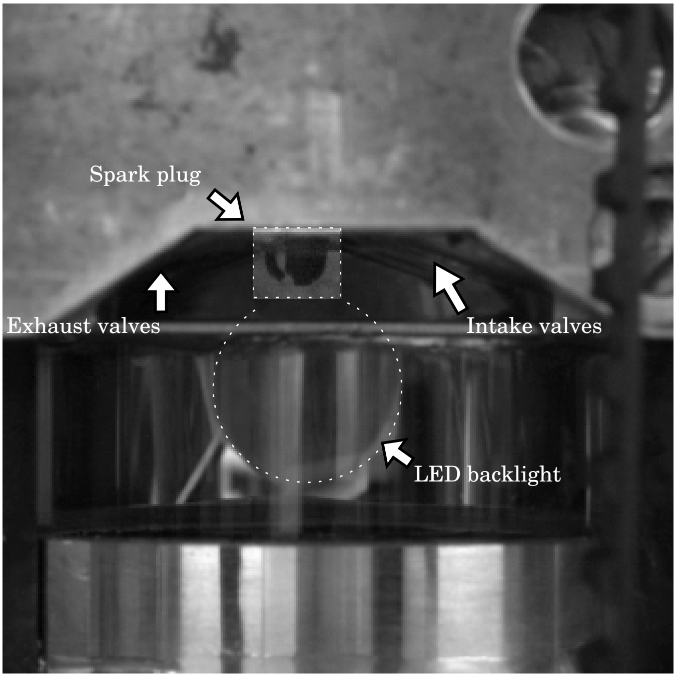

Figure 6.3: *The combustion chamber as viewed through the quartz cylinder liner and the pent–roof windows. Contrast stretching has been applied in region of image contained within the spark plug bounding box*

An elongated piston with a flat quartz window crown was used in the engine. The quartz piston crown provided a view of the combustion chamber along the cylinder axis by means of a mirror positioned below the piston in a Bowditch configuration [Bow61]. The mirror was inclined at an angle of 45° with respect to the cylinder axis and was visible through a slot in the elongated piston skirt as illustrated in the diagram on the left in Figure 6.2.

Figure 6.4 shows the combustion chamber and cylinder head as viewed from below through the quartz piston crown using the piston mirror. The pent roof quartz windows are located on the left and right hand sides of the combustion chamber image in Figure 6.4. The position of the injector tip and the spark plug tip is shown in Figure 6.4. The injector was inclined 20° clockwise from the cylinder axis in the plane of the diagram on the left in Figure 6.2 and the spark plug was inclined 10° counter clockwise. The inclinations are indicated in Figure 6.2. Images of the spark ignition and flame development were recorded from the side of the combustion chamber through the quartz cylinder liner. Monochrome Vision Research v7.1 and v1210 cameras were used to capture images for E10 and E85 respectively at a frame rate of 20 kHz. At 1500 RPM the frame frequency

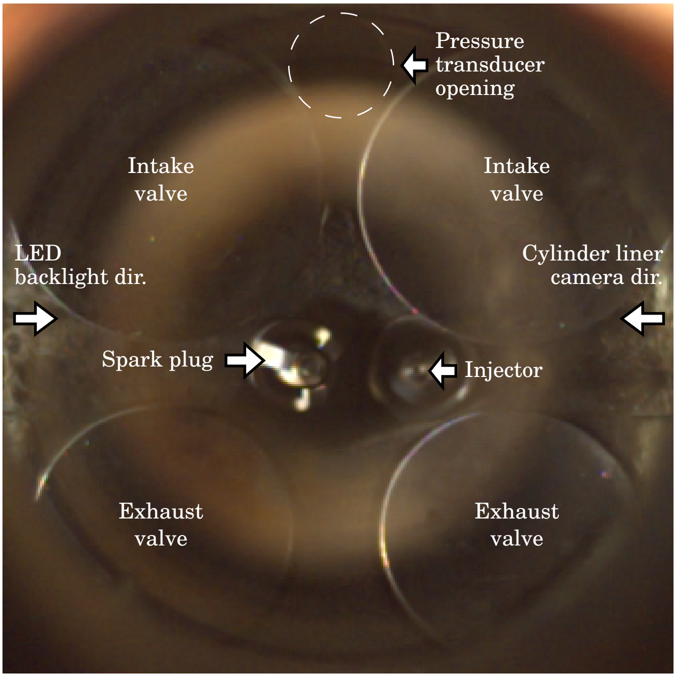

Figure 6.4: *The combustion chamber viewed from below through the quartz piston crown. The bright ring is due to reflection of light on the piston crown window.*

corresponds to an crank angle interval of 0.45 CAD with an exposure corresponding to 0.4 CAD. The crank angle calculated for each image has a maximum error of 0.4 CAD relative to the true crank angle.

6.2.3 Emission Spectrum

The luminescence and incandescence passing through the quartz piston crown and reflected by the piston mirror were analyzed. The radiation measured is the line of sight sum along the cylinder axis. The apparatus arrangement used for the spectrum measurements is illustrated in Figure 6.5.

A plate beamsplitter with 70% reflection and 30% transmission was used to direct luminescence towards the spectrometer arrangement. The luminescence was focused by a lens on to a fixed vertical slit with a width of 0.25 mm. The radiation passing through the slit was directed on to a reflecting diffraction grating and the diffracted radiation was reflected on to a Hamamatsu C9548–04 image intensifier. The image intensifier was used as a sensor for incident radiation in the wavelength interval 185 nm to 900 nm. The incident electromagnetic radiation signal was amplified and converted to broad spectrum electromagnetic radiation with a peak at 530 nm. The output of the intensifier was recorded using a Vision Research v7.1 video camera, designated as the spectrum camera. The camera was operated with a frame frequency of 9009 Hz. The frame frequency

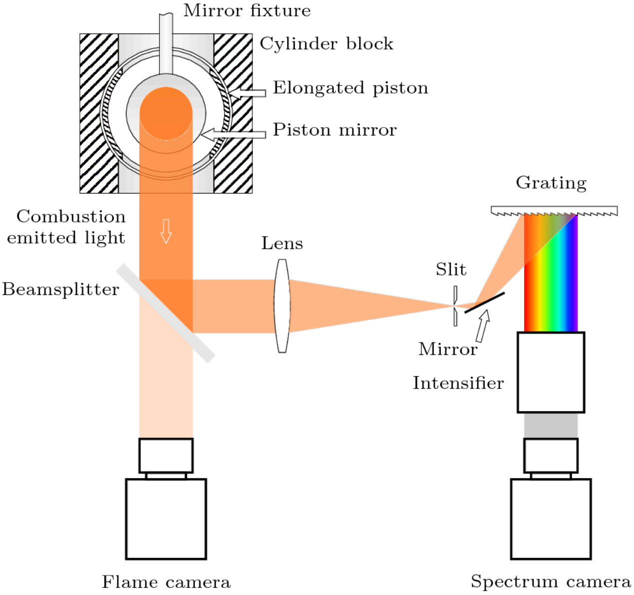

Figure 6.5: *Diagram of the optics arrangement used to measure the spectrum of the emitted radiation. The arrangement is viewed from above. The location of the cut plane for the engine section shown is indicated by the A–A cut plane in Figure 6.2*

corresponds to an crank angle interval of 1 CAD between recorded images at 1500 RPM. The exposure time was 100 μs with a corresponding crank angle duration of 0.9 CAD.

The vertical slit limited the area of the combustion chamber measured by the spectrometer to a rectangle delimited by the bounding box shown in Figure 7.9. The spectrum measurements were spatially resolved along the length of rectangle with a scale of 0.3 mm.

The spectrometer arrangement was calibrated with a Hg lamp. A wavelength interval of 193 nm to 847 nm was measured with a wavelength scale of 0.8 nm.

The luminescence transmitted by the beamsplitter was used to record images of the spark and combustion using a Vision Research Miro M310 frame synchronous with the spectrum camera and designated as the flame camera. The exposure time was equal to the spectrum image exposure times.

6.2.4 OH* Chemiluminescence and Soot Incandescence

The chemiluminescence emitted from OH^* and soot incandescence was measured simultaneously with the arrangement illustrated in Figure 6.6. The measured radiation at each pixel is the line of sight sum approximately along the cylinder axis.

A dichroic mirror with a wavelength center at 308 nm and a full width at half maximum (FWHM) of 50 nm reflected the OH^* chemiluminescence towards a bandpass filter centered at 308 nm with FWHM of 10 nm. A Hamamatsu C9548–04 intensifier equipped

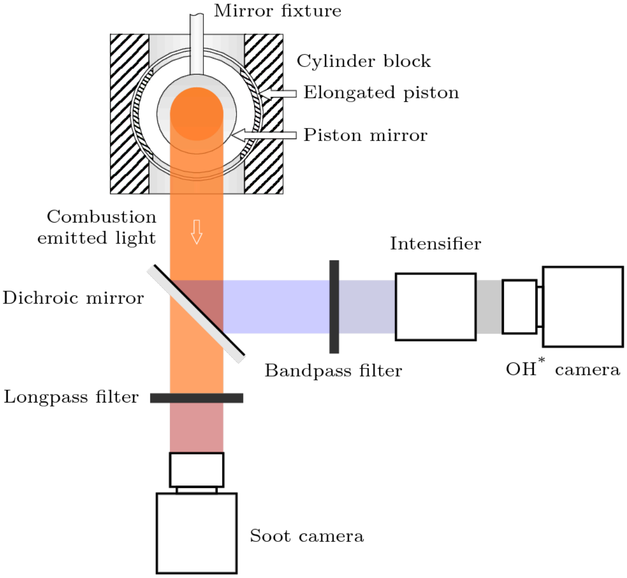

Figure 6.6: *Diagram of the optics arrangement used to measure the OH* chemiluminescence and soot incandescence. The arrangement is viewed from above. The location of the cut plane for the engine section shown is indicated by the A–A cut plane in Figure 6.2*

with UV transmitting 100 mm lens set to f/1.4 was used as a sensor for the luminescence transmitted through the bandpass filter. The intensifier amplified the transmitted luminescence and the output of the intensifier was recorded using a Vision Research v7.1 video camera, designated as the OH^* camera.

The luminescence and incandescence transmitted through the dichroic mirror was filtered with a longpass filter with a cut on wavelength of 610 nm. This filtered the luminescence from Na observed in the E85 flame emission spectrum in a previous study by the authors with the same fuel [JH15b]. The filtered broadband radiation was recorded with a Vision Research Miro M310 video camera, designated as the soot camera. The cameras were frame synchronized and for E10 were operated at 10 kHz with exposures of 98 μs and 89 μs for the OH^* and soot images respectively. For E85 the cameras were operated at 9 kHz with an exposure of 100 μs for both sets of images.

6.3 Gas Jet Structure

A modified multihole, solenoid actuated, gasoline injector designed for direct injection engines was used for gas injections. The original six-hole tip of the injector was removed and a single-hole nozzle was substituted. The nozzle was mounted by means of a thread cut into the injector. The number of turns with which the nozzle was fastened determined the effective needle lift and thereby the throat area located between the ball at the end

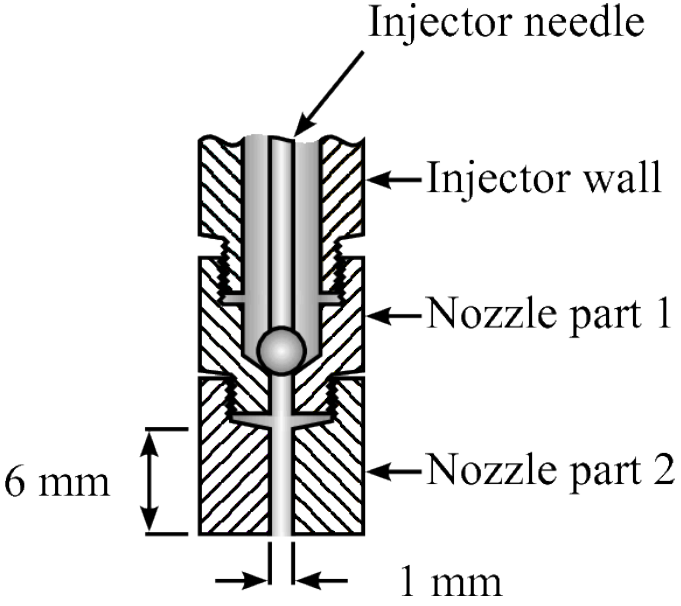

Figure 6.7: *Injector nozzle design*

of the injector needle and the inclined surface of the ball seat. The nozzle assembly is illustrated in Figure 6.7.

Gas injections occurred into a constant flow pressure chamber. The chamber had a square cross section externally and a circular cross-section internally. Optical access was provided by a circular window on each side of the chamber with a diameter of 110 mm. A dual field lens schlieren arrangement has been used to visualize the helium gas jets created in the pressure chamber with the modified injector. A Vision Research Phantom v7.1 camera has been used to capture schlieren images at a frame rate of 10 kHz. The arrangement of the pressure chamber, injector, schlieren optics and the image acquisition is illustrated in Figure 6.8.

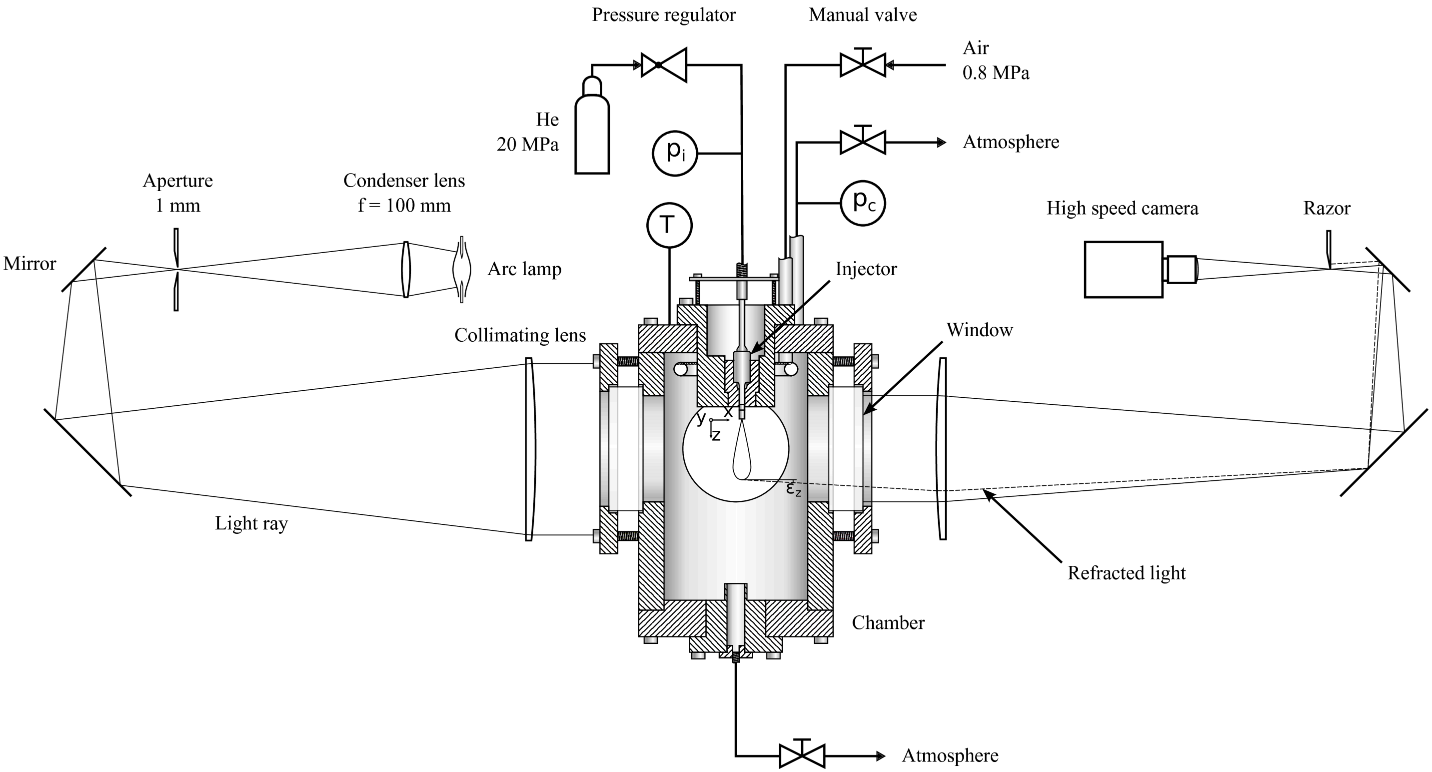

Figure 6.8: *Arrangement of gas injector, the constant pressure chamber with optical access and the schlieren optics and image acquisition*

Chapter 7

Results

7.1 Electric Assistance During Engine Load Transients

The time resolved drive cycle emissions were investigated for vehicle mass values of 1600 kg and 800 kg. This represents a reduction in maximum required acceleration power from 12.8 kW to 6.1 kW and thus a maximum required electric motor power of 6.7 kW in the simulated electric motor assistance case. This was using Eq. 5.3 with acceleration determined from the speed profile with the central difference method. In both cases the engine and catalyst were preheated prior to the measured drive cycles by idling the engine until the engine and exhaust gas temperatures reached steady state.

The 1600 kg vehicle mass value represents gasoline operation exclusively and the 800 kg vehicle mass represents gasoline operation with simulated electric motor assistance during vehicle acceleration and by extension during powertrain load transients. As discussed in the previous section, the smaller vehicle mass resulted in a smaller engine load during drive cycle transients compared to the larger vehicle mass while the engine load during constant drive cycle vehicle speeds was equal in both cases. The 800 kg vehicle mass was used to simulate electric motor assistance during acceleration due to the lower engine load during acceleration. The engine load was defined in terms of the mean of the indicated mean effective pressure measured for each engine cylinder. The IMEP is shown in the second plot from the top in Figure 7.1. The engine mean IMEP was equal for both pure engine operation and simulated electric boost during drive cycle idle periods $\left(0\,\mathrm{km\,h^{-1}}\right)$ and during drive cycle intervals with constant vehicle speeds as required with the sole exception of the second last constant speed segment of the EUDC segment. For the 800 kg vehicle mass test the automatic transition selected a lower gear during this segment resulting in a lower engine load. The IMEP during acceleration was smaller for the 800 kg vehicle mass which represented simulated electric assistance compared to the 1600 kg vehicle mass representing pure gasoline operation consistent with the dependency of the required acceleration power on vehicle mass per Eq. 5.3. The difference in IMEP between the two cases is particularly apparent during the accelerations in the EUDC segment of the NEDC in Figure 7.1. Similar differences in IMEP occur during accelerations in the ECE 15 segments which is more clearly seen in Figure 7.2 and Figure 7.3 in which the first and last ECE 15 segments are shown.

7.1.1 Air to Fuel Ratio

In both cases the air to fuel ratio relative to the stoichiometric ratio, λ, was 1 during engine idling and constant vehicle speeds. Deviations from this value occurred during engine load transients and gear changes to higher and lower gears due to engine speed transients. Both occurred during acceleration and deceleration. Accelerations led to fuel rich ($\lambda < 1$) air and fuel mixtures at the onset of the acceleration for both tests. During accelerations in both the first and last ECE 15 segment λ decreased to 0.9 in both cases as shown in greater detail in Figure 7.2 and Figure 7.3 respectively. Fuel rich conditions are thought to occur due to air mass flow transients and inaccurate fuel dosage by the engine control unit as a result. The decrease in λ was also observed by [Sto+12] at the onset of wide open throttle accelerations and by [Sto+14] during a throttle position step change. The smallest λ values after engine start were observed during gear changes at the beginning of the last constant speed segment of the ECE 15 segments during a gear change accompanied with an engine load spike for which the λ value decreased to 0.85 as shown in Figure 7.2 and Figure 7.3 for the first and last ECE 15 segments respectively. Fuel rich λ values occurred longer during downshifts for the 800 kg test as can be seen in the first and last ECE 15 segments, particularly at the end of the second segment in the ECE 15 segments as shown in the plots. The smallest λ value occurred during the engine start in both cases due to excessive throttling with λ values of 0.84 and 0.8 respectively for 1600 kg and 800 kg vehicle mass tests as shown at 0 s s in Figure 7.1 and in Figure 7.2 in greater detail. At maximum vehicle speed during the EUDC segment the engine operated fuel rich continuously with $\lambda = 0.98$ to avoid knock. Fuel lean conditions occurred during deceleration due to fuel shut off prior to gear changes.

7.1.2 NOx

NOx emissions are dependent on engine load, as demonstrated by the IMEP and NOx plots in Figure 7.1. The NOx emissions plot closely mirrors the engine mean IMEP. This is particularly apparent when comparing the IMEP and NOx during the EUDC segment. This is due to increased engine mass flow at greater engine loads coupled with the cylinder gas temperature increasing with engine load and the temperature dependence of NOx formation [Hey89]. The NOx emissions were lower for the 800 kg vehicle mass throughout the the drive cycle relative to the 1600 kg vehicle mass test as shown in Figure 7.1, due to the smaller engine load during accelerations. The EUDC segment of the NEDC cycle accounted for the majority of the total NOx emission in both tests due to a larger average engine load over the course of the segment compared to the preceding ECE 15 segments. The EUDC segment accounted for approximately 75 % of the total NOx emissions in both cases.The total NOx emissions per unit mass of fuel, given in Table 7.1, was 10 % smaller for the 800 kg vehicle mass test. This is attributed to the smaller engine load during accelerations which represented simulated electric motor assist. This in combination with the lower fuel consumption for the smaller vehicle mass test resulted in lower NOx emissions per kilometer.

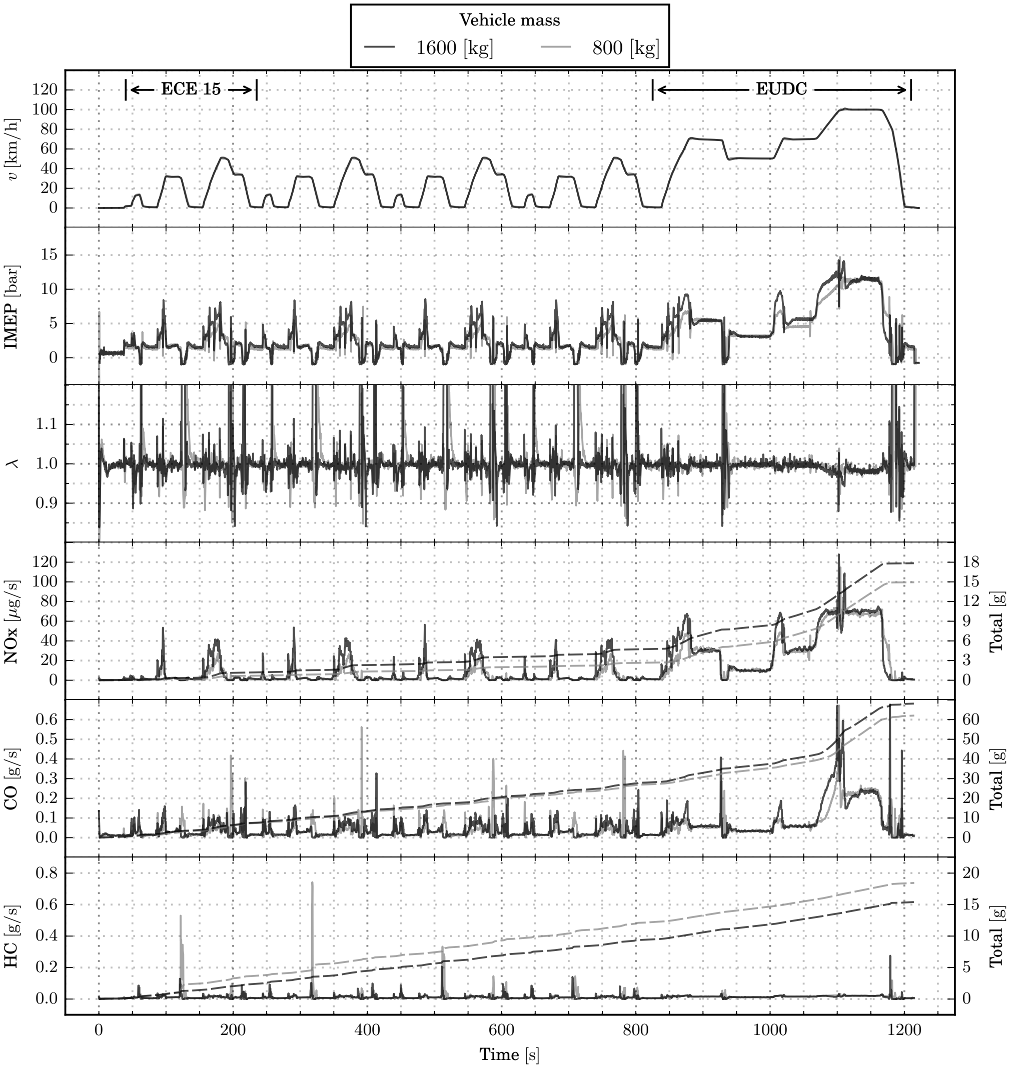

Figure 7.1: *Comparison of the NEDC results with for vehicle mass value of* 1600 kg *and* 800 kg*. The NOx, soot and temperature were measured before the three way catalyst. v is the vehicle speed, λ is air to fuel ratio relative to the stoichiometric ratio and* HC *is CH_4 equivalent hydrocarbon mass flow. All emissions were sampled between the turbocharger turbine and the catalyst (pre-catalyst)*

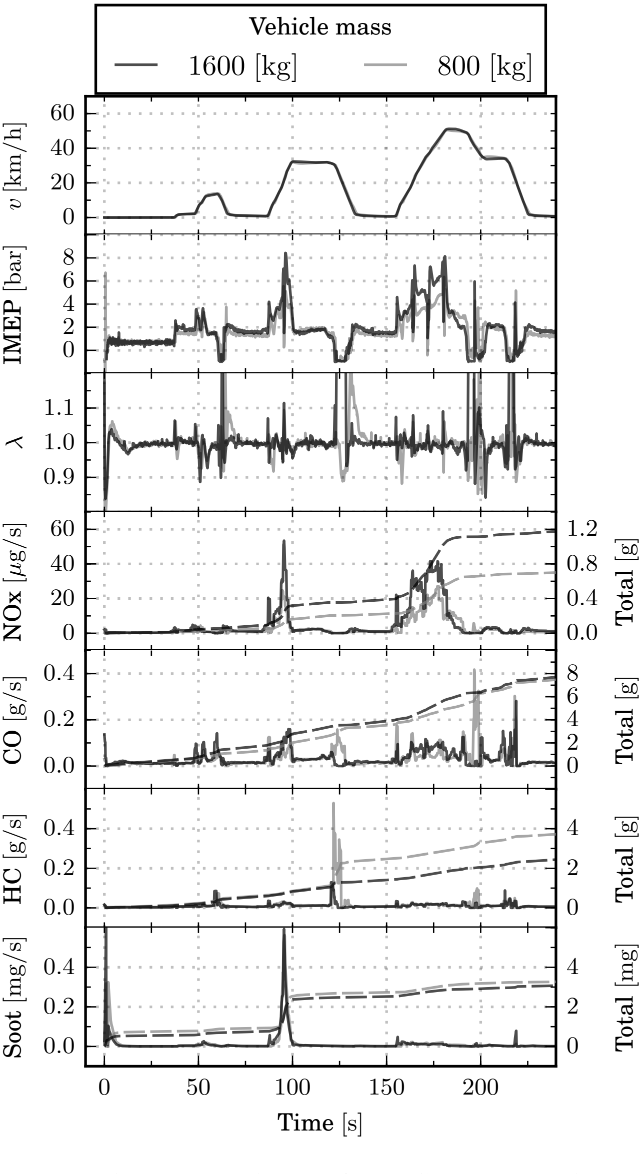

Figure 7.2: *Comparison of the results for the first ECE 15 cycle of the NEDC for vehicle mass value of* 1600 kg *and* 800 kg*. The NOx, soot and temperature were measured before the three way catalyst. v is the vehicle speed, λ is the air to fuel ratio relative to the stoichiometric ratio and HC is the CH_4 equivalent hydrocarbon mass flow. All emissions were sampled between the turbocharger turbine and the catalyst (pre-catalyst)*

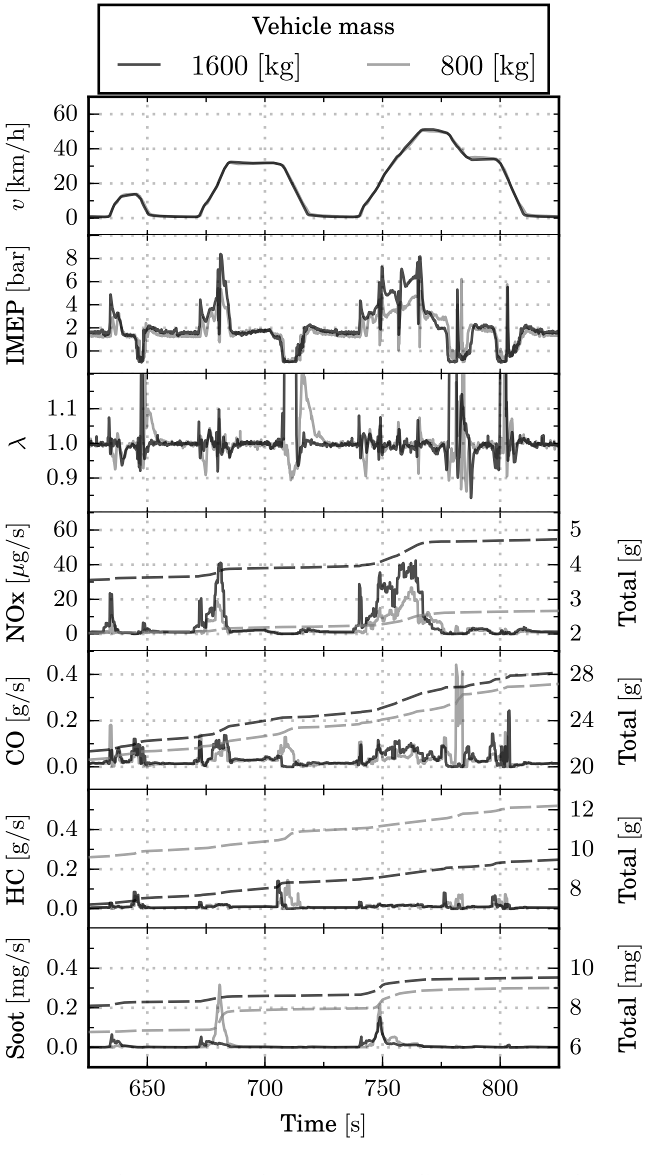

Figure 7.3: *Comparison of the results for the last ECE 15 cycle of the NEDC for vehicle mass value of* 1600 kg *and* 800 kg*. The NOx, soot and temperature were measured before the three way catalyst. v is the vehicle speed, λ is the air to fuel ratio relative to the stoichiometric ratio and HC is the CH_4 equivalent hydrocarbon mass flow. All emissions were sampled between the turbocharger turbine and the catalyst (pre-catalyst)*

1600 kg	Fuel	0.710 kg 0.0890 L km^{-1}
	CO$_2$	83 g km^{-1} 0.82 kg/kg
	CO	0.23 g km^{-1} 6.0 g kg^{-1}
	NOx	0.63 g km^{-1} 5.1 g kg^{-1}
	HC	0.41 g km^{-1} 1.7 g kg^{-1}
	PM	0.31 mg km^{-1} 0.1 mg kg^{-1}
	PN	0.8×10^{14} km^{-1} 0.21×10^{16} kg^{-1}
800 kg	Fuel	0.656 kg 0.0824 L km^{-1}
	CO$_2$	69 g km^{-1} 0.82 kg/kg
	CO	0.65 g km^{-1} 4.6 g kg^{-1}
	NOx	0.36 g km^{-1} 2.8 g kg^{-1}
	HC	0.68 g km^{-1} 8.1 g kg^{-1}
	PM	0.43 mg km^{-1} 4.0 mg kg^{-1}
	PN	0.9×10^{15} km^{-1} 0.12×10^{16} kg^{-1}

Table 7.1: NEDC precatalyst fuel consumption and emissions per kilometer and per kilogram of fuel for 1600 kg and 800 kg vehicle mass

7.1.3 Particulate Matter

Particulate matter emissions in terms of both number and mass occurred predominantly during acceleration in both tests, similarly to the previously discussed emission results as shown in Figure 7.4. The particulate mass (PM) emissions in particular occurred during accelerations in the ECE 15 segments of the drive cycle in both tests which coincided with transient fuel rich conditions as shown in Figure 7.1 and in greater detail Figure 7.2 and Figure 7.3. In both tests the particulate mass spikes at acceleration accounted for the total emissions prior to the EUDC segment with very little increase in total PM emission during constant engine load or deceleration. During the EUDC segment the fuel rich conditions at the end of the segment also accounted for a fraction of the PM emissions due to continuously fuel rich conditions in addition to acceleration λ transients. Engine start resulted in soot emissions during which fuel rich conditions also occurred due to excessive engine throttling as previously discussed. The difference in the instantaneous PM emission between the pure gasoline operation and simulated electric motor assist tests was minimal suggesting that engine load reduction during accelerations had little effect on the PM emissions. Since the λ transients were similar in both tests, it would seem that this was the determining factor for PM emissions. The total PM emissions per kilometer were approximately equal as shown in Table 7.1, with the electric motor assist test resulting in slightly larger PM value. Due to the lower fuel consumption for the simulated electric motor assist test, the total PM emission per unit mass of fuel was larger in the simulated electric assist test. The majority of the total PM emissions occurred during the ECE 15 segments as shown in Figure 7.4.

The particulate number (PN) was calculated based on the number and size distribution for particle larger than 23 nm. The PN emissions in both tests also occurred primarily during accelerations during the ECE 15 segments and coincided with the PM emissions as shown in Figure 7.4. In both tests PN emission spikes occurred at the beginning of deceleration. In addition to PN emissions during accelerations in the ECE 15 segments, PN emission spikes were also measured at the beginning of deceleration in both tests. As discussed previously, fuel rich λ transients coincided with both accelerations and deceleration with the latter also associated with gear shifts. This is consistent with laboratory and on road measurements of PN emissions from commercial light duty vehicles [Kar+14]. A significant difference in PN emissions between pure gasoline operation and simulated electric motor assist was observed. The latter case resulted in significantly greater PN emission during accelerations. The simulated electric assist test demonstrated continuous PN emissions during deceleration and during the second segment of the first ECE 15 segment of the drive cycle.

Due to the fuel rich λ transients coinciding with PM and PN emissions, the particulate matter is attributed to soot as fuel rich conditions are known to result in soot formation [Sta01]. The greater PN emissions in the electric motor assist case is hypothesized to in part be due to less efficient in cylinder oxidation of the soot due to lower combustion temperature [Sta01] as a result of lower engine load. The total PN emissions in the simulated electric motor assist test are nevertheless still accounted for by emissions during accelerations. The PN emissions during the EUDC segment are equal for both tests and occur during the fuel rich final constant speed segment where the engine load and λ in

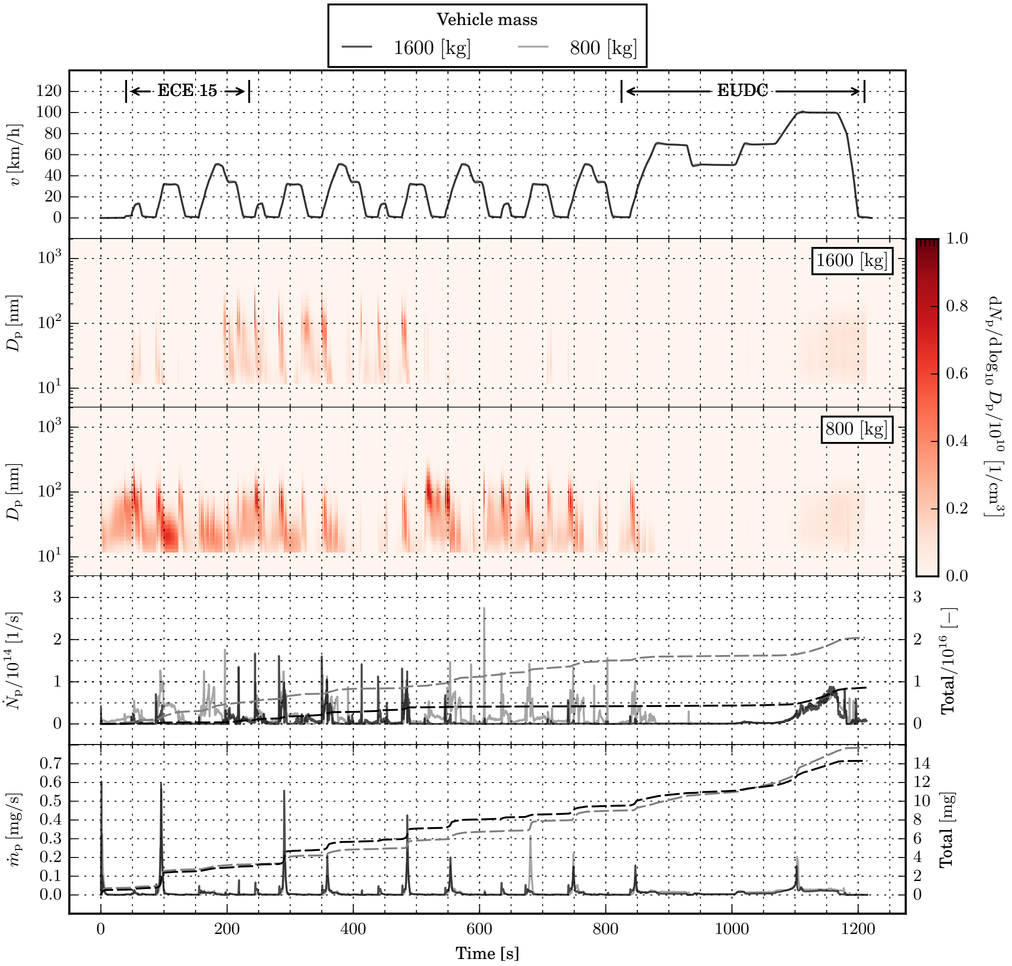

Figure 7.4: *Comparison of the soot particle size distribution and number for vehicle mass values of* 1600 kg *and* 800 kg*.* D_p *is the particle diameter,* $\dot{N}_\mathrm{p}$ *is the particle number flow rate and* $\dot{m}_\mathrm{p}$ *is the particle mass flow rate. All emissions were sampled between the turbocharger turbine and the catalyst (pre-catalyst)*

both tests were also equal. This would seem to lend further weight to the hypothesis of soot oxidation dependence on engine load for equal λ values. Improvements in fuel metering and throttle control and reducing the second derivative of the engine load by electric powertrain assistance are methods which could be investigated as means to reduce or eliminate the fuel to air ratio transients.

The relative size distribution of particulate matter was similar in the pure gasoline operation and simulated electric motor assist tests as shown in the second and third plot respectively in Figure 7.4. The particle size distribution during accelerations in both tests were centered around 100 nm. Similar results were obtained by [Kar+14]. While the particle size distributions during acceleration in the simulated electric motor assist test was similar to the pure gasoline operation size distributions, the magnitude of the distribution was greater, consistent with the greater PN emissions. This illustrates that the particulate matter in both tests originated in the same manner. Similarly to the PM emissions the majority of the total PN emissions occurred during the ECE 15 segments.

7.2 Soot Formation in E10 and E85 Stratified Combustion

7.2.1 Cylinder Pressure Analysis

Two injection strategies were investigated for the 3.6 bar engine load and and three for 5 bar for both E10 and E85. Single and double injections were used for both loads with an additional four injection strategy for the 5 bar engine load. Four injections was not used for the 3.6 bar engine load because it did not allow sufficient time for the injector orifice to open fully due. This meant that the injected mass was difficult to control precisely in this case. The injection strategy cases are listed in Table 7.2 along with the injection durations and timings, spark timing and combustion variable results from cylinder pressure analysis. The injection strategies and spark timings are also illustrated schematically in Figure 7.5 in which the trigger signals are shown.

In a given case with multiple injections, the durations of the individual injections were equal as was the delay between each injection if four injections were used. The injection durations in each case were determined from this and the requirement that the total fuel quantity was to be equal to that of corresponding single injection case with the same engine load. The individual injection durations in the multiple injection cases are longer than that obtained by dividing the single injection duration with the number of injections in the given case. This is due to the additional opening and closing of the injection orifice in the multiple injection cases during which the injector orifice area and be extension the fuel flow rate is smaller than when fully open. The additional time allotted for each injection compensates for this effect.

With the exception of case C, stable ignition and combustion for both fuels was achieved when the spark occurred at the end of the last injection, as illustrated in Figure 7.5 with the injection and spark signals. In all cases the IMEP coefficient of variation (CoV) was below 6 %. For case C in which a single injection was used for the larger 5 bar engine load, reliable ignition and combustion was not possible with a spark at the end of

Fuel	Case	n_{inj}	SOI	t_{inj}	d_{inj}	SOS	$\overline{\mathrm{IMEP}}$	$\Delta\overline{\mathrm{IMEP}}$	IMEP CoV	ΔIMEP CoV	$\overline{\mathrm{CA50}}$	$\overline{\mathrm{CA50}}-$ SOS	Avg. $\frac{\mathrm{d}Q_{\mathrm{ch}}}{\mathrm{d}t}$	Max. $\frac{\mathrm{d}Q_{\mathrm{ch}}}{\mathrm{d}t}$	Q_{ch}
			CAD	μs	μs	CAD	bar	%	%	%	CAD	CAD	$\mathrm{kJ\,s^{-1}}$	$\mathrm{kJ\,s^{-1}}$	J
E10	A	1	-20	420		-16	3.64	(a)	4.0	(a)	2.9	18.9	39.6	238	343
	B	2	-25	230	400	-16	3.75	$3.0_{(\mathrm{a})}$	2.9	$-28_{(\mathrm{a})}$	3.0	19.0	40.0	202	354
	C	1	-32	550		-20	4.88	(b)	4.6	(b)	4.1	24.1	49.5	186	457
	D	2	-28	300	400	-17	5.07	$3.9_{(\mathrm{b})}$	2.4	$-48_{(\mathrm{b})}$	2.2	19.2	52.2	281	473
	E	4	-32	192	200	-21	5.34	$9.4_{(\mathrm{b})}$	2.8	$-39_{(\mathrm{b})}$	1.7	22.7	53.4	276	503
E85	A	1	-20	560		-16	3.73	(c)	3.9	(c)	2.6	18.6	40.8	256	354
	B	2	-24	300	400	-14	3.98	$6.7_{(\mathrm{c})}$	2.4	$-38_{(\mathrm{c})}$	3.2	17.2	43.0	242	380
	C	1	-35	760		-20	4.97	(d)	5.3	(d)	1.9	21.9	48.1	193	459
	D	2	-30	400	400	-17	5.15	$3.6_{(\mathrm{d})}$	2.6	$-51_{(\mathrm{d})}$	3.0	20.0	53.9	265	495
	E	4	-30	220	200	-16	5.25	$5.6_{(\mathrm{d})}$	2.3	$-57_{(\mathrm{d})}$	1.1	17.1	52.6	321	482

Table 7.2: Case injection parameter values, the measured work and combustion variable results for the experiments. The combustion variable results were determined from cylinder pressure measurements during imaging. The change in mean IMEP and IMEP CoV for multiple injection experiments relative to the single injection experiment are denoted $\Delta\overline{\mathrm{IMEP}}$ % and ΔIMEP CoV % respectively. The $\Delta\overline{\mathrm{IMEP}}$ and ΔIMEP CoV value subscripts denote the label of the single injection experiment to which the value is relative to. n_{inj}: number of injections, SOI: start of injection, t_{inj}: individual injection duration, d_{inj}: delay between injections, SOS: start of spark, $\overline{\mathrm{IMEP}}$: mean IMEP, CoV: coefficient of variation, $\overline{\mathrm{CA50}}$: mean CA50., $\mathrm{d}Q_{\mathrm{ch}}/\mathrm{d}t$: rate of heat release (Eq. 6.1), Q_{ch}: total heat release. The average rate of heat release was determined on the interval $[\mathrm{SOS}, \mathrm{SOS} + 80]$.

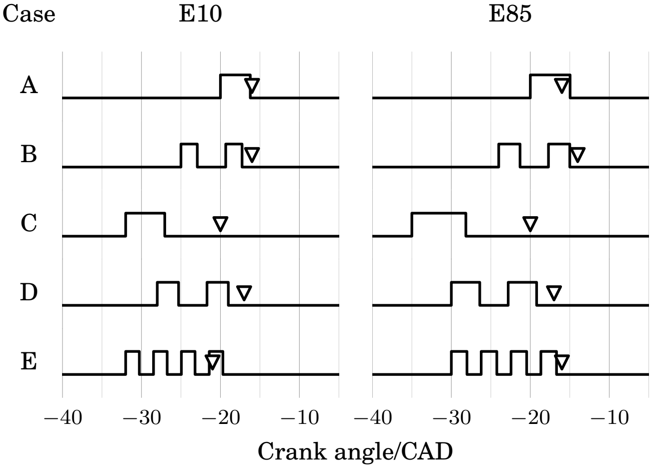

Figure 7.5: *The injection and ignition coil trigger signals and durations for the experiments in Table 7.2. A high signal indicates an injection trigger signal. The triangles indicate the timing of the ignition coil trigger signal*

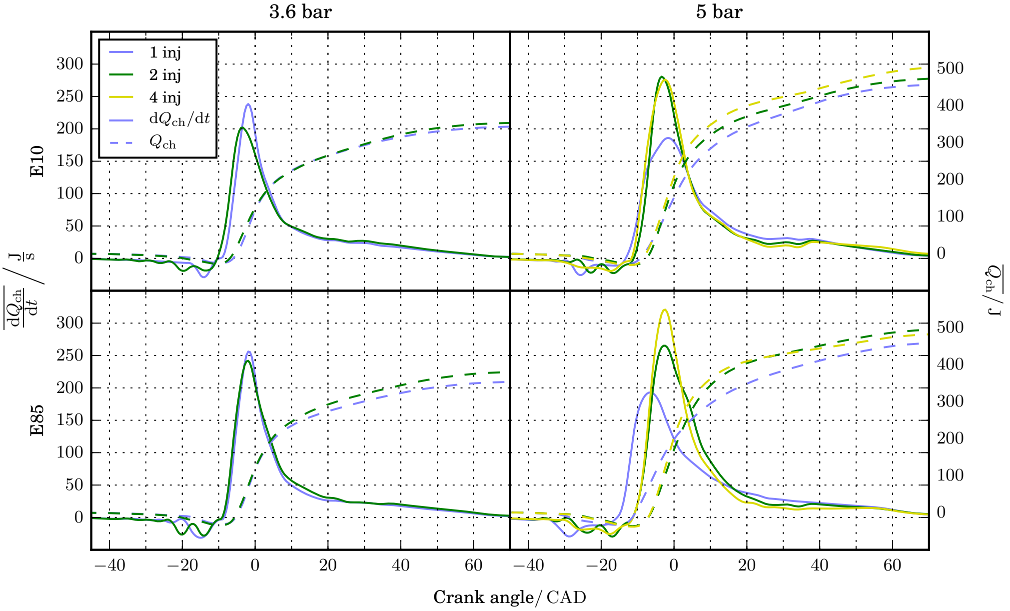

Figure 7.6: *Cycle ensemble average rate of heat release and cumulative heat release for the cases in Table 7.2*

injection in contrast to the shorter duration single injection for the 3.6 bar engine load in case A. Instead, a spark 7 CAD to 8 CAD after the end of injection yielded stable ignition and combustion. It is assumed that the disparity is due to excessively fuel rich conditions on average in the stratified mixture, at and immediately after the end of injection in case C which causes the initial flame to propagate poorly. Delaying the spark relative to the end of injection allows further mixing of the fuel with the ambient gas. Due to the smaller fuel mass in case A it is further assumed that the mixing that occurs during injection and immediately after is sufficient to produce a suitable average fuel to air ratio in the stratified mixture.

The start of injection and the spark timings for the single injection cases resulted in the maximum IMEP. The maximum IMEP coincided with CA50 values of 1 CAD to 4 CAD after TDC firing (aTDC) for both E10 and E85. This is earlier than the CA50 value of 7 CAD aTDC often cited for maximum IMEP in homogeneous combustion [Hey89]. The same CA50 range for maximum IMEP and minimum variability as been observed for E0, E20 and E85 with the same injector type in an earlier study [Fra11]. This result suggests that the rate of combustion curve for stratified combustion differs from that of homogeneous combustion; either the rate of fuel oxidation during the initial stage of combustion is larger compared to homogeneous combustion or the rate of oxidation during the latter stage is smaller. By contrast, if the rate of combustion for stratified combustion was scaled so as to be slower or faster throughout compared to homogeneous combustion, the optimal CA50 would remain at 7 CAD because the ratio of fuel oxidation occurring during compression and expansion would remain the same.

Multiple injections led to an increase in IMEP of between 3 % to 9 % and a decrease in IMEP variation between 30 % to 60 % for both engine loads and for both fuels relative to the corresponding single injection cases. Increasing the number of injections from two in case D to four in case E for the 5 bar load led to led to a further increase in IMEP for both E10 and E85 while the IMEP CoV increased slightly for E10 and decreased slightly for E85 consistent with the respective total heat release. The increase in total heat release suggests an increase in combustion efficiency. This is consistent with either poor combustion of the fuel on the piston in the single injection case and with improved mixing and combustion in the gas phase. Whether one or a combination of both effects is responsible cannot be concluded on the basis of the cylinder pressure analysis.

The duration of the first half of combustion was larger for E85 compared to E10 in all cases as indicated by the shorter time between the spark and CA50, given in Table 7.2 as $\overline{\text{CA50}} - \text{SOS}$. The peak rate of heat release for E85 was also larger for every case compared to E10 except when using two injections for the 5 bar load in case D as shown in Figure 7.6. The larger peak rate of heat release for E85 compared to E10 is consistent with previous results demonstrating that the peak rate of heat release and duration of combustion in the same type of engine operation increases with the fuel ethanol fraction [OBM10].

The peak rate of heat release for both fuels decreased by 20 % as the load increased from 3.6 bar to 5 bar when a single injections was used and the average rate of heat release similarly decreased, as shown in Figure 7.6 and in Table 7.2. Increasing the number of injections at the 5 bar load from one in case C to two in case D resulted in an increase in the peak and average rate of heat release for both E10 and E85. For E85, increasing the number of injections to four caused a reduction in IMEP, total heat release and average heat release relative to two injections although all were larger than in the single injection case.

In contrast to the 5 bar engine load, multiple injections did not have a significant effect on the rate of combustion at the 3.6 bar engine load with E10 despite the increase in IMEP and total heat release, and decrease in IMEP CoV. The increase in IMEP corresponds with the increase in total heat release. The rate of heat release and the average value was approximately equal although the peak value decreased by 15 %. For E85, two injections again led to a decrease in the first half combustion duration and an increase in the average rate of heat release with a slightly smaller peak value.

7.2.2 Imaging

A comparison of the E85 fuel sprays from a single injection and double injection is shown in Figure 7.7 in the left and right columns respectively with cycle average cylinder liner images. The time from the start of the first injection trigger signal to the end of the last injection trigger signal was 560 μs and 1000 μs respectively and the time from the start of the first injection trigger signal, denoted Δt_{SOI}, is given in each image. The end of the last trigger signal for both of the experiments occurred at the same crank angle as shown in Figure 7.5. At $\Delta t_{\mathrm{SOI}} = 287\,\mu$s the penetration length of both fuel sprays was approximately equal despite a slightly higher ambient density in the single injection case as injection began 4 CAD later. At $\Delta t_{\mathrm{SOI}} = 478\,\mu$s both fuel sprays impinge on the piston surface. The injection trigger signal had ended in the double injection experiment and fuel injection ceased resulting in a shorter duration of impingement compared to the single injection experiment in which fuel injection continued. In the single injection experiment the piston was closer to the injector at the same time after the start of injection due to the later start of injection crank angle. [MPK10] found that the penetration length of the hollow cone fuel spray from an outward opening piezo injector increased linearly during injection and the penetration rate decrease significantly at the end of injection in pressure chamber measurements at 0.5 MPa and 1.0 MPa. Based on the shorter duration of fuel spray impingement on the piston crown and the reduction of the penetration length at the cessation of injection it is conjectured that a smaller fuel mass impinged on the piston crown at $\Delta t_{\mathrm{SOI}} = 478\,\mu$s in the double injection experiment where injection had ceased compared to the single injection experiment where injection continued.

At $\Delta t_{\mathrm{SOI}} = 978\,\mu$s the time from the start of the second fuel injection trigger pulse was 278 μs and the injection had lasted equally as long as the first injection at $\Delta t_{\mathrm{SOI}} = 278\,\mu$s. At $\Delta t_{\mathrm{SOI}} = 978\,\mu$s the fuel spray penetration length was smaller and the spray was wider compared to the first fuel spray at $\Delta t_{\mathrm{SOI}} = 278\,\mu$s. [MPK10] found that the penetration length and maximum width of the hollow cone fuel spray decreased with increasing pressure. During motored conditions the single injection caused the pressure to decrease by 1 bar from 19 bar due to vaporization of the fuel. The decrease in pressure after the first injection is not thought to be sufficient to explain the increase in fuel spray width at $\Delta t_{\mathrm{SOI}} = 978\,\mu$s and the decrease in penetration length at a lower cylinder pressure is inconsistent with the pressure chamber results. An increase in the angle of the second hollow cone fuel spray using two fuel injections in an optical engine with an outward opening piezo injector was measured by [Sti+13]. A stable upward flow towards the injector in the interior of the first hollow cone fuel spray due a vortice on the inside of the leading edge of the hollow cone was identified from particle image velocimetry (PIV) measurements and was referred to as a funnel flow [Sti+13]. A correlation between the funnel flow velocity and the spray angle was found and it was concluded that the flow impinged on the second fuel spray causing the increase in spray angle. The results presented here are consistent with the PIV results in the earlier study. In the double injection experiment a greater fraction of fuel was injected during partial needle lift and a reduced injector orifice area due to the additional opening and closing of the injector caused by the additional fuel injection. Two injections of fuel results in a lower effective injector orifice area compared to a single fuel injection with the effective area decreasing with an increasing number of injections. [Mar+10] found that a lower needle lift reduced the hollow cone fuel spray penetration length for both homogeneous and stratified injection timings in an optical engine. A lower effective needle lift and injector orifice area is expected to result in a reduced fuel spray penetration length and a decrease in the piston crown fuel film mass based on these results.

Pool fires on the piston due to spray impingement occurred for both E10 and E85 when using a single injection for both engine loads. This is shown in Figure 7.8 in which the single and cycle ensemble averaged images at 40 CAD aTDC for each case in Table 7.2 are shown. Pool fires are characterized by flames emanating from the piston. The single images clearly show pool fires on the piston for the single injection cases for both fuels. The radiation is composed of chemiluminescence and soot incandescence due to the formation of soot in the diffusion flames. Soot incandescence is the primary contributor to the pool fire radiation. While the single images more clearly illustrate the source of radiation, the cycle ensemble average images are more suitable for comparison of the injection strategies for each fuel. The luminosity at the piston surface in the average images for the single injection cases demonstrate the regular occurrence of pool fires.

Pool fires were the only source of radiation emission for E85 at both loads and with all injection strategies as shown by the single and average images. No significant incandescence separate from the pool fires occurred in the cylinder volume. The size of the pool fire increased with the engine load with a single injection. Increasing the number of injection from one to two reduced the pool fire incandescence significantly at both the 3.6 bar and 5 bar load and increasing to four injections at the 5 bar engine load reduced the pool fire still further to the point that the average luminosity of the pool fire is smaller than for the 3.6 bar single injection.

In contrast to E85, pool fires were not the only source of luminosity with E10. In the single injection case at 3.6 bar engine load single image, luminous flames are located above the pool fires in the cylinder volume. The maximum intensity in the average images is located at middle of the surface of the piston and lower average intensity values are found evenly distributed throughout the cylinder volume above in contrast to the corresponding E85 case. Taken in conjunction with the single image this suggests that for E10, soot formation occurred in the gas phase late in the combustion process based on the rate of heat release in Figure 7.6.

Two injections at 3.6 bar with E10 led to an overall reduction of luminosity similarly to E85. A confined region of luminous flame on the left hand side of the cylinder volume

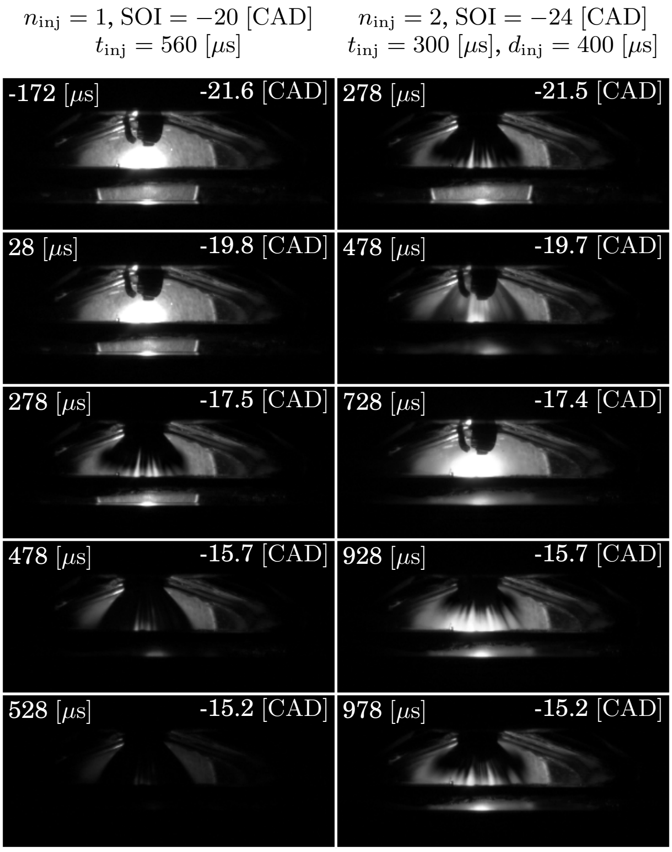

Figure 7.7: *Comparison of the E85 fuel injection process and the fuel sprays for a single injection and two injections with the same total fuel mass. Cycle average of cylinder liner images of fuel injection for the single injection experiment in the left column and a double injection experiment in the right column, case A and B respectively.* $\omega = 1500\,\mathrm{RPM}$. *The time relative to SOI is given in the upper left corner of each image and the crank angle is given in the upper right corner*

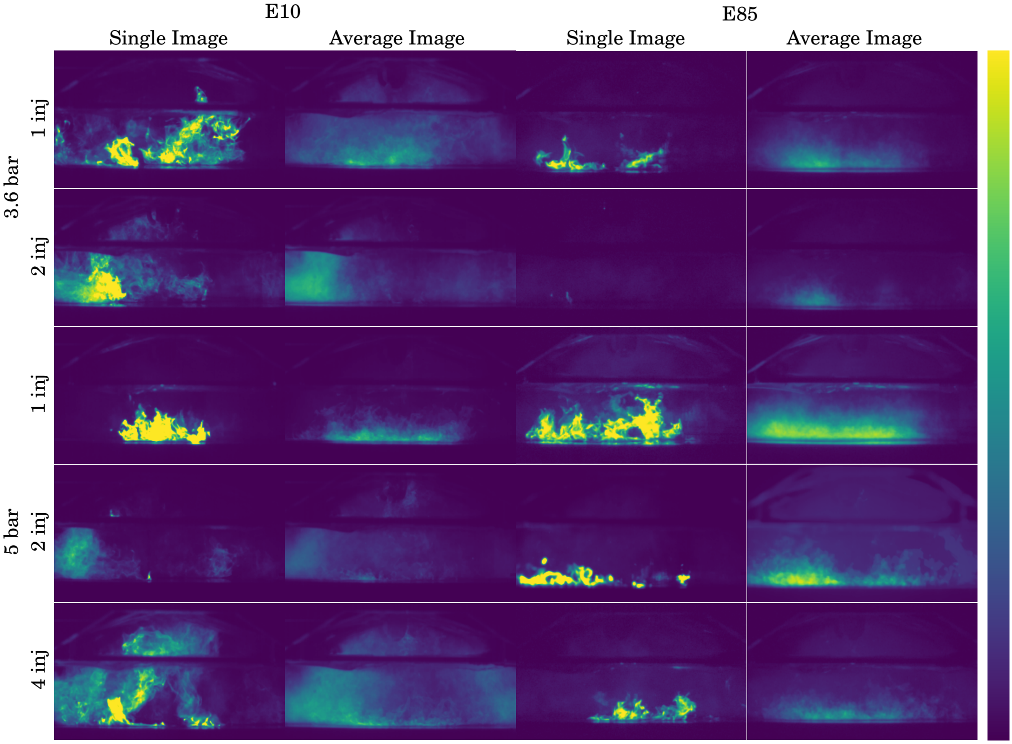

Figure 7.8: *Comparison of single and cycle ensemble average cylinder liner images for E10 and E85 at* 40 CAD *aTDC. A gamma correction of 4 has been applied to enhance low intensity features. Different exposures and apertures were used respectively for the E10 and E85 images*

exists in both the single and average images with almost no luminosity in the rest of the cylinder volume compared to the single injection case. The average image of the luminous flame is not confined to the surface of the piston as pool fires in the other cases are suggesting that it is not a pool fire. Pool fires thus appear to have been reduced with an accompanying increase in soot formation in the gas phase.

At the 5 bar load, as in the 3.6 bar load case, a single injection resulted in a pool fire at the middle of the piston. Unlike the 3.6 bar case and similarly to the corresponding case E85 at 5 bar, there was no luminosity above the pool fire in the rest of the cylinder volume. While the luminosity differed from the 3.6 bar engine load, two injections effectively eliminated the pool fire and the radiation emissions with two injections are strikingly similar to the 3.6 bar load with the same number of injections. Radiation emissions were confined primarily to the left of the cylinder volume above the piston rather than on the surface. Increasing the number of injections shifted the soot formation from a pool fire to the gas phase with less luminosity.

Increasing the number of injection to four with E10 at 5 bar caused an increase in luminosity rather than a further reduction as was the case with E85. Pool fires which were absent with two injections appeared again with four injections as evident both from the single image and luminosity on the piston surface in the average image. The luminosity in the rest of the cylinder volume above the piston similarly increased relative to the two injection case rather than decreasing.

7.2.3 Spectrum

Images of the E85 combustion luminescence (A) and combustion luminescence spectrum (B) passing through the piston crown synchronously recorded at −14.0 CAD, 0.0 CAD and 20.0 CAD in a cycle are shown in Figure 7.9. The spectrometer arrangement gathered luminescence from the combustion chamber volume delimited in the horizontal plane normal to the cylinder axis (a plane parallel to the piston crown surface) at the top of the combustion chamber by the white rectangle in the combustion luminescence images. The measurement volume approximately spanned the combustion diameter in the vertical direction and was centered horizontally on the spark plug. The measurement volume was spatially resolved in the vertical direction of the delimitation rectangle in the combustion luminescence images and correspondingly along the vertical axis in the combustion luminescence spectra images (B).

Luminescence from the spark discharge at the centre of the rectangle delimiting the measurement boundaries in the plane was observed at −14.0 CAD, as shown in the luminescence image in (A). The spatially centered (vertical axis centre) broad spectrum in the luminescence spectrum image in (B) corresponds to the spark luminescence. Peaks in the spatial sum of the luminescence spectrum (C) correspond to energy transitions of species present at the spark plug. Given that the fuel spray was ignited as it passed the spark plug during the spark plug discharge, the species present are in part the result of the combustion of fuel. Species with energy transitions corresponding to the wavelengths of the spectrum peaks in (C) have been labeled in the figure.

OH and CH possess energy transitions in the vicinity of 312 nm at which a spectrum peak is present [Gay74]. The spectrum peak at 312 nm is attributed primarily to the

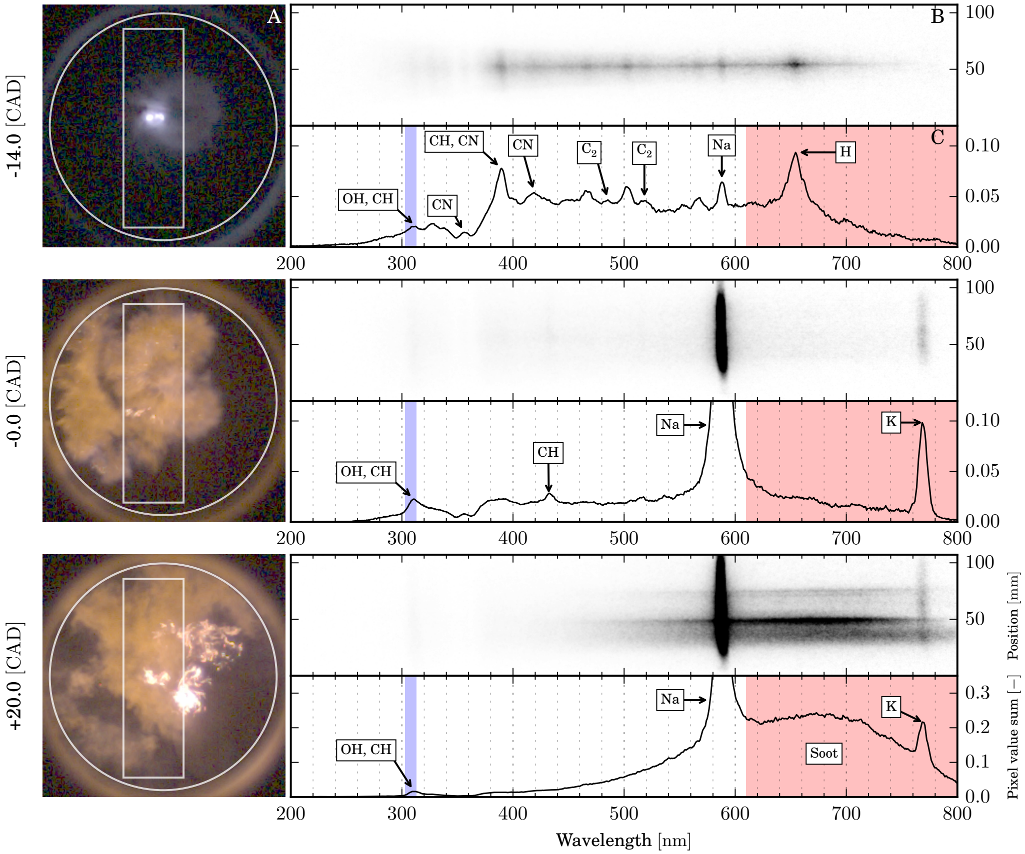

Figure 7.9: *Images and spectra of luminescence passing through the piston crown recorded at* -14.0 CAD, 0.0 CAD *and* 20.0 CAD *for cycle number 45 of 50 fired cycles for the E85 case A (*3.6 bar, *one injection,* SOI $= -20$ CAD *and* SOS $= -16$ CAD*). (A) Luminescence image. The white circle marks the location of the piston crown window edge. The white rectangle delimits the spectrometer measurement volume in the plane normal to the cylinder axis (the piston crown plane). The vertical axis of the measurement volume delimitation was spatially resolved in the luminescence spectrum. An exponential intensity transfrom with an exponent value of* 0.25 *has been applied to make the flame and low intensity details more easily visible. (B) The luminescence spectrum from the measured volume. The spectrum of the emitted luminescence is resolved along the horizontal axis of the image and the vertical location in the measurement volume delimitation rectangle in (A) is resolved along the vertical axis. The position values are relative to the bottom edge of the delimiting rectangle. (C) Plot of the spatial sum of the emission spectrum image ((B) image column sums). The labels indicate species with energy state transitions corresponding to the wavelengths indicated by the label arrows. The blue and red shaded wavelength intervals (left and right respectively) were captured in the* OH^* *chemiluminescence and soot incandescence images respectively discussed in subsection 7.2.4 using the experiment apparatus arrangement discussed in subsection 6.2.4*

presence of OH with contributions from CH and possibly other unidentified species and is referred to as OH* chemiluminescence. Both OH and CH are radical species involved in the combustion reaction mechanism models for the combustion of hydrocarbon fuels in general and ethanol in particular [GY08; Lep+11]. The presence of either is taken to indicate the occurrence of radical chemistry and conditions conducive to the oxidation of soot as discussed in subsection 5.2.5.

The blue shaded region indicates the spectrum interval gathered in the OH* chemiluminescence imaging and spans a wavelength interval of 10 nm at FWHM centered at 308 nm. This wavelength interval covers the spectrum peak attributed to OH* chemiluminescence with the peak located at the far end of the interval as shown in Figure 7.9. The OH* chemiluminescence spectrum peak was also present at 0.0 CAD during the peak rate of heat release and at 20.0 CAD at which point two pool fires are visible in the luminescence image. The continued presence of OH* chemiluminescence throughout the combustion process is consistent with the presence of OH radicals in the coincident line of sight and visible flame fronts in the measurement volume apparent in the visible luminescence images (A) with OH radicals participating in ongoing combustion radical chemistry according to the discussed reaction mechanism models. The OH* chemiluminescence intensity was centered and spread across the demarcated measurement area at 0.0 and 20.0 CAD coinciding with the visible flame area. This suggests flame front chemistry was distributed across the visible flame area. That OH* chemiluminescence is easily identified and not obscured by spectrally broadband emission at 0.0 CAD and 20.0 CAD, demonstrates the applicability of luminescence at this wavelength for detection of rapid radical chemistry associated with flame fronts and conditions favourable for the oxidation of soot.

The large peak at 390 nm is attributed primarily to CH and CN in addition to the probable luminescence contributions from other species. Both CN and C_2 radicals are similarly attributed to several peaks as shown in Figure 7.9 and are also involved in hydrocarbon combustion reaction mechanism models. In contrast to OH* chemiluminescence, the luminescence spectrum peaks to which CN and C_2 are attributed are not easily identifiable at 0.0 CAD and 20.0 CAD in part due to broadband emission from soot amongst other sources as discussed in the following.

H is thought to be one possible source for part of luminescence peak at 654 nm. The luminescence peak was present during the spark discharge and was not subsequently apparent at later stages of the cycle. The spectrum peak at 588 nm is attributed to Na. The intensity of the spatial luminescence sum increased from −14.0 CAD to 20.0 CAD as combustion progressed and the flame front expanded. During the same period a spectrum peak at 768 nm attributed to K appeared and the intensity of this luminescence spectrum peak increased in the same manner as the peak associated with Na. Luminescence from both attributed sources spanned the vertical length of the visible flame area in the measurement boundaries at 0.0 CAD and 20.0 CAD. Na luminescence thus accounts for the orange colour of the visible flame area. The source of Na and K is believed to be the fuel and the refining process of the fuel.

The bright luminescent flames approximately in the center of the chamber at 20.0 CAD emanated from pools fires as discussed in the preceding Section 7.2.2. Three areas of luminescence from pool fires occurred within the measurement volume. The pool fire luminescence in the center of the measurement boundary area gave rise to the broad saturated spectrum line (horizontal line) centered spatially (vertically) in the spectrum image. The pool fires above and below the central pool fire with approximately equal intense luminosity give rise to the less intense broad spectra above and below the saturated broad spectrum line in (C) due to their location on the right edge of the measurement volume. The broad spectrum lines in the luminescence spectrum image (B) results in a broad spectrum peak in the spatial sum of the luminescence spectrum (C). The spectral distribution of the broad spectrum peak is similar in nature to the distribution of the spectrum from blackbody radiation when the superimposed peaks from Na and K are disregarded. Based on this, the source of the broad spectrum peak is conjectured to be thermal radiation from particulate matter which in turn is conjectured to be soot particles. The spectral distribution is consistent with typical emission spectra from soot [Mod13, Ch. 12]. The red shaded area in luminescence spectrum spatial sum plots (C) indicates the spectral region transmitted by the lowpass filter used for the soot incandescence imaging. The spectral sum of the soot incandescence transmitted by the filter is significantly greater than than the sum of the transmitted luminescence at 14.0 CAD and 0.0 CAD from sources of luminescence other than broad spectrum soot incandescence at 20.0 CAD. It is for this reason that significant luminosity in the spectral interval gathered by the soot incandescence imaging is attributed primarily to soot with additional contributions from other sources of luminescence.

7.2.4 OH^* Chemiluminescence and Soot Incandescence

The spatial probability of OH^* chemiluminescence and soot luminescence, calculated as the cycle ensemble mean of the threshold images at a given crank angle, is shown in Figure 7.10. The crank angle of each image is relative to the start of the spark. All image processing was done with the Python package scikit-image [Wal+14]. Thresholding was applied in order to separate chemiluminescence and incandescence from noise from the image intensifier and reflections from the cylinder head. Li's minimum cross entropy method [LL93; LT98] was used to determine threshold values for the OH^* chemiluminescence and soot incandescence images respectively from the 3.6 bar engine load, single injection case. This choice establishes the case as the benchmark for comparison with the other load and injection strategy cases for each fuel. Separate threshold value pairs were determined for E10 and E85 due to the different exposures used for each fuel. The values for cases with the same fuel can therefore be compared while only trends can be compared for cases with different fuels. The threshold values for the OH^* and soot images are each the cycle ensemble mean of the threshold values calculated using Li's minimum cross entropy method from the set of images 15 CAD after the start of the spark at which point a flame had developed. This choice of images provides both a background and a flame resulting in OH^* chemiluminescence and soot incandescence from which the threshold is determined.

The sum of the OH^* chemiluminescence or soot incandescence pixel values in the respective image types provides a spatial average of the relative combustion and soot formation activity between cases respectively as discussed earlier. The intensity of an image, denoted i, is defined as the normalized sum of the set $\mathcal{R}$ of pixel values above the

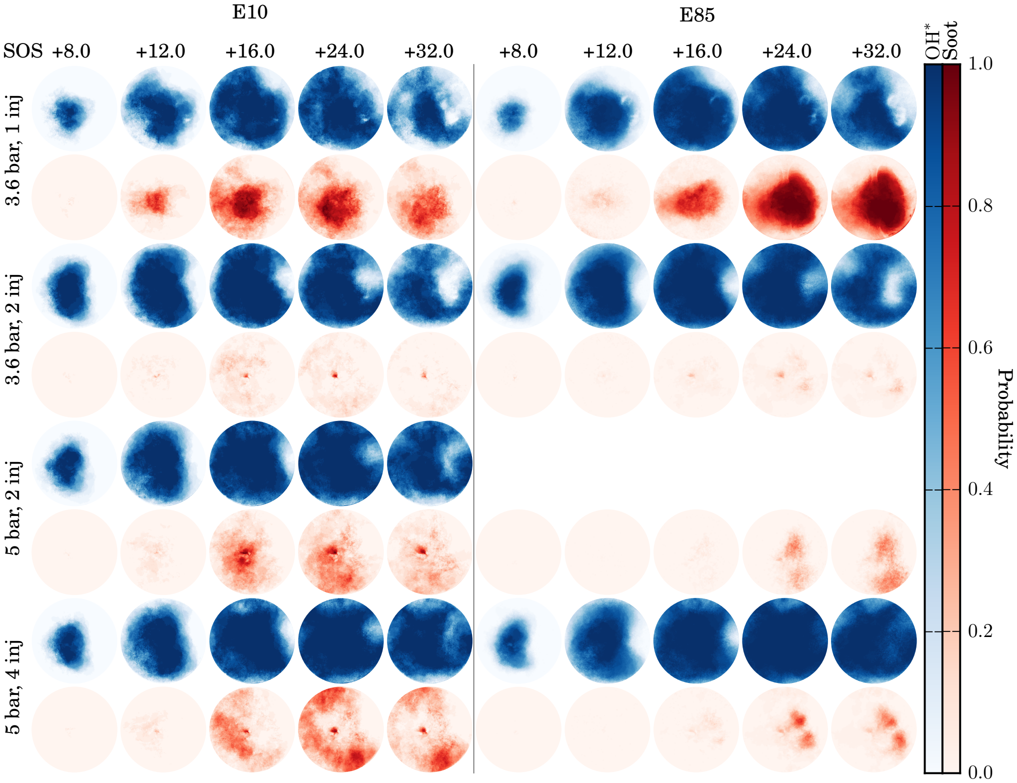

Figure 7.10: *Spatial probability of* OH* *chemiluminescence and soot incandescence at crank angles relative to the start of the spark. The probabilities are determined from the sum of cycle images at each crank angle after thresholding using Li's minimum cross entropy method. The OH* and soot threshold values for each fuel are the mean of the values calculated from the* 3.6 bar, *1 inj. case at* SOS+15 CAD *for E10 and E85 respectively. As a result, the E10 and E85 threshold value pairs are different and based on case A for each fuel. The* 5 bar, *2 inj. OH* data set for E85 is unavailable due to a camera calibration error*

threshold value and given in Eq. 7.1.

$$i\left(\mathcal{R}\right) = \frac{1}{C_n} \sum_{(u,v)\in\mathcal{R}} I\left(u,v\right) \tag{7.1}$$

where u and v are the horizontal and vertical pixel coordinates of a pixel in the set $\mathcal{R}$, $I\left(u,v\right)$ is the value of the pixel at the given coordinate and C_n is a normalizing constant. The normalizing constant pair for OH* and soot is different for E10 and E85 in the same manner as the threshold pairs. The values are based on the maximum values amongst all cases for a given fuel.

If multiple injections lead to improved fuel and air mixing compared to a single injection, combustion would be expected to occur over a greater volume of the cylinder. If this is the case, a similar trend is expected for OH* chemiluminescence since it is an indication of ongoing combustion. An increase in OH* chemiluminescence volume can be detected as an increase in projected area due to the line of sight nature of the image. The sum of second order centralized image moments [BB09] of the threshold image scaled with the cylinder area is used as a measure of the spatial distribution of OH* chemiluminescence and soot luminescence. This is referred to as the spread, denoted s, and is given in Eq. 7.2.

$$s\left(\mathcal{R}\right) = \frac{1}{A_{\text{cyl}}^3} \sum_{(u,v)\in\mathcal{R}} \left(u-\overline{u}\right)^2 + \left(v-\overline{v}\right)^2 \tag{7.2}$$

where $\overline{u}$ and $\overline{v}$ are the centroid coordinates of $\mathcal{R}$ and A_{cyl} is the cylinder area in number of pixels. The power of 3 arises due to the order of the moments [BB09]. The spread is proportional to the area of $\mathcal{R}$ and the distance of each pixel in $\mathcal{R}$ to the centroid of $\mathcal{R}$. Two pixel sets with the same area will not in general yield the same spread value.

3.6 bar

The spatial probability of OH* chemiluminescence for both E10 and E85 at the 3.6 bar demonstrate a similar progression after ignition. The chemiluminescence is initially circular with large frequency and expands to the left away from the injector and downward towards the exhaust valves as combustion progresses. The orientation of the images is the same as in Figure 6.4. The edges of the inflamed volume show the greatest variation as indicated by the low probability vales. For both fuels an area in the upper right of the cylinder is completely devoid of OH* chemiluminescence throughout the combustion process. This area is clear at +16 CAD and +24 CAD in both the E10 and E85 images and has been observed earlier in flame images [JH15b]. At +32 CAD the area of high probability has decreased and consists of a roughly circular area in the center of the combustion chamber as the combustion process ends per the rate of heat release in Figure 7.6. The two approximately circular voids at +32 CAD in the E85 3.6 bar, 1 inj. OH* chemiluminescence image are due to soot on the piston from pool fires which block OH* chemiluminescence based on observed soot patterns on the piston crown during routine cylinder liner and piston crown cleaning.

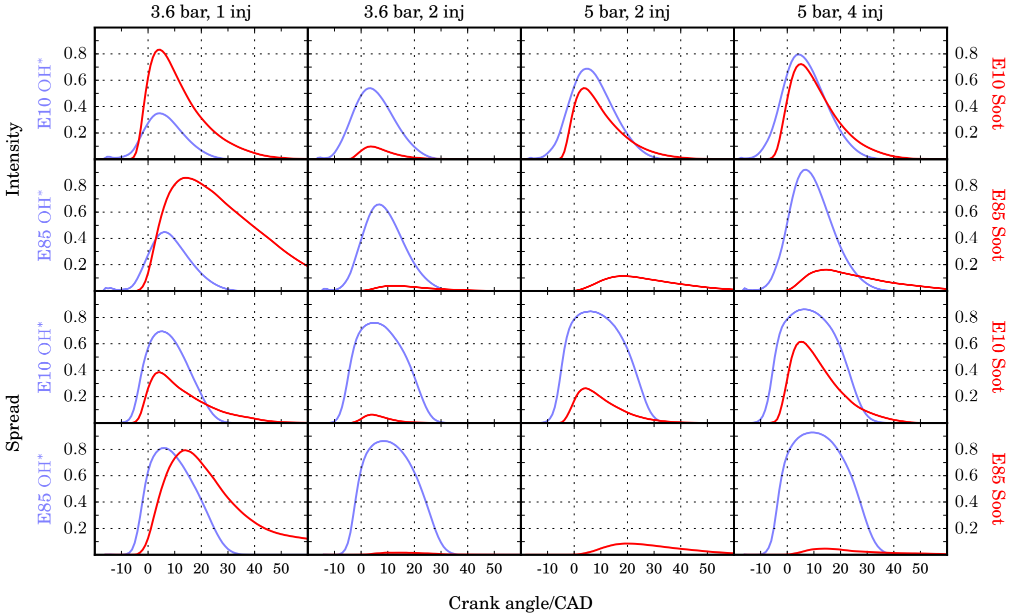

Figure 7.11: *Cycle ensemble average of the* OH* *chemiluminescence and soot incandescence intensity and spread. The intensity is the sum of pixel values above the threshold value and represents the spatial average. Distinct normalization and threshold value pairs are used for E10 and E85 respectively. The normalization and threshold values are equal for a given fuel and data set; for example, the E10 OH* chemiluminescence threshold values for each case are equal and the same normalization value is used for all intensity data for these same cases. The intensity and spread are defined by Eq. 7.1 and 7.2 respectively. The* 5 bar, *2 inj. OH* data set for E85 is unavailable due to a camera calibration error*

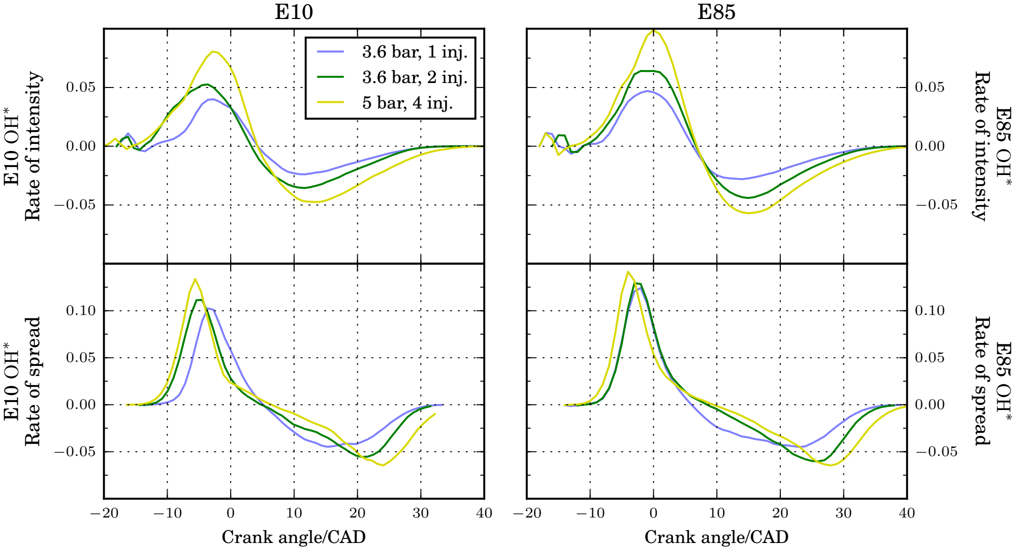

Figure 7.12: *Cycle ensemble average of the* OH* *chemiluminescence rate of intensity and rate of spread defined as the second order finite difference of i and s respectively as a function of the crank angle. The rate of intensity and spread for the* 3.6 bar*, 1 injection and 2 injection case and the* 5 bar*, 4 injection case shown in Figure 7.11*

Whereas the spatial probability OH* chemiluminescence for both E10 and E85 with a single injection at 3.6 bar are similar, the distribution and development of soot incandescence differs which is consistent with the images in Figure 7.8 for this case. The onset of soot incandescence for E10 occurred earlier compared to E85 and occurred with less frequency over a smaller area throughout the combustion process. By the end of the combustion process at +32 CAD the probability of soot incandescence had decreased compared to the peak values earlier at +16 CAD. The peak soot incandescence intensity coincided with the peak OH* chemiluminescence and both decreased exponentially subsequently as shown in Figure 7.11. In contrast, for E85 the soot incandescence probability and extent continued to increase from the onset to +32 CAD at which point soot incandescence occurred over a large extent in every cycle. The pool fire soot incandescence intensity reached a peak value after the OH* chemiluminescence for E85 and decreased in a linear manner rather than exponentially as was the case for E10. The location of soot incandescence also differs with the soot incandescence for E10 located to the left of the incandescence in the E85 case.

When the results for E85 are compared with the corresponding single and average images in Figure 7.8 it is clear that the soot incandescence coincided with the pool fires in these images and that the pool fires are the source of the frequent soot incandescence. The presence and extent of OH* chemiluminescence overlapped the soot incandescence from the onset until the extent of the OH* chemiluminescence decreased which is visible at +32 CAD. At this point significant overlap still existed between OH* and soot. The overlap suggests that during the early stages of the pool fire, as it increased in size, conditions in the vicinity of the pool fire were conducive to the oxidation of the the resulting soot. The pool fire continued to be a source of soot formation as the extent and probability of OH* chemiluminescence decreased presumably along with soot oxidizing conditions. The linear rather than exponential decrease in soot incandescence intensity demonstrates both the persistence of pool fires and the importance in soot formation given the slower decrease compared to oxidizing conditions.

The source of soot incandescence for E10 at 3.6 bar and one injection was a mix of pool fires and soot formation in other parts of the combustion chamber volume based on the average image in Figure 7.8 for the case. Further illustration of the difference in soot formation source is provided by the exponential decrease of soot incandescence in conjunction with the OH* chemiluminescence in contrast to E85. The exponential decrease in soot incandescence taken in conjunction with the greater proportion of soot formation occurring the gas phase compared to the E85 suggests that gas phase soot formation is short lived and is oxidized efficiently by the overlapping soot oxidizing regions throughout the combustion process in contrast to the pool fires in the E85 case.

Increasing the number of injections from one to two lead to a remarkably similar OH* chemiluminescence spatial distribution for E10 and E85 in addition to an increase in OH* chemiluminescence intensity and the rate of increase in the intensity, as shown in Figure 7.12, along with a decrease in soot incandescence intensity. The spread and the rate of spread of OH* chemiluminescence increased relative to the single injection cases for both fuels throughout the combustion process which is apparent from a comparison of the images in Figure 7.10 from +8 CAD to +32 CAD and from a comparison of the OH* spread graphs for the two cases for each fuel in Figure 7.11 and in Figure 7.12. The increase in the OH* chemiluminescence rate of spread indicates a faster flame propagation and is hypothesized to be due to improved fuel and air mixing compared to the single injection case while avoiding over mixing and excessively fuel lean conditions. The increase in intensity and spread for E10 contrasts with the negligible change in the average rate of heat release. The increase in intensity and spread coincides with an increase in IMEP and reduction in IMEP CoV for both E10 and E85.

For both fuels the OH* chemiluminescence recurrently expanded to the left and vertically before continuing around the perimeter to the right of the combustion chamber volume. The void on the right was not due to soot on the piston and given the absence of soot incandescence in the same region the void cannot have been caused by attenuation by soot particles. Based on the similarity in the OH* distribution is presumed to be the result of a recurrent fuel distribution when two injections were used despite the difference in fuel mass and fuel properties. In contrast, the chemiluminescence distribution in the single injection case differs to a greater degree between the two fuels. The first of two injections from outward opening pintle injectors has been observed to create a recurrent bulk flow pattern which affects the second injection demonstrating repeatable phenomena associated with double injections [Sti+13].

The soot incandescence intensity and spread for both fuels underwent a significant reduction with two injections and so was entirely absent in the majority of cycles relative to the threshold values based on the single injection case for each fuel. The soot incandescence distribution for both fuels is similar primarily due to the large reduction in the incandescence. The most frequent location of soot incandescence was the spark plug based on cylinder liner images, possibly due to a jet flame as the result of spray impingement.

The soot incandescence sources for each fuel when using two injections mirrored the sources when one injection was used. The E85 soot incandescence stemmed from two infrequent pool fires and for E10 it originated from the gas phase based on the visible luminosity in Figure 7.8. The soot incandescence for both fuels was overlapped by recurrent OH* chemiluminescence providing soot oxidizing conditions in the vicinity. The reduction in pool fires for E85 is attributed to reduced fuel spray impingement on the piston [JH15b]. The reduction for E10 is consistent with the hypothesis of improved fuel and air mixing leading to a reduction of fuel rich regions given the dependence of soot formation on fuel rich conditions [Sta01].

The difference in the relative contribution of soot incandescence from pool fires suggests that the fuel properties and quantity significantly affected the piston impingement. The start of injection for corresponding cases for E10 and E85 were essentially identical and the end of injection was broadly similar. Despite the difference in the soot incandescence sources, the use of multiple injections decreases the soot formation for both fuels regardless.

5 bar

Two injections at the 5 bar engine load for both E10 and E85 led to less soot incandescence intensity and spread than for the corresponding single injection cases at the 3.6 bar load despite the increase in fuel quantity which more likely lends itself to an increase in fuel rich regions. Both quantities were larger than for the same injection cases at the 3.6 bar engine load as might be expected. For both fuels the soot incandescence distribution was similar to the corresponding cases at the 3.6 bar load albeit with larger probabilities. Soot incandescence was once again frequent solely at the spark plug for E10 with the remaining less frequent soot incandescence located in the gas phase based on a comparison of the soot incandescence images in Figure 7.10 with the average image in Figure 7.8 for the case. For E85 the more frequent soot incandescence from the two pool fires was in the same location and the spread was larger.

With two injections the OH* chemiluminescence distribution for E10 was remarkably similar to the 3.6 bar two injection case despite the increase in fuel quantity. The chemiluminescence developed in the same manner and the same voids were present although with a reduction in size. Of particular note are the voids on the right of the combustion chamber for both the 3.6 bar and 5 bar cases. The intensity and spread increased compared to the 3.6 bar case as expected due to the increase in fuel mass and resulting combustion activity. The similarity of the chemiluminescence distribution for the E10 3.6 bar and 5 bar load cases with two injections is consistent with the hypothesis that the double injection creates a recurrent fuel distribution despite the increase in fuel mass.

The E10 OH* chemiluminescence distribution remained remarkably similar after increasing the number of injections to four and was similar to the E85 OH* distribution. The intensity and spread increased further for E10 compared to the two injection case with an accompanying decrease in the void areas which all remained in the same locations at the same stages in the combustion process. Similarly to E10, the E85 OH* distribution was similar to the 3.6 bar case with two injections and the reduction in void area occurred.

The E85 soot incandescence when four injections were used was very similar to the two injection case with the same two pool fires as the source. The spread decreased slightly due to the reduction in the extent of the pool fires. The increase in frequency and intensity of the pool fires are hypothesized to be due to the later end of injection. The end of the third injection coincides with the end of the second injection in the two injection case as illustrated in Figure 7.5. The fourth injection thus occurs after the end of the fuel injection process in the two injection case which is hypothesized to lead to increased fuel impingement.

In contrast to the similarity of the E85 soot incandescence distribution and source for the two and four injection cases, the E10 soot incandescence distribution changed significantly with the increase in the number of injections. The soot incandescence frequency, intensity and spread increased and a greater proportion of the soot stemmed from pool fires compared to the two injection case in which pool fires were largely absent. This difference is even more remarkable due to the near identical distribution of OH* chemiluminescence for the two E10 cases. While the increase in spread and intensity of the OH* chemiluminescence with the increase in injections suggests improved fuel and air mixing, the increase soot incandescence suggests an increase in the average fuel to air ratio in the stratified mixture and increased fuel impingement.

7.3 Gas Jet Structure

Figure 7.13 shows the average of the 50 schlieren images after background subtraction and taking the absolute value where $p_{\mathrm{amb}} = 0.4\,\mathrm{MPa}$, $p_{\mathrm{inj}} = 2.2\,\mathrm{MPa}$, $t = 1.5\,\mathrm{ms}$. From the image it is apparent that the Turner model of a transient jet is in good agreement with the current case insofar as the overall shape of the jet is concerned. This becomes even more clear when a threshold is applied to the image in Figure 7.13 yielding the image in Figure 7.14. From the images in Figure 7.13 and Figure 7.14 it can be seen that the leading edge of the jet is circular while the behind this leading edge the jet is triangular which is consistent with the Turner model.

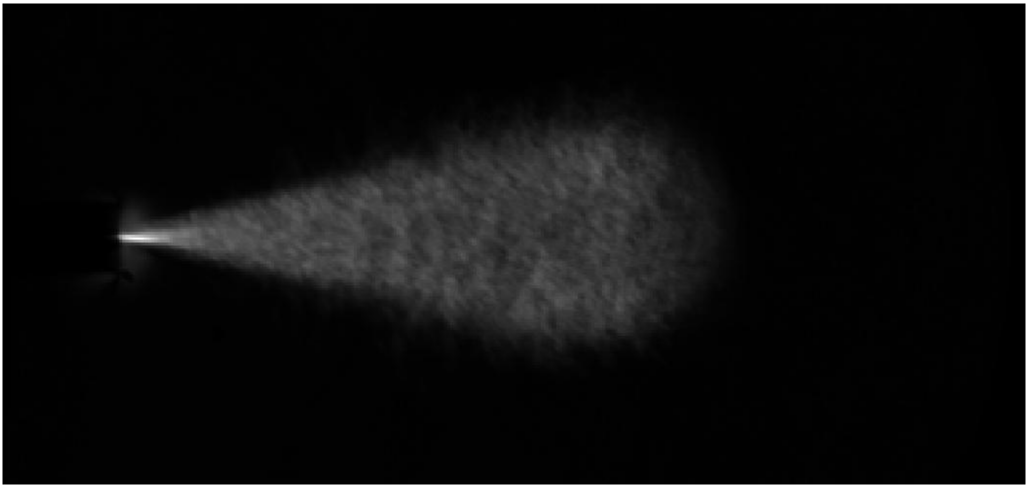

Figure 7.13: *The average of 50 images schlieren images after background subtraction and taking the absolute value.* $p_{\mathrm{amb}} = 0.4\,\mathrm{MPa}$, $p_{\mathrm{inj}} = 2.2\,\mathrm{MPa}$, $t = 1.5\,\mathrm{ms}$

According to the Turner model, the location of the maximum jet width[1], z_D, is located a half jet width behind the leading edge. Therefore, according to the Turner model, $z_D + D/\,2$ should be equal to z_t if the Turner model is accurate for the jets created in this study. Figure 7.15 is a comparison of these two quantities. The penetration length calculated from the jet width and the location of the maximum jet width is initially equal to z_t and diverges during the first $3\,\mathrm{ms}$ as the penetration length is smaller than the actual leading to a rapid increase to $8.5\,\%$ in the error of the Turner model relative to z_t. The penetration length estimate provided by $z_D + D/\,2$ exhibits the same power law relation as z_t with respect to t as stated in Eq. 4.1. After the initial increase in relative error of the Turner model, the relative error remained approximately constant. The penetration length provided by the Turner model would therefore appear to be a reasonable approximation of the true penetration length. The constant relative error and smaller penetration length would either indicate that the almost circular leading arc of the jet, shown in Figure 7.14, deviates slightly from a perfectly circular arc, or that

---

[1] This is also the center of the head vortex in Figure 4.1.

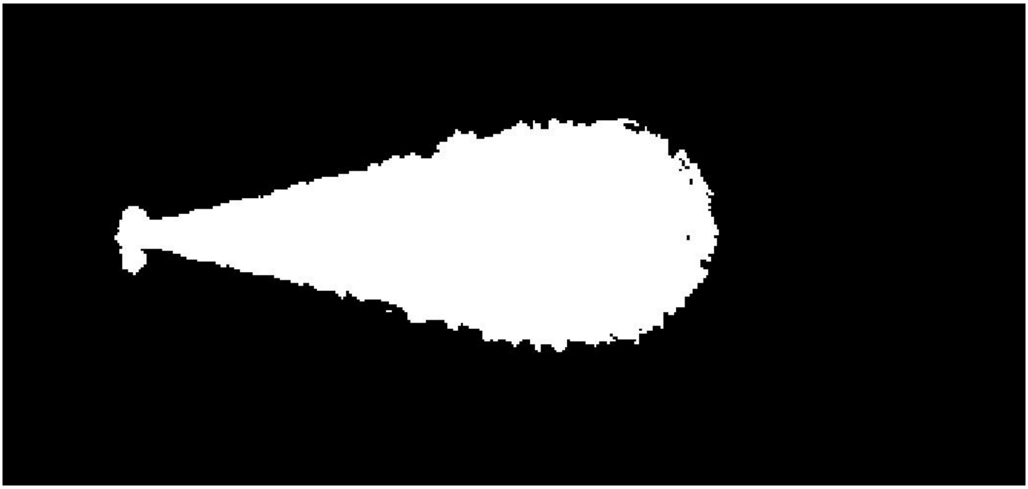

Figure 7.14: *The threshold image resulting from the image in Figure 7.13*

$z_D < z_t - D/2$; the maximum jet width occurs further away from leading edge than predicted. Given the small relative error (< 0.1), and the jet images in Figure 7.13 and Figure 7.14, it can be concluded that the Turner model is an accurate model of the average overall structure of the jet for the given case in Figure 7.15. For the remaining cases investigated, the penetration length estimate also under predicted the true penetration length with an approximately constant relative error of the order of 10 %, indicating that the Turner model was appropriate for the other 17 combinations of p_{inj} and p_{amb} investigated.

In accordance with the discussion by [HO99] and results of [Riz58; BKD10], the jet in all cases was found to be self similar with respect to D/z_t for $z_t/d_{\text{noz}} > 20$ given the near constant value D/z_t. The onset of self similarity appeared to be delayed as the the injection pressure or the ambient pressure increased. [HO99] argued that non-dimensional lengths scale with $\sqrt{\rho_{\text{noz}}/\rho_{\text{amb}}}$ which is consistent with D/z_t scaling with p_{inj} while it is inconsistent with D/z_t scaling with p_{amb}. The mean of $\overline{D}/\overline{z}_t$ for $z_t/d_{\text{noz}} > 60$ was used to determine the self-similarity value. In comparison with the value of 0.25(5) reported by [HO99] as measured from the data of [Riz58], the values are significantly larger, ranging from 0.33 to 0.422, relative to the value of 3.0 reported by [Riz58]. The minimum value of 0.330 occurred with $p_{\text{inj}} = 3.6\,\text{MPa}$, $p_{\text{amb}} = 0.1\,\text{MPa}$ yielding the maximum $p_{\text{inj}}/p_{\text{amb}}$ of all the pressure combinations investigated. Conversely, the maximum value of 0.422 occurred with the third smallest pressure ratio 1.86 investigated where $p_{\text{inj}} = 1.3\,\text{MPa}$, $p_{\text{amb}} = 0.7\,\text{MPa}$. The two cases with a lower pressure ratio also provided large values for the mean $\overline{D}/\overline{z}_t$ relative to the other cases. The value of the self-similarity value D/z_t therefore appears to be inversely proportional to the pressure ratio $p_{\text{inj}}/p_{\text{amb}}$ as illustrated in Figure 7.16. The value of appears to asymptotically approach a value of 0.33 as $p_{\text{inj}}/p_{\text{amb}}$ increases.

The data by [Riz58] is for water jets in water and the smaller ratio of the injected helium density to the chamber air density therefore appears to have played a role in the

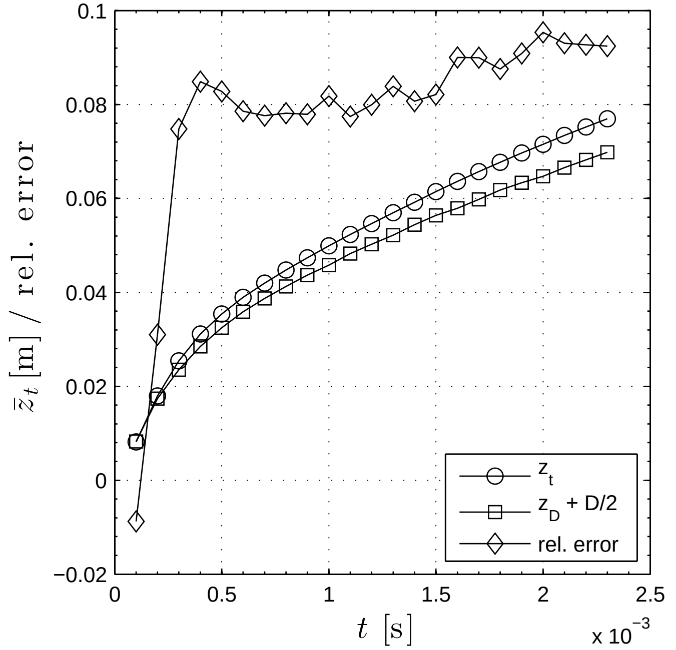

Figure 7.15: $\overline{z}_t$, *$\overline{z}_D + \overline{D}/\,2$ and relative error of $\overline{z}_D + \overline{D}/\,2$ relative to z_t with* $p_{\mathrm{amb}} = 0.4\,\mathrm{MPa}$*,* $p_{\mathrm{inj}} = 2.2\,\mathrm{MPa}$

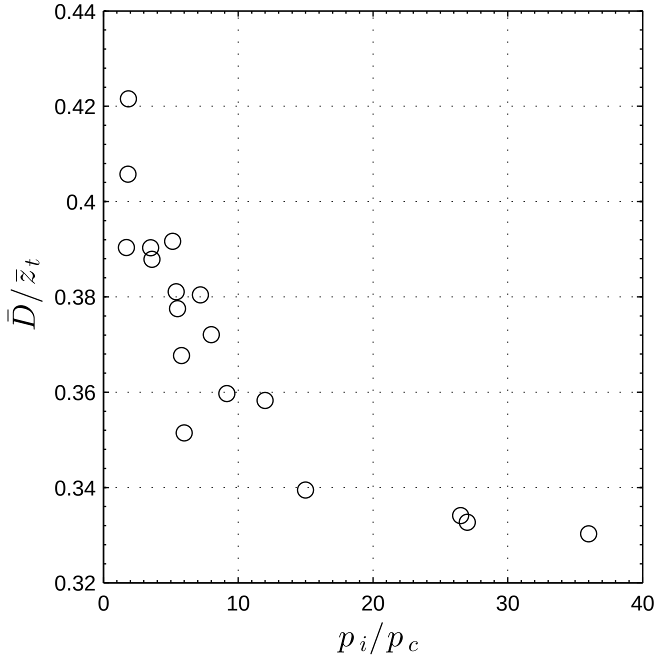

Figure 7.16: *Mean of* $\overline{D}/\overline{z_t}$ *for* $z_t/d_{\mathrm{noz}} > 60$ *as a function of* $p_{\mathrm{inj}}/p_{\mathrm{amb}}$

larger values of z_t/D obtained in this study and that z_t/D is inversely proportional to $p_{\mathrm{inj}}/p_{\mathrm{amb}}$. The spread in z_t/D values at near equal pressure ratios also shows that the pressure ratio is not the only parameter influencing the structure of the jet.

Chapter 8

Conclusion

The potential for reduction of spark ignition engine emissions during engine load transients using assistance from the electric powertrain was investigated. This was done using dynamometers imposing a road load determined from a predefined vehicle mass and speed profile on a three cylinder, turbocharged, spark ignited, direct injected engine. A modified New European Drive Cycle was used for the vehicle speed profile. Electric assistance during vehicle accelerations and the resulting engine load transients was simulated by reducing the road load on the engine during speed transients. NOx emissions during engine load transients were reduced with simulated electric powertrain assistance due to the reduction in combustion temperature due to a reduction in engine load. CO, hydrocarbon and soot emissions occurred at the beginning and end of engine load transients due to transient fuel rich conditions in the engine as a result of incorrect fuel metering. Electric assistance as simulated in the study did not reduce these emissions because the fuel rich, fuel to air ratio transients occurred at the beginning or end of engine load changes rather and were unconnected to the engine load value during the transient. Improvements in fuel metering and throttle control and reducing the second derivative of the engine load by electric powertrain assistance are methods which could be investigated as means to reduce or eliminate the fuel to air ratio transients.

Direct injection of fuel into the cylinders in spark ignition engines provide several advantages over port fuel injection engines with respect to improving fuel efficiency and transient response when continuing to operate the engine with homogeneous combustion. Direct injection in spark ignition engines also provides the means to operate the engine with lean stratified combustion which increases the maximum possible air to fuel ratio, thereby extending the lean operating limit and thermal efficiency. Lean stratified combustion leads to increased soot formation due to locally rich combustion and greater combustion instability due to locally fuel lean conditions. Ethanol is a low carbon intensity, alternative fuel for spark ignition engines which can be produced from renewable sources and possesses several advantageous properties compared to gasoline. Previous studies found that soot emissions from lean, spark ignited, stratified combustion of pure ethanol and blends of ethanol with small quantities of gasoline were reduced compared to gasoline. Combustion, sources of soot formation and soot oxidation in lean, spark ignited, stratified combustion of E10 (10 % vol. ethanol, 90 % vol. gasoline) and E85 were investigated in an engine with optical access using pressure analysis, high speed imaging, OH* chemiluminescence and soot incandescence. Two engine loads were studied. The effect of splitting a single injection into multiple injections on the phenomena studied was also investigated. Diffusion combustion of liquid fuel films on the surface of the piston, referred to as a pool fire, was a major source of soot formation for both E10 and E85 when a single injection was used. Fuel was injected during the end of the compression stroke in order to provide a stratified and ignitable fuel and air mixture by avoiding over mixing of the fuel and air. This caused the fuel spray from a single injection to impinge on the piston creating a liquid fuel film on the piston due to the proximity of the piston to the injector. The effect was magnified when the engine load was increased. For E10, in addition to the soot formation from pool fires, soot formation also occurred in the gas phase. Pool fires were the sole source of soot formation with E85 as the fuel. Splitting the single injection into multiple injections reduced the magnitude of soot formation from pool fires for both E10 and E85 which is hypothesized to be due to a reduction in fuel impingement on the piston and the liquid fuel film mass. While the pool fires were reduced for E10, soot formation in the gas phase, seemed to increase slightly with multiple injection for both engine loads. Multiple injections led to an increase in the rate and stability of combustion in all cases. These results along with an increase in the spread of OH* chemiluminescence in the combustion chamber is hypothesized to be due to increased fuel and air mixing in the gas phase while avoiding over mixing and excessively fuel lean conditions locally. Further investigation of the interaction between the combustion process and the fuel and air mixture formation process, both in terms of the liquid fuel spray and the vapour phase would provide a greater understanding of the phenomena which was studied in the current work, particularly with respect to stratified operation using piezo actuated, outward opening pintle injectors as was used in this work.

Gaseous fuels such as hydrogen and methane amongst others are another class of alternative fuels for spark ignited engines. Both are available from renewable sources and are low carbon-intensity fuels. Direct injection of gaseous fuels in spark ignited engines increases specific power. Lean, spark ignited, stratified combustion of gaseous fuels depends on reliable ignition of the fuel which can be achieved during injection. This requires an understanding of the transient behaviour of gas jets during fuel injection. The transient structure of gas jets during injection with a range of injection and ambient pressures was investigated. Self similarity and the Turner model for the structure of transient jets were investigated under the varying pressure conditions. High speed schlieren imaging of helium jets in a constant flow, pressure chamber filled with air and with optical access was used in the study. The jets were found to be self similar with respect to the ratio of the maximum jet width to the jet penetration length after having penetrated 20 nozzle diameters for all injection pressures and ambient pressures investigated. The Turner model was found to be an accurate approximation for the structure of the jet for all pressure in all cases. The self similarity variable was found to vary with the injection pressure to ambient pressure ratio indicating that the jet width to length ratio varied with different pressure ratio. This has implications for the ignition location for gaseous fuel jets during injection in lean stratified combustion operation, in which pressure conditions also vary, particularly the cylinder pressure which corresponds to the ambient pressure in the investigation.

Chapter 9

Contributions

Paper A

- L. C. R. Johansen and S. Hemdal. In cylinder visualization of stratified combustion of E85 and main sources of soot formation. *Fuel* **159** (2015), 392–411. DOI: `10.1016/j.fuel.2015.07.013`

S. Hemdal defined the scope of the work and supervised the project. S. Hemdal and L. C. R. Johansen performed the experimental work in conjunction with Research Engineer E. de Benito Sienes. L. C. R. Johansen wrote the manuscript and S. Hemdal edited the manuscript.

Paper B

- L. C. R. Johansen, S. Hemdal, and I. Denbratt. Comparison of E10 and E85 Spark Ignited Stratified Combustion and Soot Formation. *Submitted to Fuel* (2016)

S. Hemdal defined the scope of the work. I. Denbratt and S. Hemdal supervised the project. S. Hemdal and L. C. R. Johansen performed the experimental work in conjunction with Research Engineer E. de Benito Sienes. L. C. R. Johansen wrote the manuscript and S. Hemdal and I. Denbratt edited the manuscript.

Paper C

- L. C. Johansen, I. Denbratt, and S. Hemdal. Drive Cycle Particulate and Gaseous Emissions from a Parallel Hybrid Combustion Engine and Electric Powertrain. *SAE Technical Paper 2015-24-2538* (2015). DOI: `10.4271/2015-24-2538`

I. Denbratt defined the scope of the work and supervised the project along with S. Hemdal. L. C. R. Johansen performed the experimental work in conjunction with

Research Engineer D. Härensten and R. Arvidsson from Volvo Car Corporation. L. C. R. Johansen wrote the manuscript.

Paper D

- L. C. Johansen, E. de Benito Sienes, and P. Dahlander. Analysis of Transient Compressible Gas Jets Using High Speed Schlieren Imaging. *SAE Technical Paper 2013-01-0871* (2013). DOI: `10.4271/2013-01-0871`

L. C. R Johansen defined the scope of the work. P. Dahlander supervised the project. L. C. R. Johansen and E. de Benito Sienes performed the experimental. L. C. R. Johansen wrote the manuscript.

Appendix A

Thermophysical Properties

Thermophysical properties of pure substances and mixtures of these, if available, are generally provided first and foremost in tabulated form based on experimental measurements. Equations which relate thermodynamic variables are to a lesser degree available based on these experimental values. A detailed overview of the sources and relations for thermophysical properties is provided by [PPO01]. In the following sections, data and equations providing values for a subset of the properties of substances relevant in engine applications are discussed, based in large part on the information provided by [PPO01].

A.1 Multiparameter Equations of State

Certain relations can provide multiple thermophysical properties. The Helmholtz free energy equation of state (EoS) is a multiparameter equation of state which provides equations for, amongst other, the following properties:

- $p\rho T$ relation
- Isochoric and isobaric specific heat capacities, c_V c_p
- Internal energy, u
- Enthalpy, h
- Compressibility factor, Z

Helmholtz free energy EoS can provide accurate values over a wide range of conditions when they are based on careful fitting to experimental values. The sources of Helmholtz free energy EoS for various engine relevant species are listed in Table A.1.

Species	Source
Hydrogen	[Lea+09]
Methane	[SW91]
Methanol	[PS13]
Ethanol	[SPS14]
n-Hexane	[SW03a], [SW03b]
n-Heptane	[SW03a], [SW03b]

Table A.1: Helmholtz free energy multiparameter equation of state sources for various species

A.2 Vapour Pressure

The simplest correlation for vapour pressure of a species as a function of temperature is the Antoine equation given in Eq. A.1.

$$\log_{10}\left(\frac{P_{\mathrm{vp}}}{1\,\mathrm{bar}}\right) = A - \frac{B}{\dfrac{T}{1\,\mathrm{K}} + C - 273.15} \tag{A.1}$$

where P_{vp} is the vapour pressure, T is the temperature and A, B and C are parameters. The values of the parameters for a wide range of chemical species are provided by [PPO01]. The extended Antoine equation in Eq. A.2a provides a relation for vapour pressure at larger temperatures.

$$\log_{10}\left(\frac{P_{\mathrm{vp}}}{1\,\mathrm{bar}}\right) = A - \frac{B}{\dfrac{T}{1\,\mathrm{K}} + C - 273.15} + 0.43429x^n + Ex^n + Fx^n \tag{A.2a}$$

$$x = \frac{T - t_0 + 273.15\,\mathrm{K}}{T_c} \tag{A.2b}$$

A.3 Enthalpy of Vapourization

The vapour pressure and enthalpy of vapourization are related through the Clapeyron equation in Eq. A.3.

$$\frac{\mathrm{d}P_{\mathrm{vp}}}{\mathrm{d}T} = \frac{\Delta H_{\mathrm{v}}}{T\Delta V_{\mathrm{v}}} \tag{A.3}$$

where ΔH_{v} is the enthalpy of vapourization and ΔV_{v} is the difference in volume between the saturated liquid and saturated vapour at a given temperature or pressure. (To be completed).

Name	Eq. #	$A\,/A/T_\mathrm{c}$	$B\,/B/a$	$C\,/C/b$	$-\bigg/\frac{T_\mathrm{c}}{1\,\mathrm{K}}\bigg/c$	$-\bigg/\frac{t_0}{1\,\mathrm{K}}\bigg/d$	$-\bigg/n\bigg/\frac{P_\mathrm{c}}{1\,\mathrm{bar}}$	$-/-/E$	$-/-/F$	$\frac{P_\mathrm{vp,min}}{1\,\mathrm{bar}}$	$\frac{T_\mathrm{min}}{1\,\mathrm{K}}$	$\frac{P_\mathrm{vp,max}}{1\,\mathrm{bar}}$	$\frac{T_\mathrm{max}}{1\,\mathrm{K}}$
2,2,4-trimethylpentane	A.1	3.936 46	1257.850	220.767						0.02	275.5	2	398.38
	A.2a	3.936 46	1257.850	220.767	543.90	124	2.132 61	134.5	12 998.0	1.9889	398.15	25.42	543.15

Table A.2: Vapour pressure correlation parameters for Eq. A.1 and A.2a [PPO01]

A.4 Surface Tension

Eq. A.4 is a three parameter equation for the surface tension, σ, from the triple point to the critical point proposed by [Som88] along with the parameters for a number of liquid compounds.

$$\sigma = a\left(\frac{T_\mathrm{c}-T}{T_\mathrm{c}}\right)^{\frac{5}{4}} + b\left(\frac{T_\mathrm{c}-T}{T_\mathrm{c}}\right)^{\frac{9}{4}} + c\left(\frac{T_\mathrm{c}-T}{T_\mathrm{c}}\right)^{\frac{13}{4}} \tag{A.4}$$

Compound	T_t	T_c	$a\big/\left(\mathrm{N\,m^{-1}}\right)$	$b\big/\left(\mathrm{N\,m^{-1}}\right)$	$c\big/\left(\mathrm{N\,m^{-1}}\right)$
Methanol	175.59	512.64	122.6257	−199.4044	153.3744
Ethanol	159.0	513.92	111.4452	−146.0229	89.5703
Hexane	177.83	507.50	52.2937	6.1685	−3.5869
Heptane	182.55	540.30	54.1778	−0.758 56	3.9897

Table A.3: Compound parameters for Eq. A.4 provided by [Som88]

Appendix B

Heat Release Analysis

The purpose of heat release analysis is to determine how the combustion process in an internal combustion engine cylinder evolves from ignition until combustion has completed, primarily using cylinder pressure data. Combustion in the cylinder of an engine converts chemical energy stored in the fuel–air mixture to sensible energy, and in turn a fraction of the sensible energy is converted to work performed on the piston. The combustion process determines the fuel conversion efficiency, the net work output and the quantity of pollutants formed. A method for examining the combustion process is needed in order to investigate how combustion is affected by engine variables and how in turn the combustion process influences the previously stated measures of performance.

A time resolved view of combustion in the cylinder is provided by the rate of heat release $\dot{Q}_{\text{ch}}$ which is the time rate of conversion of chemical energy to sensible energy and the total heat release Q_{ch} which is the sum of the chemical energy released by combustion at a given point in time. Q_{ch} can be determined by integrating $\dot{Q}_{\text{ch}}$ from the start of combustion to the specified time. The total heat release is proportional to $x_b\,[-]$, the mass fraction of the fuel which has combusted. From the total heat release it is possible to determine the crank angle duration of the initial flame development θ_d and of the rapid burning phase θ_r, the crank angle at which 50% of the fuel has combusted (CA50 [°]), stability, variation, abnormal combustion and combustion efficiency, as discussed by [Hey89], which can be used to characterize and analyze the combustion process.

The rate of heat release is not directly measurable. The most readily measurable quantity providing a measure of the combustion process in a cylinder is the cylinder pressure p. The cylinder pressure increases as combustion progresses due to the resulting increase in cylinder gas temperature T. The pressure is therefore a function of the rate of heat release and this relationship provides a way of determining the rate of heat release from the cylinder pressure. However, the cylinder pressure also changes due to the following:

- The cylinder volume V changes during combustion
- Heat transfer Q_{ht} from the cylinder gases to solid boundaries decreases the gas temperature

- Vaporization of liquid fuel in the cylinder decreases the gas temperature
- Gas leaking from the cylinder through crevices decreases the mass in the cylinder

The goal of heat release analysis is to seperate the effect of combustion on the cylinder pressure from the effects of any other phenomena. The accuracy of any method relating cylinder pressure to heat release will therefore depend on which of the phenomena other than combustion are accounted for, the accuracy of the models for the phenomena, and the magnitude of the effect of each neglected term on the cylinder pressure, relative to combustion.

B.1 Conservation of Energy

[Gat+84] derive an expression for the heat release Q_{ch} from the conservation of energy. The first law of thermodynamics, which expresses the conservation of energy is reformulated in terms of measured thermodynamic state variables and known engine operating variables. The first law of thermodynamics is typically stated in terms of the internal energy U, heat transfer Q and work transfer W which are not easily measured. To solve this, the first law can be reformulated in terms of the thermodynamic state variables p, T, V and $c_p/c_v = \gamma$, the ratio of constant pressure specific heat capacity to the constant volume specific heat capacity, which are somewhat more straightforward to determine. The task of reformulating the first law to obtain the equation for heat release in terms of measured and known variables is covered in detail in the following, based on the approach outlined by [Gat+84]. The differential form of the 1st law of thermodynamics for an open control volume can be stated as given in Eq. B.1.

$$\mathrm{d}U = \underbrace{\delta Q}_{\text{pos. in}} - \underbrace{\delta W}_{\text{pos. out}} + \sum h_i \underbrace{\mathrm{d}m_i}_{\text{pos. in}} \tag{B.1}$$

where $\mathrm{d}U$ is the differential change in internal energy (both sensible and formation energy) of the control volume, δQ is the differential heat transfer *to* the control volume, δW is differential work transfer *from* the control volume, $\mathrm{d}m_i$ is the differential mass transfer *into* the control volume and h_i is the specific enthalpy of the differential mass $\mathrm{d}m_i$. The kinetic and potential energy of the differential mass $\mathrm{d}m_i$ has been neglected in Eq. B.1. The sign convention used is indicated in Eq. B.1. The differential heat and work transfer are inexact differentials as denoted by δ, indicating that Q and W are functions of the path taken between an initial state 1 and final state 2. The path must therefore be known in order to integrate δQ and δW and determine the heat and work transfer between an initial and final state. For $\mathrm{d}U$, an exact differential, it is sufficient to know the initial and final state in order to integrate and obtain the change in U between two states.

In general the cylinder gas will not have a uniform composition or thermodynamic state. For example, during combustion the cylinder will contain a mass fraction which has combusted and therefore consists primarily of the reaction products H_2O, CO_2 in addition to N_2, and a mass fraction which has not yet combusted and therefore consists

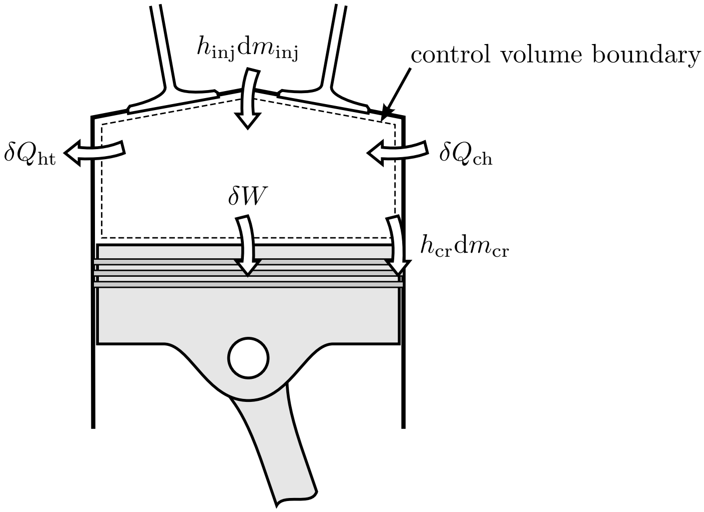

Figure B.1: *A cylinder combustion chamber control volume with energy and mass transfers shown.*

primarily of a mixture of fuel and air. Furthermore, fuel and air which combusts at the beginning of the cylinder combustion will have a temperature approximately 400 greater than the mass which combusts at the end of combustion in the case of a gasoline fueled spark ignition engine operating homogenously as discussed by [Hey89].

B.2 One Zone Heat Release

Gatowski et al. use a single control volume consisting of the engine cylinder combustion chamber volume, as illustrated in Figure B.1. In Figure B.1, δQ_{ch} is the differential heat transfer to the control volume representing the combustion heat release, δW is the differential work transfer from the control volume to the cylinder piston, δQ_{ht} is the differential heat transfer from the control volume to the cylinder walls, $\mathrm{d}m_{\mathrm{inj}}$ is the differential fuel mass entering the cylinder and $\mathrm{d}m_{cr}$ is the differential cylinder gas mass leaving the cylinder and entering the crevice volume.

Gatowski et al. point out that when multiple control volumes are used, the geometry of the control volumes for the burnt and unburnt gases must be determined in order to calculate the heat transfer to the cylinder walls and the composition and state of the gases leaving the combustion chamber through crevices between the piston and the cylinder walls. This calculation is not required when a single control volume is used.

With a control volume for Eq. B.1 now defined as shown in Figure B.1, the next step in determining a relation for Q_{ch} from Eq. B.1 involves reformulating each term in Eq. B.1 in terms of Q_{ch} and the thermodynamic state variables p, T, v, c_v and c_p. Following the approach of Gatowski et al., the heat release equation will be derived for the case of a premixed fuel-air cylinder mixture in which there is no fuel injection into the cylinder, and the case of a non-premixed cylinder mixture in which fuel injection into the cylinder takes place.

B.2.1 General One-Zone Heat Release Equation

Internal Energy

The internal energy U of a mixture can be divided into the sensible internal energy U_{s}, which is associated with the internal energy due to the temperature of the mixture, and the internal energy of formation U_{f} which is the internal energy associated with the bonds of the molecules in the mixture and therefore depends on the mixture species composition. U can therefore be expressed as the sum of U_{s} and U_{f} as stated in Eq. B.2.

$$U = U_{\mathrm{s}} + U_{\mathrm{f}} \tag{B.2}$$

Given the equality $\mathrm{d}\left(ca\right) = c\mathrm{d}\left(a\right)$ for a differential of variable a multiplied by a constant c, and the equality $\mathrm{d}\left(ab\right) = \mathrm{d}a + \mathrm{d}b$ for a differential of a sum $a + b$, the differential internal energy $\mathrm{d}U$ is given by Eq. B.3.

$$\mathrm{d}U = \mathrm{d}\left(U_{\mathrm{s}} + U_{\mathrm{f}}\right) = \mathrm{d}U_{\mathrm{s}} + \mathrm{d}U_{\mathrm{f}} \tag{B.3}$$

Since the internal energy of formation is associated with the composition, when a mixture combusts and the composition changes as a result, there will in general occur a change ΔU_{f} in the internal energy of formation of the mixture. When ΔU_{f} is negative, the energy stored in the bonds of the mixture molecules, often denoted chemical energy, is converted to sensible energy as a result of a change in the molecular composition of the mixture. The energy converted to sensible energy is defined as the heat release Q_{ch} and is positive for a negative change in the internal energy of formation ie. a release of chemical energy. This is expressed in Eq. B.4.

$$-\Delta U_{\mathrm{f}} = Q_{\mathrm{ch}} \tag{B.4}$$

In effect, Gatowski et al. model the conversion of chemical energy to sensible energy and the resulting change in the internal energy of formation, as heat transfer to the control volume. This is illustrated in Figure B.1 and explains the choice of the term heat release and Q_{ch} to denote this quantity. As the change in the internal energy of formation ΔU_{f} in Eq. B.4 approaches zero it becomes infinitesimally small and can be replaced by the differential change in internal energy of formation $\mathrm{d}U_{\mathrm{f}}$. Under this condition Q_{ch} in Eq. B.4 similarly becomes infinitesimally small and can be replaced by the differential heat release δQ_{ch}. An inexact differential is used for Q_{ch} in keeping with the analogy that the formation energy converted to sensible energy is provided by a heat transfer which is an inexact differential quantity. Making these substitutions in Eq. B.4 results in Eq. B.6.

$$-\mathrm{d}U_{\mathrm{f}} = \delta Q_{\mathrm{ch}} \tag{B.5}$$

Substituting Eq. B.5 into Eq. B.3 yields Eq. B.6.

$$
\begin{aligned}
\mathrm{d}U &= \mathrm{d}U_{\mathrm{s}} + \mathrm{d}U_{\mathrm{f}} \Rightarrow \\
\mathrm{d}U &= \mathrm{d}U_{\mathrm{s}} - \delta Q_{\mathrm{ch}}
\end{aligned}
\tag{B.6}
$$

Eq. B.6 expresses the differential internal energy $\mathrm{d}U$ in terms of the differential sensible internal energy $\mathrm{d}U_{\mathrm{s}}$ and the differential heat release δQ_{ch}. The goal is to reformulate Eq. B.1 to obtain an expression for Q_{ch} and Eq. B.6 provides a relation between $\mathrm{d}U$ in Eq. B.1 and δQ_{ch} and thereby a way of introducing Q_{ch} into Eq. B.1 in the form of δQ_{ch}.

$\mathrm{d}U_{\mathrm{s}}$ remains to formulated in terms of known variables. Given the equality $\mathrm{d}\left(ab\right) = \mathrm{d}\left(a\right)b + a\mathrm{d}\left(b\right)$ for the differential of the product of the variables a and b, Eq. B.7 follows for $\mathrm{d}U_{\mathrm{s}}$.

$$
\mathrm{d}U_{\mathrm{s}} = \mathrm{d}\left(mu_{\mathrm{s}}\right) = \mathrm{d}\left(m\right)u_{\mathrm{s}} + m\mathrm{d}\left(u_{\mathrm{s}}\right) \tag{B.7}
$$

Eq. B.7 expresses $\mathrm{d}U_{\mathrm{s}}$ in terms of the control volume mass m, which is the mass in the cylinder, and the specific sensible internal energy u_{s}. Eq. B.7 states that a differential change in sensible internal energy $\mathrm{d}U_{\mathrm{s}}$ results from a differential change in mass $\mathrm{d}m$, or a differential change in specific sensible internal energy $\mathrm{d}u_{\mathrm{s}}$. The task is then to reformulate u_{s} and $\mathrm{d}u_{\mathrm{s}}$ in terms of thermodynamic state variables.

For an ideal gas, u_{s} is dependent only on the temperature T of the gas and the cylinder mass is assumed to behave as an ideal gas. The total differential of a variable $a\left(x_1, x_2, \ldots, x_i \ldots, x_N\right)$ which is a function of N independent variables x_i is given by Eq. B.8.

$$
\mathrm{d}a = \sum_{i=1}^{N} \frac{\partial a}{\partial x_i}\mathrm{d}x_i \tag{B.8}
$$

Given that u_{s} is a function of T alone for an ideal gas, i.e. $u_{\mathrm{s}}\left(T\right)$, it follows from Eq. B.8 that $\mathrm{d}u_{\mathrm{s}}$ can be expressed as shown in Eq. B.9.

$$
\mathrm{d}u_{\mathrm{s}} = \frac{\partial u_{\mathrm{s}}}{\partial T}\mathrm{d}T \tag{B.9}
$$

where $\mathrm{d}T$ is the differential change in temperature. Eq. B.9 still leaves the partial derivative of u_{s} with respect to T to be determined. From thermodynamics this term is equal to the constant volume specific heat capacity c_v as expressed in Eq. B.10.

$$
\frac{\partial u_{\mathrm{s}}}{\partial T} = c_v \tag{B.10}
$$

$c_v\left(T\right)$ is itself a function of T. Substituting Eq. B.10 into Eq. B.9 results in Eq. B.11.

$$
\begin{aligned}
\mathrm{d}u_{\mathrm{s}} &= \frac{\partial u_{\mathrm{s}}}{\partial T}\mathrm{d}T \Rightarrow \\
\mathrm{d}u_{\mathrm{s}} &= c_v\mathrm{d}T
\end{aligned}
\tag{B.11}
$$

Eq. B.11 provides a relation for $\mathrm{d}u_{\mathrm{s}}$ in terms of T and c_v. The differential change in sensible internal energy $\mathrm{d}u_{\mathrm{s}}$ is due to a differential change in temperature $\mathrm{d}T$. Given that it has been assumed that the cylinder gases behave as an ideal gas, the temperature T can be determined from the ideal gas equation given in Eq. B.13.

$$\begin{aligned} pV &= nR_uT \Rightarrow && \text{(B.12)} \\ pV &= \frac{m}{M}R_uT \Rightarrow && \\ pV &= mRT \Rightarrow && \\ T &= \frac{pV}{mR} && \text{(B.13)} \\ m &= \frac{pV}{RT} && \text{(B.14)} \end{aligned}$$

where n is the number of moles of the gas, R_u is the universal gas constant, R is the specific gas constant and M is the molar mass of the gas. Using the ideal gas equation in Eq. B.13 and the equation for the total differential of a variable in Eq. B.8, the total differential $\mathrm{d}T$ in terms of the ideal gas variables in Eq. B.15 yields Eq. B.16 for $\mathrm{d}T$.

$$\begin{aligned} \mathrm{d}T &= \frac{\partial T}{\partial p}\mathrm{d}p + \frac{\partial T}{\partial V}\mathrm{d}V + \frac{\partial T}{\partial m}\mathrm{d}m + \frac{\partial T}{\partial R}\mathrm{d}R \Rightarrow && \text{(B.15)} \\ \mathrm{d}T &= \frac{V}{mR}\mathrm{d}p + \frac{p}{mR}\mathrm{d}V - \frac{pV}{m^2R}\mathrm{d}m - \frac{pV}{mR^2}\mathrm{d}R && \text{(B.16)} \end{aligned}$$

Eq. B.16 relates the change in T to the change in p, V, m and R. The differential $\mathrm{d}R$ occurs because R is a function of the molar mass M of the gas which in turn is dependent on the composition of the gas which in general will change. As a result, R is not in general a constant. Substituting Eq. B.16 for $\mathrm{d}T$ in Eq. B.11 results in Eq. B.17.

$$\begin{aligned} \mathrm{d}u_{\mathrm{s}} &= c_v\mathrm{d}T \Rightarrow && \\ \mathrm{d}u_{\mathrm{s}} &= c_v\left(\frac{V}{mR}\mathrm{d}p + \frac{p}{mR}\mathrm{d}V - \frac{pV}{m^2R}\mathrm{d}m - \frac{pV}{mR^2}\mathrm{d}R\right) && \text{(B.17)} \end{aligned}$$

which after rearrangement yields Eq. B.18.

$$\mathrm{d}u_{\mathrm{s}} = c_v\frac{pV}{mR}\left(\frac{\mathrm{d}p}{p} + \frac{\mathrm{d}V}{V} - \frac{\mathrm{d}m}{m} - \frac{\mathrm{d}R}{R}\right) \qquad \text{(B.18)}$$

Eq. B.18 relates the differential sensible internal energy $\mathrm{d}u_{\mathrm{s}}$ to the control volume pressure p, volume V, mass m and gas constant R and changes in these variable as expressed by the differentials of the variables. Substituting Eq. B.18 for $\mathrm{d}u_{\mathrm{s}}$ in Eq. B.7 yields Eq. B.19.

$$\begin{aligned}\mathrm{d}U_\mathrm{s} &= u_\mathrm{s}\mathrm{d}m + m\mathrm{d}u_\mathrm{s} \Rightarrow \\ \mathrm{d}U_\mathrm{s} &= u_\mathrm{s}\mathrm{d}m + c_v\frac{pV}{R}\left(\frac{\mathrm{d}p}{p}+\frac{\mathrm{d}V}{V}-\frac{\mathrm{d}m}{m}-\frac{\mathrm{d}R}{R}\right)\end{aligned} \tag{B.19}$$

Substituting Eq. B.19 for $\mathrm{d}U_\mathrm{s}$ in Eq. B.6 yields Eq. B.20 for $\mathrm{d}U$.

$$\begin{aligned}\mathrm{d}U &= \mathrm{d}U_\mathrm{s} - \delta Q_\mathrm{ch} \Rightarrow \\ \mathrm{d}U &= u_\mathrm{s}\mathrm{d}m + c_v\frac{pV}{R}\left(\frac{\mathrm{d}p}{p}+\frac{\mathrm{d}V}{V}-\frac{\mathrm{d}m}{m}-\frac{\mathrm{d}R}{R}\right) - \delta Q_\mathrm{ch}\end{aligned} \tag{B.20}$$

Substituting Eq. B.20 for $\mathrm{d}U$ in Eq. B.1 yield Eq. B.21 for δQ_ch.

$$\begin{aligned}\mathrm{d}U &= \delta Q - \delta W + \sum h_i\mathrm{d}m_i \Rightarrow \\ u_\mathrm{s}\mathrm{d}m + c_v\frac{pV}{R}\left(\frac{\mathrm{d}p}{p}+\frac{\mathrm{d}V}{V}-\frac{\mathrm{d}m}{m}-\frac{\mathrm{d}R}{R}\right) - \delta Q_\mathrm{ch} &= \delta Q - \delta W + \sum h_i\mathrm{d}m_i\end{aligned} \tag{B.21}$$

By substituting the ideal gas equation $m = pV/RT$ in Eq. B.14 for m in Eq. B.21 and solving for δQ_ch, Eq. B.22 for δQ_ch is obtained.

$$\delta Q_\mathrm{ch} = c_v\frac{pV}{R}\left(\frac{\mathrm{d}p}{p}+\frac{\mathrm{d}V}{V}-\frac{RT}{pV}\mathrm{d}m-\frac{\mathrm{d}R}{R}\right) + u_\mathrm{s}\mathrm{d}m - \delta Q + \delta W - \sum h_i\mathrm{d}m_i \tag{B.22}$$

Collecting the terms in Eq. B.22 involving $\mathrm{d}m$ yields Eq. B.23

$$\delta Q_\mathrm{ch} = c_v\frac{pV}{R}\left(\frac{\mathrm{d}p}{p}+\frac{\mathrm{d}V}{V}-\frac{\mathrm{d}R}{R}\right) + \left(u_\mathrm{s} - c_vT\right)\mathrm{d}m - \delta Q + \delta W - \sum h_i\mathrm{d}m_i \tag{B.23}$$

Gatowski et al. replace c_v in the first term on the right hand side of Eq. B.22 with $\gamma = c_p/c_v$, the ratio of the constant pressure and constant volume specific heat capacities. For an ideal gas Eq. B.24 relates c_v, c_p and R.

$$c_p - c_v = R \tag{B.24}$$

where c_p is the gas constant pressure specific heat capacity. Rearranging Eq. B.24 yields Eq. B.25 and B.26 for c_v and c_p respectively in terms of γ and R.

$$\begin{aligned}\frac{c_p}{c_v} - 1 = \frac{R}{c_v} &\Rightarrow \gamma - 1 = \frac{R}{c_v} \Rightarrow \\ c_v &= \frac{R}{\gamma - 1}\end{aligned} \tag{B.25}$$

$$1 - \frac{c_v}{c_p} = \frac{R}{c_p} \Rightarrow 1 - \frac{1}{\gamma} = \frac{R}{c_p} \Rightarrow$$
$$c_p = \frac{R\gamma}{\gamma - 1} \tag{B.26}$$

Substituting Eq. B.25 for c_v in the first right hand term of Eq. B.23 yields Eq. B.27.

$$\delta Q_{\text{ch}} = \frac{pV}{\gamma - 1}\left(\frac{\mathrm{d}p}{p} + \frac{\mathrm{d}V}{V} - \frac{\mathrm{d}R}{R}\right) + \left(u_{\text{s}} - c_v T\right)\mathrm{d}m - \delta Q + \delta W - \sum h_i \mathrm{d}m_i \tag{B.27}$$

p is known from measurements. V is determined from the cylinder geometry and the crank angle as detailed in subsubsection B.2.1. T can be calculated from the ideal gas equation when m and R are known. R is dependent on the cylinder mixture composition. The cylinder composition depends on the initial (before combustion) cylinder conditions and the mass fraction of the fuel-air mixture that has combusted and therefore is a function of δQ_{ch}. The composition can be determined from the heat release and the reaction mechanism as discussed in the following sections. If the cylinder mass species composition at given time is known, then $\gamma\left(T\right)$, $c_v\left(T\right)$ and $u_{\text{s}}\left(T\right)$ can be calculated from the aforementioned variable values and suitable thermodynamic property functions.

Leaving aside the determination of the initial cylinder state, the remaining unknown quantities in Eq. B.43 are thusfar:

- Cylinder volume V and differential of the volume $\mathrm{d}V$
- Gas constant R as a function of composition at a given time and differential $\mathrm{d}R$ as a result
- Differential change in the total mass $\mathrm{d}m$ in the cylinder
- Differential heat transfer δQ *to* the cylinder
- Differential work transfer *from* the cylinder δW
- Differential mass flows $\mathrm{d}m_i$ *into* the cylinder

Cylinder Volume

The total cylinder volume, V, is the sum of the displacement volume, V_d, and the clearence volume V_{c} as shown in Eq. B.28.

$$V = V_{\text{d}} + V_{\text{c}} \tag{B.28}$$

The clearance volume is constant. The displacement volume is given by Eq. B.29.

$$V_{\mathrm{d}} = \frac{\pi^2}{4} B^2 \left(l + r - s\right) \tag{B.29}$$

where B is the cylinder diameter (bore), l is the distance between the centers of revolution of the connecting rod, r is half of the distance between piston at top dead center and bottom dead center (stroke) and s is the distance from the center of the piston pin to the center of revolution for the crankshaft. l, and r are constant while s is determined with Eq. B.30

$$s = r\cos\theta + \left(l^2 - r^2\sin^2\theta\right)^{\frac{1}{2}} \tag{B.30}$$

Substituting Eq. B.29 and Eq. B.30 into Eq. B.28 yields Eq. B.31.

$$V = \frac{\pi^2}{4} B^2 \left(l + r - r\cos\theta + \left(l^2 - r^2\sin^2\theta\right)^{\frac{1}{2}}\right) + V_{\mathrm{c}} \tag{B.31}$$

In addition to the total cylinder volume, the derivative of the cylinder volume with respect to crank angle is required for the differential energy conservation equations. This is given in Eq. B.34 derived from Eq. B.32 and Eq. B.33.

$$\frac{\mathrm{d}V}{\mathrm{d}\theta} = \frac{\mathrm{d}V_{\mathrm{d}}}{\mathrm{d}\theta} = -\frac{\pi^2}{4} B^2 \frac{\mathrm{d}s}{\mathrm{d}\theta} \tag{B.32}$$

$$\frac{\mathrm{d}s}{\mathrm{d}\theta} = -r\sin\theta + \frac{1}{2}\left(l^2 - r^2\sin^2\theta\right)^{-\frac{1}{2}}\left(-2r^2\sin\theta\cos\theta\right) \tag{B.33}$$

$$\frac{\mathrm{d}V}{\mathrm{d}\theta} = \frac{\pi^2}{4} B^2 \left(r\sin\theta + \frac{1}{2}\left(l^2 - r^2\sin^2\theta\right)^{-\frac{1}{2}}\left(2r^2\sin\theta\cos\theta\right)\right) \tag{B.34}$$

Work Transfer

The differential work tranfer δW between the control volume and the surroundings is positive for work transfer *from* the control volume to the surroundings. From thermodynamics the differential work transfer δW *from* a control volume equals the product of the pressure p and the differential change in volume $\mathrm{d}V$ as shown in Eq. B.35.

$$\delta W = p\mathrm{d}V \tag{B.35}$$

This provides a relation between the work transfer and the control volume state variables p and V. Substituting Eq. B.35 for δW in Eq. B.43 and collecting the terms involving $\mathrm{d}V$ yields Eq. B.36.

$$\delta Q_{\mathrm{ch}} = \frac{1}{\gamma - 1}\left(V\mathrm{d}p + p\mathrm{d}V\right) + \left(u_{\mathrm{s}} - c_v T\right)\mathrm{d}m - \delta Q + \delta W - \sum h_i \mathrm{d}m_i \Rightarrow$$
$$\delta Q_{\mathrm{ch}} = \frac{1}{\gamma - 1} V\mathrm{d}p + \left(\frac{1}{\gamma - 1} + 1\right) p\mathrm{d}V + \left(u_{\mathrm{s}} - c_v T\right)\mathrm{d}m - \delta Q - \sum h_i \mathrm{d}m_i \Rightarrow$$
$$\delta Q_{\mathrm{ch}} = \frac{1}{\gamma - 1} V\mathrm{d}p + \frac{\gamma}{\gamma - 1} p\mathrm{d}V + \left(u_{\mathrm{s}} - c_v T\right)\mathrm{d}m - \delta Q - \sum h_i \mathrm{d}m_i \tag{B.36}$$

Composition

The term $\mathrm{d}R$ can be determined from the definition of R in Eq. B.37 and the molar mass of a mixture in Eq. B.38a and B.38b.

$$R = \frac{R_u}{M} \tag{B.37}$$

$$M = \frac{m}{n} = \frac{\sum m_i}{n} = \frac{\sum n_i M_i}{n} = \sum x_i M_i \tag{B.38a}$$
$$= \frac{m}{\sum n_i} = \frac{m}{\sum \frac{m_i}{M_i}} = \frac{1}{\sum \frac{y_i}{M_i}} \tag{B.38b}$$

From Eq. B.37 $\mathrm{d}R$ is given by Eq. B.39.

$$\mathrm{d}R = \frac{\partial}{\partial M}\left(\frac{R_u}{M}\right)\mathrm{d}M = -\frac{R_u}{M^2}\mathrm{d}M \tag{B.39}$$

As shown in Eq. B.38a and B.38b, M is dependent on the composition and is therefore a variable. In contrast, the individual species molar masses M_i are constant. From Eq. B.38b $\mathrm{d}M$ is given by Eq. B.40.

$$\mathrm{d}M = \sum_j \frac{\partial}{\partial y_j}\left(\frac{1}{\sum_i \frac{y_i}{M_i}}\right)\mathrm{d}y_j = \frac{1}{\left(\sum_i \frac{y_i}{M_i}\right)^2}\sum_j -\frac{1}{M_j}\mathrm{d}y_j = M^2 \sum_j -\frac{1}{M_j}\mathrm{d}y_j \tag{B.40}$$

The last substitution providing M^2 in Eq. B.40 uses Eq. B.38b. Substituting Eq. B.40 into Eq. B.39 provides Eq. B.41.

$$\mathrm{d}R = R_u \sum_j \frac{1}{M_j}\mathrm{d}y_j \tag{B.41}$$

Eq. B.41 requires an expression for $\mathrm{d}y_j$ which is determined in Eq. B.42 from the definition of the mass fraction.

$$\mathrm{d}y_j = \mathrm{d}\left(\frac{m_j}{m}\right) = \frac{\partial}{\partial m_j}\left(\frac{m_j}{m}\right)\mathrm{d}m_j + \frac{\partial}{\partial m}\left(\frac{m_j}{m}\right)\mathrm{d}m \Rightarrow$$

$$\mathrm{d}y_j = \frac{1}{m}\mathrm{d}m_j - \frac{m_j}{m^2}\mathrm{d}m = \frac{1}{m}\left(\mathrm{d}m_j - y_j\mathrm{d}m\right) \tag{B.42}$$

B.2.2 Gatowski One Zone Premixed Equation

Gatowski et al. assume that the change dR can be neglected and do not include this term. This assumption is based on the molar mass M of the reactant and product gases being approximately equal and therefore $R = R_u/M$ remains approximately constant when employing this assumption. Eq. B.43 is the result of neglecting dR in Eq. B.27.

$$\delta Q_{\mathrm{ch}} = \frac{1}{\gamma - 1}\left(V\mathrm{d}p + p\mathrm{d}V\right) + \left(u_{\mathrm{s}} - c_v T\right)\mathrm{d}m - \delta Q + \delta W - \sum h_i \mathrm{d}m_i \tag{B.43}$$

Heat Transfer

The differential heat transfer *to* the control volume δQ, consists of the differential heat transfer δQ_{ht} between the cylinder control volume and the cylinder surfaces due to the temperature difference between the two. These surfaces are the piston head, the cylinder walls and the cylinder head. In the model for the heat transfer δQ_{ht}, heat transfer is positive *from* the control volume to the surroundings. This is the *opposite* direction of δQ which is positive for heat transfer *to* the control volume from the surroundings. δQ and δQ_{ht} therefore have opposite signs as expressed in Eq. B.44.

$$\delta Q = -\delta Q_{\mathrm{ht}} \tag{B.44}$$

Substituting Eq. B.44 for δQ in Eq. B.36 yields Eq. B.45 for δQ_{ch}

$$\delta Q_{\mathrm{ch}} = \frac{1}{\gamma - 1}V\mathrm{d}p + \frac{\gamma}{\gamma - 1}p\mathrm{d}V + \left(u_{\mathrm{s}} - c_v T\right)\mathrm{d}m - \delta Q - \sum h_i \mathrm{d}m_i$$

$$\delta Q_{\mathrm{ch}} = \frac{1}{\gamma - 1}V\mathrm{d}p + \frac{\gamma}{\gamma - 1}p\mathrm{d}V + \left(u_{\mathrm{s}} - c_v T\right)\mathrm{d}m + \delta Q_{\mathrm{ht}} - \sum h_i \mathrm{d}m_i \tag{B.45}$$

In addition to the heat transfer δQ_{ht} there is also the heat transfer δQ_{ch} which models the energy released by combustion as heat transfer *to* the cylinder control volume. This term has already been introduced as a component of the differential of the internal energy dU, by replacing the differential of the internal energy of formation dU_{f} component of dU with $-\delta Q_{\mathrm{ch}}$ as shown in Section B.2.1. δQ_{ch} could instead have been introduced as a component of δQ along with δQ_{ht}, in which case the internal energy is assumed to consist entirely of sensible internal energy without any internal energy of formation, i.e. $\mathrm{d}U = \mathrm{d}U_{\mathrm{s}}$ and $\delta Q = -\delta Q_{\mathrm{ht}} + \delta Q_{\mathrm{ch}}$. This is the approach taken by Gatowski et al. and explains the heat transfer notation for the heat release. Using this approach also leads to Eq. B.45. In order to determine the heat transfer δQ_{ht} a model which relates the heat transfer to known thermodynamic variables and engine parameters.

B.2.3 Simulated Pressure

Rather than determining the rate of heat release, given a specificed rate of fuel mass combustion, the cylinder pressure can be determined. The differential equation for dp in this case is given in Eq. B.46.

$$\mathrm{d}p = \frac{\gamma - 1}{V}\left(\delta Q_{\mathrm{ch}} - \left(u_{\mathrm{s}} - c_v T\right)\mathrm{d}m - \delta Q_{\mathrm{ht}} + \sum h_i \mathrm{d}m_i\right) - \frac{\gamma p}{V}\mathrm{d}V \tag{B.46}$$

The total heat release is given by Eq. B.47.

$$\begin{aligned} Q_{\mathrm{ch}} &= m_{\mathrm{b}}\mathrm{LHV} \Rightarrow \\ Q_{\mathrm{ch}} &= y_{\mathrm{b}} m_{\mathrm{f}}\mathrm{LHV} \end{aligned} \tag{B.47}$$

The total differential of the heat of heat release is determined from Eq. B.47 and given in Eq. B.48.

$$\begin{aligned} \mathrm{d}Q_{\mathrm{ch}} &= \mathrm{d}\left(y_{\mathrm{b}} m_{\mathrm{f}}\mathrm{LHV}\right) \Rightarrow \\ \mathrm{d}Q_{\mathrm{ch}} &= \mathrm{d}y_{\mathrm{b}} m_{\mathrm{f}}\mathrm{LHV} + y_{\mathrm{b}}\mathrm{d}m_{\mathrm{f}}\mathrm{LHV} + y_{\mathrm{b}} m_{\mathrm{f}}\mathrm{dLHV} \end{aligned} \tag{B.48}$$

The Wiebe function for the mass fraction of fuel burned is given by Eq. B.49.

$$y_{\mathrm{b}} = 1 - \exp\left(-a\left(\frac{\theta - \theta_0}{\Delta\theta}\right)^{b+1}\right) \tag{B.49}$$

The total differential of mass fraction burned as given by the Wiebe function in Eq. B.49 is given in Eq. B.50.

$$\frac{\mathrm{d}y_{\mathrm{b}}}{\mathrm{d}\theta} = \frac{a\left(b+1\right)}{\Delta\theta}\left(\frac{\theta - \theta_0}{\Delta\theta}\right)^{b}\exp\left(-a\left(\frac{\theta - \theta_0}{\Delta\theta}\right)^{b+1}\right) \tag{B.50}$$

References

[Aga07] A. K. Agarwal. Biofuels (alcohols and biodiesel) applications as fuels for internal combustion engines. *Energy Conversion and Management* **48** (2007), 2751–2761. DOI: `10.1016/j.enconman.2007.07.027`.

[Ale+10] P. G. Aleiferis et al. Mechanisms of spray formation and combustion from a multi-hole injector with E85 and gasoline. *Combustion and Flame* **157** (2010), 735–756. DOI: `10.1016/j.combustflame.2009.12.019`.

[Alk07] A. C. Alkidas. Combustion advancements in gasoline engines. *Energy Conversion and Management* **48** (2007), 2751–2761. DOI: `10.1016/j.enconman.2007.07.027`.

[AR13] P. G. Aleiferis and Z. R. van Romunde. An analysis of spray development with iso-octane, n-pentane, gasoline, ethanol and n-butanol from a multi-hole injector under hot fuel conditions. *Fuel* **105** (2013), 143–168. DOI: `10.1016/j.fuel.2012.07.044`.

[Arn+99] W. P. Arnott et al. Photoacoustic spectrometer for measuring light absorption by aerosol: instrument description. *Atmospheric Environment* **33** (17 1999), 2845–2852. DOI: `10.1016/S1352-2310(98)00361-6`.

[Bas09] R. van Basshuysen, ed. *Gasoline Engine with Direct Injection.* 1st. Vieweg+Teubner, 2009.

[BB09] W. Burger and M. J. Burge. *Principles of Digital Image Processing: Core Algorithms.* Springer London, 2009. ISBN: 978-1-84800-195-4. DOI: `10.1007/978-1-84800-195-4`.

[BCL14] F. Bonatesta, E. Chiappetta, and A. La Rocca. Part-load particulate matter from a GDI engine and the connection with combustion characteristics. *Applied Energy* **124** (2014), 366–376. DOI: `10.1016/j.apenergy.2014.03.030`.

[BKD10] R. Baert, A. Klaassen, and E. Doosje. Direct injection of high pressure gas: Scaling properties of pulsed turbulent jets. *SAE International Journal of Engines* **3**.2 (2010), 383–396. DOI: `10.4271/2010-01-2253`.

[Boc94] H. Bockhorn, ed. *Soot Formation in Combustion.* 1st. Vol. 59. Springer Series in Chemical Physics. Springer, 1994. DOI: `10.1007/978-3-642-85167-4`.

[Bow61] F. W. Bowditch. A New Tool for Combustion Research A Quartz Piston Engine. *SAE Technical Paper 610002* (1961). DOI: `10.4271/610002`.

[Bro+13] G. Broustail et al. Experimental determination of laminar burning velocity for butanol/iso-octane and ethanol/iso-octane blends for different initial pressures. *Fuel* **106** (2013), 310–317. DOI: `10.1016/j.fuel.2012.10.066`.

[BWS14] P. Bielaczyc, J. Woodburn, and A. Szczotka. Particulate Emissions from European Vehicles Featuring Direct Injection Spark Ignition Engines Tested Under Laboratory Conditions. *SAE International Journal of Fuels and Lubricants* **7**.2 (2014), 580–590. DOI: `10.4271/2014-01-1608`.

[Cav+94] A. Cavaliere et al. Fuel and Soot Oxidation in Diesel-Like Conditions. *Symposium (International) on Combustion* **25**.1 (1994), 167–174. DOI: `10.1016/S0082-0784(06)80641-7`.

[Cid96] P. E. Ciddor. Refractive index of air. new equations for the visible and near infrared. *Applied Optics* **35**.9 (1996), 1566–1573. DOI: `10.1364/AO.35.001566`.

[CVP03] S. A. Carl, M. Van Poppel, and J. Peeters. Identification of the CH + $O_2 \longrightarrow$ OH(A) + CO Reaction as the Source of OH(A–X) Chemiluminescence in $C_2H_2/O/H/O_2$ Atomic Flames and Determination of Its Absolute Rate Constant over the Range T = 296 to 511 K. *Journal of Physical Chemistry A* **107**.50 (2003), 11001–11007. DOI: `10.1021/jp035568j`.

[DC62] G. H. Dieke and H. M. Crosswhite. The ultraviolet bands of OH Fundamental data. *Journal of Quantitative Spectroscopy and Radiative Transfer* **2**.2 (1962), 97–199. DOI: `10.1016/0022-4073(62)90061-4`.

[Dir+14] P. Dirrenberger et al. Laminar burning velocity of gasolines with addition of ethanol. *Fuel* **115** (2014), 162–169. DOI: `10.1016/j.fuel.2013.07.015`.

[DP04] D. E. Dillon and S. G. Penoncello. A Fundamental Equation for Calculation of the Thermodynamic Properties of Ethanol. *International Journal of Thermophysics* **25**.2 (2004), 321–335. DOI: `10.1023/B:IJOT.0000028470.49774.14`.

[Dra+03] M. C. Drake et al. Piston Fuel Films as a Source of Smoke and Hydrocarbon Emissions from a Wall-Controlled Spark-Ignited Direct-Injection Engine. *SAE Technical Paper 2003-01-0547* (2003). DOI: `10.4271/2003-01-0547`.

[DT08] P. Dagaut and C. Togb. Experimental and Modeling Study of the Kinetics of Oxidation of Ethanol-Gasoline Surrogate Mixtures (E85 Surrogate) in a Jet-Stirred Reactor. *Energy & Fuels* **22** (2008), 3499–3505. DOI: `10.1021/ef800214a`.

[DV92] D. S. Dandy and S. R. Vosen. Numerical and Experimental Studies of Hydroxyl Radical Chemiluminescence in Methane-Air Flames. *Combustion Science and Technology* **82** (1992), 131–150. DOI: `10.1080/00102209208951816`.

[Eur96] European Parliament, Council of the European Union. *Directive 96/69/EC of the European Parliament and of the Council of 8 October 1996 amending Directive 70/220/EEC on the approximation of the laws of the Member States relating to measures to be taken against air pollution by emissions from motor vehicles.* OJ L 282, 1.11.1996. 1996. URL: `http://eur-lex.europa.eu/legal-content/en/ALL/?uri=CELEX:31996L0069`.

[FHG12] R. J. Farrauto, R. M. Heck, and S. T. Gulati. *Catalytic Air Pollution Control. Commercial Technology.* 3rd. Wiley, 2012. ISBN: 9780470275030.

[FJ67] C. P. Fenimore and G. W. Jones. Oxidation of soot by hydroxyl radicals. *Journal of Physical Chemistry* **71**.3 (1967), 593–597. DOI: `10.1021/j100862a021`.

[Foo+14] T. M. Foong et al. The octane numbers of ethanol blended with gasoline and its surrogates. *Fuel* **115** (2014), 727–739. DOI: `10.1016/j.fuel.2013.07.105`.

[Fra11] L. de Francqueville. Effects of Ethanol Addition in RON 95 Gasoline on GDI Stratified Combustion. *SAE Technical Paper 2011-24-0055* (2011). DOI: `10.4271/2011-24-0055`.

[Gat+84] J. A. Gatowski et al. Heat Release Analysis of Engine Pressure Data. *SAE Technical Paper 841359* (1984). DOI: `10.4271/841359`.

[Gay74] A. G. Gaydon. *The Spectroscopy of Flames*. 2nd. Springer, 1974. ISBN: 978-94-009-5722-0. DOI: `10.1007/978-94-009-5720-6`.

[GHJ06] P. Ghosh, K. J. Hickey, and S. B. Jaffe. Development of a Detailed Gasoline Composition-Based Octane Model. *Industrial and Engineering Chemistry Research* **45**.1 (2006), 337–345. DOI: `10.1021/ie050811h`.

[Gie+12] B. Giechaskiel et al. Measurement of Automotive Nonvolatile Particle Number Emissions within the European Legislative Framework: A Review. *Aerosol Science and Technology* **46**.7 (2012), 719–749. DOI: `10.1080/02786826.2012.661103`.

[Gie+14] B. Giechaskiel et al. Review of motor vehicle particulate emissions sampling and measurement: From smoke and filter mass to particle number. *Journal of Aerosol Science* **67** (2014), 48–86. DOI: `10.1016/j.jaerosci.2013.09.003`.

[Gov16] Government Offices of Sweden. *Fossil-free transport and travel: The Governments work to reduce the impact of transport on the climate*. Accessed 2016/08/22. 2016. URL: `http://www.government.se/government-policy/environment/fossil-free-transport-and-travel-the-governments-work-to-reduce-the-impact-of-transport-on-the-climate/`.

[GY08] I. Glassman and R. Yetter. *Combustion*. 4th. Academic Press, 2008. ISBN: 978-0-12-088573-2.

[Hay16] W. M. Haynes, ed. *CRC Handbook of Chemistry and Physics*. (Internet Version 2016). 96th. CRC Press/Taylor and Francis, 2016.

[Hem+11] S. Hemdal et al. In-cylinder soot imaging and emissions of stratified combustion in a spark-ignited spray-guided direct-injection gasoline engine. *International Journal of Engine Research* **12** (2011), 549–563. DOI: `10.1177/1468087411418167`.

[Hey89] J. Heywood. *Internal Combustion Engine Fundamentals*. McGraw-Hill Higher Education, 1989. ISBN: 978-0071004992.

[HNI14] K. Hayashida, S. Nagaoko, and H. Ishitani. Growth and oxidation of graphitic crystallites in soot particles within a laminar diffusion flame. *Fuel* **128** (2014), 148–154. DOI: `10.1016/j.fuel.2014.03.008`.

[HO99] P. G. Hill and P. Ouellette. Transient Turbulent Gaseous Fuel Jets for Diesel Engines. *Journal of Fluids Engineering* **121**.1 (1999), 93–101. DOI: `10.1115/1.2822018`.

[Inta] International Energy Agency. *IEA Sankey Diagram*. Accessed 2016-08-05. URL: `https://www.iea.org/Sankey/#?c=World&s=Final%20consumption`.

[Intb] International Energy Agency. *IEA - Unit Converter.* Accessed 2016-07-25. URL: `https://www.iea.org/statistics/resources/unitconverter/`.

[Int12] International Energy Agency. *Technology Roadmap. Fuel Economy of Road Vehicles.* 2012. URL: `http://www.iea.org/publications/freepublications/publication/Fuel_Economy_2012_WEB.pdf`.

[Int14a] Intergovernmental Panel on Climate Change. *Climate Change 2014. Mitigation of Climate Change. Contribution of Working Group III to the Fifth Assessment. Report of the Intergovernmental Panel on Climate Change.* Intergovernmental Panel on Climate Change, 2014. URL: `http://www.ipcc.ch/report/ar5/syr/`.

[Int14b] Intergovernmental Panel on Climate Change. *Climate Change 2014. Synthesis Report. Contribution of Working Groups I, II and III to the Fifth Assessment Report of the Intergovernmental Panel on Climate Change.* Intergovernmental Panel on Climate Change, 2014. URL: `http://www.ipcc.ch/report/ar5/syr/`.

[Int15] International Energy Agency. *CO2 Emissions from Fuel Combustion. Highlights (2015 Edition).* 2015. URL: `https://www.iea.org/publications`.

[JBD13] L. C. Johansen, E. de Benito Sienes, and P. Dahlander. Analysis of Transient Compressible Gas Jets Using High Speed Schlieren Imaging. *SAE Technical Paper 2013-01-0871* (2013). DOI: `10.4271/2013-01-0871`.

[JDH15] L. C. Johansen, I. Denbratt, and S. Hemdal. Drive Cycle Particulate and Gaseous Emissions from a Parallel Hybrid Combustion Engine and Electric Powertrain. *SAE Technical Paper 2015-24-2538* (2015). DOI: `10.4271/2015-24-2538`.

[Jer+09] S. Jerzembeck et al. Laminar burning velocities at high pressure for primary reference fuels and gasoline: Experimental and numerical investigation. *Combustion and Flame* **156** (2009), 292–301. DOI: `10.1016/j.combustflame.2008.11.009`.

[JH15a] L. C. R. Johansen and S. Hemdal. In cylinder visualization of stratified combustion of E85 and main sources of soot formation. *Fuel* **159** (2015), 392–411. DOI: `10.1016/j.fuel.2015.07.013`.

[JH15b] L. C. R. Johansen and S. Hemdal. In cylinder visualization of stratified combustion of E85 and main sources of soot formation. *Fuel* **159** (2015), 392–411. DOI: `10.1016/j.fuel.2015.07.013`.

[JHD13] A. N. Johansson, S. Hemdal, and P. Dahlander. Experimental Investigation of Soot in a Spray-Guided Single Cylinder GDI Engine Operating in a Stratified Mode. *SAE Technical Paper 2013-24-0052* (2013). DOI: `10.4271/2013-24-0052`.

[JHD16] L. C. R. Johansen, S. Hemdal, and I. Denbratt. Comparison of E10 and E85 Spark Ignited Stratified Combustion and Soot Formation. *Submitted to Fuel* (2016).

[Joh13] T. Johnson. Vehicular Emissions in Review. *SAE International Journal of Engines* **6**.2 (2013), 699–715. DOI: `10.4271/2013-01-0538`.

[Kar+14] P. Karjalainen et al. Exhaust particles of modern gasoline vehicles: A laboratory and an on-road study. *Atmospheric Environment* **97** (2014), 262–270. DOI: `10.1016/j.atmosenv.2014.08.025`.

[KBW11] P. Kulkarni, P. A. Baron, and K. Willeke. *Aerosol Measurement: Principles, Techniques, and Applications.* 3rd. Wiley, 2011. ISBN: 978-0470387412.

[KNC11] T. Korakianitis, A. M. Namasivayam, and R. J. Crookes. Natural-gas fueled spark-ignition (SI) and compression-ignition (CI) engine performance and emissions. *Progress in Energy and Combustion Science* **37**.1 (2011), 89–112. DOI: `doi:10.1016/j.pecs.2010.04.002`.

[Kuo05] K. K. Kuo. *Principles of Combustion.* 2nd. Wiley-Interscience, 2005. ISBN: 978-0471046899.

[Lea+09] J. W. Leachman et al. Fundamental Equations of State for Parahydrogen, Normal Hydrogen, and Orthohydrogen. *Journal of Physical and Chemical Reference Data* **38**.3 (2009), 721–748. DOI: `10.1063/1.3160306`.

[Lep+11] N. Leplat et al. Numerical and experimental study of ethanol combustion and oxidation in laminar premixed flames and in jet-stirred reactor. *Combustion and Flame* **158** (2011), 705–725. DOI: `10.1016/j.combustflame.2010.12.008`.

[LL93] C. H. Li and C. K. Lee. Minimum cross entropy thresholding. *Pattern Recognition* **26**.4 (1993), 617–625. DOI: `10.1016/0031-3203(93)90115-D`.

[LM14] P. J. Lindstrom and W. G. Mallard, eds. *NIST Chemistry WebBook, NIST Standard Reference Database Number 69.* National Institute of Standards and Technology, Apr. 2014. URL: `http://webbook.nist.gov`.

[LS06] E. W. Lemmon and R. Span. Short Fundamental Equations of State for 20 Industrial Fluids. *Journal of Chemical and Engineering Data* **51**.3 (2006), 785–850. DOI: `10.1021/je050186n`.

[LT98] C. H. Li and P. K. S. Tam. An iterative algorithm for minimum cross entropy thresholding. *Pattern Recognition Letters* **19**.8 (1998), 771–776. DOI: `10.1016/S0167-8655(98)00057-9`.

[Mam+13] A. Mamakos et al. Assessment of different technical options in reducing particle emissions from gasoline direct injection vehicles. *Journal of Aerosol Science* **63** (2013), 115–125. DOI: `10.1016/j.jaerosci.2013.05.004`.

[Mar+10] A. Marchi et al. Spray stability of outwards opening pintle injectors for stratified direct injection spark ignition engine operation. *International Journal of Engine Research* **11**.6 (2010), 413–437. DOI: `10.1243/14680874JER605`.

[Mar+12] P. Marti-Aldavari et al. "A comparison of non-reactive fuel sprays under realistic but quiescent engine conditions for SGDI". ICLASS 2012. 12th Triennial International Conference on Liquid Atomization and Spray Systems. 2012. URL: `http://www.ilasseurope.org/ICLASS/iclass2012_Heidelberg/Contributions/Paper-pdfs/Contribution1214_b.pdf`.

[Mar12] M. M. Maricq. Soot formation in ethanol/gasoline fuel blend diffusion flames. *Combustion and Flame* **159** (2012), 170–180. DOI: `10.1016/j.combustflame.2011.07.010`.

[Mod13] M. F. Modest. *Radiative Heat Transfer.* 3rd Edition. Academic Press, 2013. ISBN: 978-0-12-386944-9.

[Moh+08] A. Mohammadi et al. Spark-Ignition and Combustion Characteristics of High-Pressure Hydrogen and Natural-Gas Intermittent Jets. *Journal of Engineering for Gas Turbines and Power* **130**.6 (2008). DOI: `10.1115/1.2938271`.

[MP69] C. R. Mansfield and E. R. Peck. Dispersion of Helium. *Journal of the Optical Society of America* **59**.2 (1969), 100–204. DOI: `10.1364/JOSA.59.000199`.

[MPK10] D. Martin, P. Pischke, and R. Kneer. Investigation of the influence of multiple gasoline direct injections on macroscopic spray quantities at different boundary conditions by means of visualization techniques. *International Journal of Engine Research* **11**.6 (2010), 439–454. DOI: `10.1243/14680874JER525`.

[MST12] G. P. Merker, C. Schwarz, and R. Teichmann, eds. *Combustion Engines Development. Mixture Formation, Combustion, Emissions and Simulation.* Springer Berlin Heidelberg, 2012. ISBN: 978-3-642-14094-5. DOI: `10.1007/978-3-642-14094-5`.

[MW90] R. Malhotra and L. A. Woolf. Thermodynamic properties of 2,2,4-trimethylpentane. *International Journal of Thermophysics* **11**.6 (1990), 1059–1073. DOI: `10.1007/BF00500560`.

[NS11] P. S. Nigam and A. Singh. Production of liquid biofuels from renewable resources. *Progress in Energy and Combustion Science* **37** (2011), 52–68. DOI: `10.1016/j.pecs.2010.01.003`.

[OB13] H. Oh and C. Bae. Effects of the injection timing on spray and combustion characteristics in a spray-guided DISI engine under lean-stratified operation. *Fuel* **107** (2013), 225–235. DOI: `10.1016/j.fuel.2013.01.019`.

[OBM10] H. Oh, C. Bae, and K. Min. Spray and Combustion Characteristics of Ethanol Blended Gasoline in a Spray Guided DISI Engine under Lean Stratified Operation. *SAE International Journal of Engines* **3**.2 (2010), 213–222. DOI: `10.4271/2010-01-2152`.

[Oh+11] H. Oh et al. Effect of Multiple Injection on Stratified Combustion Characteristics in a Spray–Guided DISI Engine under Lean Stratified Operation. *SAE Technical Paper 2011–24–0059* (2011). DOI: `10.4271/2011-24-0059`.

[PBS00] J. A. Pumphrey, J. I. Brand, and W. A. Scheller. Vapour pressure measurements and predictions for alcohol-gasoline blends. *Fuel* **79** (2000), 1405–1411. DOI: `10.1016/S0016-2361(99)00284-7`.

[Por+67] R. P. Porter et al. A study of hydrocarbon flames. *Symposium (International) on Combustion* **11**.1 (1967), 907–917. DOI: `10.1016/S0082-0784(67)80217-0`.

[PPO01] B. E. Poling, J. M. Prausnitz, and J. P. O'Connell. *Properties of Gases and Liquids.* 5th. McGraw-Hill Education, 2001. ISBN: 9780070116825.

[PRS14] B. Peterson, D. L. Reuss, and V. Sick. On the ignition and flame development in a spray-guided direct-injection spark-ignition engine. *Combustion and Flame* **161** (2014), 240–255. DOI: `10.1016/j.combustflame.2013.08.019`.

[PS13] L. Piazza and R. Span. An equation of state for methanol including the association term of SAFT. *Fluid Phase Equilibria* **349** (2013), 12–24. DOI: `10.1016/j.fluid.2013.03.024`.

[Rei15] K. Reif, ed. *Gasoline Engine Management. Systems and Components.* Springer Fachmedien Wiesbaden, 2015. ISBN: 978-3-658-03964-6. DOI: `10.1007/978-3-658-03964-6`.

[Riz58] W. Rizk. Experimental Studies of the Mixing Processes and Flow Configurations in Two-Cycle Engine Scavenging. *Proceedings of the Institution of Mechanical Engineers* **172**.1 (1958), 417–437. DOI: `10.1243/PIME_PROC_1958_172_037_02`.

[RS61] F. P. Ricou and D. B. Spalding. Measurements of entrainment by axisymmetrical turbulent jets. *Journal of Fluid Mechanics* **11**.1 (1961), 21–32. DOI: `10.1017/S0022112061000834`.

[SA03] L. Song and J. Abraham. Entrainment Characteristics of Transient Turbulent Round, Radial and Wall-Impinging Jets: Theoretical Deductions. *Journal of Fluids Engineering* **125**.4 (2003), 605–612. DOI: `10.1115/1.1593707`.

[SAW13] R. A. Stein, J. E. Anderson, and T. J. Wallington. An Overview of the Effects of Ethanol-Gasoline Blends on SI Engine Performance, Fuel Efficiency, and Emissions. *SAE International Journal of Engines* **6**.1 (2013), 470–487. DOI: `10.4271/2013-01-1635`.

[Sch90] H. H. Schobert. *The Chemistry of Hydrocarbon Fuels.* Butterworth-Heinemann, 1990. ISBN: 978-0408038256.

[Set01] G. S. Settles. *Schlieren and Shadowgraph Techniques. Visualizing Phenomena in Transparent Media.* Springer Berlin Heidelberg, 2001. ISBN: 978-3-642-56640-0. DOI: `10.1007/978-3-642-56640-0`.

[Sic13] V. Sick. High speed imaging in fundamental and applied combustion research. *Proceedings of the Combustion Institute* **34** (2013), 3509–3530. DOI: `10.1016/j.proci.2012.08.012`.

[Som88] G. R. Somayajulu. A Generalized Equation for Surface Tension from the Triple Point to the Critical Point. *International Journal of Thermophysics* **9**.4 (1988), 559–566. DOI: `10.1007/BF00503154`.

[SPS14] J. A. Schroeder, S. G. Penoncello, and J. S. Schroeder. A Fundamental Equation of State for Ethanol. *Journal of Physical and Chemical Reference Data* **43** (2014). DOI: `10.1063/1.4895394`.

[SR12] M. Sjberg and D. Reuss. NOx-Reduction by Injection-Timing Retard in a Stratified-Charge DISI Engine using Gasoline and E85. *SAE Internation Journal of Fuels and Lubricants* **5**.3 (2012). DOI: `10.4271/2012-01-1643`.

[SR13] M. Sjberg and D. Reuss. High-speed imaging of spray-guided DISI engine combustion with near-TDC injection of E85 for ultra-low NO and soot. *Proceedings of the Combustion Institute* **34**.2 (2013), 2933–2940. DOI: `10.1016/j.proci.2012.05.033`.

[SS01] E. Stevens and R. Steeper. Piston Wetting in an Optical DISI Engine: Fuel Films, Pool Fires, and Soot Generation. *SAE Technical Paper 2001–01–1203* (2001). DOI: `10.4271/2001-01-1203`.

[Sta01] B. R. Stanmore. The oxidation of soot: a review of experiments, mechanisms and models. *Carbon* **39** (2001), 2247–2268. DOI: `10.1016/S0008-6223(01)00109-9`.

[Sti+13] R. Stiehl et al. In-Cylinder Flow and Fuel Spray Interactions in a Stratified Spray-Guided Gasoline Engine Investigated by High-Speed Laser Imaging Techniques. *Flow Turbulence Combustion* **91** (2013), 431–450. DOI: `10.1007/s10494-013-9500-x`.

[Sto+05] B. D. Stojkovic et al. High-speed imaging of OH* and soot temperature and concentration in a stratified-charge direct-injection gasoline engine. *Proceedings of the Combustion Institute* **30**.2 (2005), 2657–2665. DOI: `10.1016/j.proci.2004.08.021`.

[Sto+12] J. M. Storey et al. Exhaust Particle Characterization for Lean and Stoichiometric DI Vehicles Operating on Ethanol-Gasoline Blends. *SAE Technical Papers 2012-01-0437* (2012). DOI: `10.4271/2012-01-0437`.

[Sto+14] J. M. Storey et al. Novel Characterization of GDI Engine Exhaust for Gasoline and Mid- Level Gasoline-Alcohol Blends. *SAE International Journal of Fuels and Lubricants* **7**.2 (2014), 571–579. DOI: `10.4271/2014-01-1606`.

[SW03a] R. Span and W. Wagner. Equations of State for Technical Applications. I. Simultaneously Optimized Functional Forms for Nonpolar and Polar Fluids. *International Journal of Thermophysics* **24**.1 (2003), 1–39. DOI: `10.1023/A:1022390430888`.

[SW03b] R. Span and W. Wagner. Equations of State for Technical Applications. II. Results for Nonpolar Fluids. *International Journal of Thermophysics* **24**.1 (2003), 41–109. DOI: `10.1023/A:1022310214958`.

[SW91] U. Setzmann and W. Wagner. A New Equation of State and Tables of Thermodynamic Properties for Methane Covering the Range from the Melting Line to 625 K at Pressures up to 100 MPa. *Journal of Physical and Chemical Reference Data* **20**.6 (1991), 1061–1155. DOI: `10.1063/1.555898`.

[The01] The Commission of The European Union. *Commission Directive 2001/116/EC of 20 December 2001 adapting to technical progress Council Directive 70/156/EEC on the approximation of the laws of the Member States relating to the type-approval of motor vehicles and their trailers (Text with EEA relevance).* OJ L 18, 21.1.2001. 2001. URL: `http://eur-lex.europa.eu/legal-content/en/ALL/?uri=CELEX:32001L0116`.

[The07] The European Parliament and The Council of the European Union. *Commission Regulation (EC) No 715/2007 of the European Parliament and of the Council of 20 June 2007 on type approval of motor vehicles with respect to emissions from light passenger and commercial vehicles (Euro 5 and Euro 6) and on access to vehicle repair and maintenance information (Text with EEA relevance).* OJ L 171, 29.6.2007. 2007. URL: `http://eur-lex.europa.eu/legal-content/EN/TXT/?uri=CELEX:32007R0715`.

[The09] The European Parliament and The Council of the European Union. *Commission Regulation (EC) No 443/2009 of the European Parliament and of the Council of 23 April 2009 setting emission performance standards for new passenger cars as part of the Community's integrated approach to reduce CO 2 emissions from light-duty vehicles (Text with EEA relevance).* OJ L 140, 5.6.2009. 2009. URL: `http://eur-lex.europa.eu/legal-content/EN/TXT/?uri=CELEX:32009R0443`.

[The12] The European Commission. *Commission Regulation (EU) No 459/2012 of 29 May 2012 amending Regulation (EC) No 715/2007 of the European Parliament and of the Council and Commission Regulation (EC) No 692/2008 as regards emissions from light passenger and commercial vehicles (Euro 6).* OJ L 142, 1.6.2012. 2012. URL: `http://eur-lex.europa.eu/legal-content/EN/TXT/?uri=CELEX:32012R0459`.

[The14] The European Parliament and The Council of the European Union. *Commission Regulation (EU) No 333/2014 of the European Parliament and of the Council of 11 March 2014 amending Regulation (EC) No 443/2009 to define the modalities for reaching the 2020 target to reduce CO 2 emissions from new passenger cars.* OJ L 103, 5.4.2014. 2014. URL: `http://eur-lex.europa.eu/legal-content/EN/TXT/?uri=CELEX:32014R0333`.

[The70] The Council of the European Communities. *Council Directive 70/220/EEC of 20 March 1970 on the approximation of the laws of the Member States relating to measures to be taken against air pollution by gases from positive-ignition engines of motor vehicles.* OJ L 76, 6.4.1970. 1970. URL: `http://eur-lex.europa.eu/legal-content/en/ALL/?uri=CELEX:31970L0220`.

[The91] The Council of the European Communities. *Council Directive 91/441/EEC of 26 June 1991 amending Directive 70/220/EEC on the approximation of the laws of the Member States relating to measures to be taken against air pollution by emissions from motor vehicles.* OJ L 242, 30.8.1991. 1991. URL: `http://eur-lex.europa.eu/legal-content/EN/TXT/?uri=CELEX:31991L0441`.

[The98] The European Parliament and The Council of the European Union. *Directive 98/69/EC of the European Parliament and of the Council of 13 October 1998 relating to measures to be taken against air pollution by emissions from motor vehicles and amending Council Directive 70/220/EEC.* OJ L 350, 28.12.1998. 1998. URL: `http://eur-lex.europa.eu/legal-content/en/ALL/?uri=CELEX:31998L0069`.

[Tun09] P. Tunestl. Self-tuning gross heat release computation for internal combustion engines. *Control Engineering Practice* **17** (2009), 518–524. DOI: `10.1016/j.conengprac.2008.09.012`.

[Tur62] J. S. Turner. The 'starting plume' in neutral surroundings. *Journal of Fluid Mechanics* **13**.3 (1962), 356–368. DOI: `10.1017/S0022112062000762`.

[Uni15] United Nations Economic Commision for Europe. *Worldwide harmonized Light vehicles Test Procedure (WLTP).* 2015. URL: `https://www2.unece.org/wiki/pages/viewpage.action?pageId=2523179`.

[Vel+10] A. Velji et al. Investigations of the Formation and Oxidation of Soot Inside a Direct Injection Spark Ignition Engine Using Advanced Laser-Techniques. *SAE Technical Paper 2010–01–0352* (2010). DOI: `10.4271/2010-01-0352`.

[VW09] S. Verhelst and T. Wallner. Hydrogen-fueled internal combustion engines. *Progress in Energy and Combustion Science* **35**.6 (2009). DOI: `10.1016/j.pecs.2009.08.001`.

[Wal+14] S. van der Walt et al. scikit-image: image processing in Python. *PeerJ* **2** (2014), e453. DOI: `10.7717/peerj.453`.

[Whi+11] P. Whitaker et al. Measures to Reduce Particulate Emissions from Gasoline DI engines. *SAE International Journal of Engines* **4**.1 (2011), 1498–1512. DOI: `10.4271/2011-01-1219`.

[Yaw12] C. L. Yaws. *Yaws' Critical Property Data for Chemical Engineers and Chemists*. Knovel, 2012. URL: `http://app.knovel.com/hotlink/toc/id:kpYCPDCECD/yaws-critical-property`.

[Zig+11] L. Zigan et al. Structure of evaporating single- and multicomponent fuel sprays for 2nd generation gasoline direct injection. *Fuel* **90** (2011), 348–363. DOI: `10.1016/j.fuel.2010.08.001`.

[ZL98] H. Zhao and N. Ladommatos. Optical diagnostics for soot and temperature measurement in diesel engines. *Progress in Energy and Combustion Science* **24**.3 (1998), 221–255. DOI: `10.1016/S0360-1285(97)00033-6`.

[ZLH99] F. Zhao, M. C. Lai, and D. L. Harrington. Automotive spark–ignited direct–injection gasoline engines. *Progress in Energy and Combustion Science* **25** (1999), 437–562. DOI: `10.1016/S0360-1285(99)00004-0`.